TÉCNICO LISBOA

Assessing the coupling between the SSG-LRR Reynolds stress model and the $\gamma - Re_\theta$ transition model

Pedro Movilha Nogueira da Silva

Thesis to obtain the Master of Science Degree in

Aerospace Engineering

Supervisor(s): Prof. Luís Rego da Cunha Eça
Phd. Rui Miguel Alves Lopes

Examination Committee

Chairperson: Prof. Fernando José Parracho Lau
Supervisor: Prof. Luís Rego da Cunha Eça
Member of the Committee: Prof. João Manuel Ribeiro Costa Baltazar

October 2021

Dedicated to ”vovó”.

Acknowledgments

First of all, I would like to thank IST for all the support and commitment to transform high-school students into real-life engineers. With all its ups and downs, going through college makes you tough. Going through IST makes you tougher. The amount of work and knowledge absorbed in five (at least) years makes you wonder what else can make you feel unable to reach your goals. It's just like the army. It hurts. But it is worth it. And makes you ready for everything.

Then, a word to my friends. Several times have I found myself struggling in various scenarios, and I can say that I have never felt forsaken at any time by them. Whether studying for a test, or preparing an event, the groups were always there to help each other. A special thanks to "Comitiva", "Triatlo" and "Condóminos", three of my most dear groups of buddies, that helped me smile in those hard times when there were three tests and two deadlines in one week. One of the good things I think everybody should learn from college is that if you want to go far, you must to go with friends. It works like in a good bar - with no friends, it gets pretty boring. And you end up going home earlier.

I would also want to thank to my girlfriend. For listening to me, for being one of the best human beings I know, and for being a truly awesome engineer.

FST Lisboa deserves an honorable mention in these acknoledgements as well. Despite being the reason of me taking so long to write this thesis, those boys and girls became a second family that grew and held together through the though COVID times, building a fantastic racing car, capable of aiming for victories and glory.

A special acknowledgement should also go to my supervisors, professor Luís Eça, and Dr. Rui Lopes. Professor Eça was always prompt to show me the right path through this work, while having the patience to answer all my questions, and passing me a part of his immense knowledge. Dr. Rui Lopes was truly relentless in helping me with all the daily questions that came up while doing this this, and was always available to enlighten me with his technical knowledge and experience as an older student.

Last, but not least, a special gratitude to my parents and grandparents. For educating me, for raising me, and for understanding me. The support and guidance you have been giving to me for the last 24 years is immense, and I am so thankful for that.

Resumo

A utilização de novos métodos para simular escoamentos de transição assume uma importância crescente no mundo da aerodinâmica. Na gama média de números de Reynolds ($10^5 - 10^7$), com aplicações que vão desde o escoamento em torno de um drone até ao estudo de modelos a serem utilizados num túnel de vento, a utilização das equações RANS com modelos de turbulência associados a um modelo de transição é vista como uma alternativa precisa e mais barata a outros métodos, tais como DNS ou LES. Usando as equações RANS, um dos métodos mais precisos para modelar a turbulência são os modelos de tensões de Reynolds (RSM). Os RSM não são isotrópicos e são vistos como sendo uma alternativa mais fiável para simulações de RANS com média no tempo, quando comparados com os EVMs. Associar RSMs a um método fiável de prever de transição é, portanto, algo que deve ser experimentado, a fim de verificar se os resultados obtidos são satisfatórios e precisos quando comparados com outros métodos de previsão de turbulência, e com dados experimentais.

O foco deste trabalho é então aplicar as equações RANS para modelar e captar as propriedades médias de um escoamento de transição. Estas equações são completadas com o modelo de turbulência SSG-LRR-ω, acoplado ao modelo de transição $\gamma - Re_\theta$. São estudados vários casos de teste: uma placa plana, um perfil, e um esferóide 6:1. Será avaliada a robustez numérica deste acoplamento, e a influência das condições de fronteira no local de transição, sendo estas características comparadas com as de outros acoplamentos: o $k - \omega$ SST + $\gamma - Re_\theta$ e o $k - \sqrt{k}L$ + $\gamma - Re_\theta$.

Palavras-chave: RANS, SSG-LRR-ω, $\gamma - Re_\theta$, escoamento de transição

Abstract

The use of new methods to simulate transitional flows is gaining increasing importance in the world of aerodynamics. In the middle Reynolds number range ($10^5 - 10^7$), with applications ranging from the flow around a drone to the study of models to be used in a wind-tunnel, the use of RANS approach with turbulence models coupled with a method for predicting transition appears as an accurate and cheaper alternative to other methods, such as DNS or LES. In the RANS approach, one of the most precise methods for modelling turbulence is the RSMs. RSMs present the advantage of not being isotropic and are viewed as being a more accurate alternative for time-averaged RANS simulations when compared to EVMs. Coupling this with a reliable transition-prediction method is, therefore, something that must be tried out in order to verify that the results obtained are satisfactory and accurate when compared to other turbulence predicting methods, and with experimental data.

The focus of this work is then to apply the RANS equations for modelling and capture the mean properties of a transitional flow. These equations are closed with the SSG-LRR-ω turbulence model, coupled with the $\gamma - Re_\theta$ transition model. Several test-cases are studied: a flat plate, an airfoil, and a 6:1 prolate spheroid. The numerical robustness of this coupling is assessed, as well as the influence of the inlet turbulence boundary conditions on the location of transition, with these characteristics being compared with the ones from other couplings: the $k - \omega$ SST + $\gamma - Re_\theta$ and the $k - \sqrt{k}L$ + $\gamma - Re_\theta$.

Keywords: RANS, SSG-LRR-ω, $\gamma - Re_\theta$, transitional flow

Contents

Acknowledgments v
Resumo vii
Abstract ix
List of Tables xv
List of Figures xvii
Nomenclature xxi
Glossary 1

1 Introduction **2**
1.1 Thesis Outline 3
1.2 Transition Phenomena 4
1.3 Transitional Flows Study Overview 8
1.4 ReFRESCO Software 12
1.5 Objectives 12

2 Theoretical Overview **14**
2.1 Mathematical Model 14
2.1.1 RANS Equations 14
2.1.2 Turbulence Models 15
2.1.3 Transition Model 19
2.2 Non Dimensional Turbulence Quantities 22
2.2.1 Eddy viscosity ratio 22
2.2.2 Turbulence Intensity 22

3 Numerical Solution **23**
3.1 Inlet Boundary Conditions in ReFRESCO 23
3.2 Decay of Turbulence Quantities 24
3.3 Quantities of interest 25
3.4 Numerical Model 27
3.4.1 The linear equation solver and the mass-momentum coupling solver 27
3.4.2 Convergence Tolerance 27
3.4.3 Convective flux discretization schemes 27

3.4.4 Relaxation Procedure . . . 27

4 Flat Plate Test-Case **29**

4.1 Problem Description . . . 29
4.1.1 Domain . . . 29
4.1.2 Boundary Conditions . . . 30
4.1.3 Numerical Settings . . . 31
4.2 Preliminary Calculations . . . 33
4.2.1 Comparisons with Other Studies . . . 33
4.2.2 Correlation with Experimental Studies . . . 35
4.3 Numerical Errors . . . 36
4.3.1 Grid Dependance in the RSM and $k-\omega$ SST models . . . 37
4.3.2 Turbulence Kinetic Energy decay . . . 41
4.3.3 Conclusions . . . 44
4.4 Influence of Inlet Boundary Conditions . . . 45
4.4.1 Inlet Boundary Conditions . . . 45
4.4.2 Calculation of the Sensitivity Coefficients . . . 46
4.4.3 Results . . . 48
4.4.4 Conclusions . . . 50

5 Airfoil Test-Case **51**

5.1 Problem Definition . . . 51
5.1.1 Domain . . . 51
5.1.2 Boundary Conditions . . . 52
5.1.3 Numerical Settings . . . 53
5.1.4 Sensitivity Coefficients Calculations . . . 54
5.2 Results . . . 56
5.2.1 Sensitivity Coefficients . . . 56
5.2.2 Comparison between the $k-\omega$ SST and the SSG-LRR-ω . . . 60

6 Spheroid Test-Case **62**

6.1 Problem Definition . . . 62
6.1.1 Domain . . . 62
6.1.2 Boundary Conditions . . . 63
6.1.3 Numerical Settings . . . 64
6.1.4 Simulation Stopping Criteria . . . 64
6.2 Results . . . 64

7 Conclusions **70**

7.1 Achievements . . . 70
7.1.1 Validation with results from other codes and experimental data . . . 70

7.1.2 Numerical Robustness of the SSG-LRR-ω + $\gamma - Re_\theta$ coupling 70
7.1.3 Transition Prediction 70
7.1.4 Influence of the decay of the turbulence inlet conditions 71
7.2 Future Work 71

Bibliography **73**

List of Tables

4.1 Number of cells in the domain, on the flat plate surface, $((y_n^+)_c)_{max}$ and designation of the several grids used. 32
4.2 Inlet conditions used for the flat plate test-cases in [2]. 34
4.3 Inlet boundary conditions for the $k-\omega$ SST + γ -Re_θ model that match the experimental location of transition. 35
4.4 Inlet boundary conditions which are kept constant throughout the grid refinement study. . 36
4.5 Values of uncertainty for the calculation of the transition position. 39
4.6 Inlet turbulence boundary conditions used for the determination of the sensitivity coefficients. 45
4.7 X-coordinate values used to calculate the FSTI sensitivity coefficient. 46
4.8 Sensitivity coefficients to the inlet turbulent boundary conditions calculated for the T3A case, for the beginning, middle, and end of transition, for the three different turbulence models: SSG-LRR-ω, $k-\omega$ SST and $k-\sqrt{k}L$. 48
4.9 Sensitivity coefficients to the inlet turbulent boundary conditions calculated for the T3AM case, for the beginning, middle, and end of transition, for the three different turbulence models: SSG-LRR-ω, $k-\omega$ SST and $k-\sqrt{k}L$. 48

5.1 Inlet turbulence boundary conditions used for the determination of the sensitivity coefficients to the inlet EVR and FSTI for the airfoil test-case. 53
5.2 Number of cells on the surface of the airfoil, total number of cells, and $((y_n^+)_c)_{max}$ of the different grids used in the airfoil test-case. 53
5.3 Sensitivity coefficients to the inlet turbulent boundary conditions obtained with the C_f distribution for the upper surface of the NLF1-0416 airfoil using the SSG-LRR-ω and the $k-\omega$ SST models. 56
5.4 Sensitivity coefficients to the inlet turbulent boundary conditions obtained with the C_f distribution for the lower surface of the NLF1-0416 airfoil using the SSG-LRR-ω and the $k-\omega$ SST models. 57
5.5 Inlet turbulence boundary conditions used for the determination of the sensitivity coefficients to the inlet EVR and FSTI for the airfoil test-case. 58
5.6 Values of the turbulence quantities of the different simulations, at the inlet and at a distance of $11c$ downstream from it. The variation of values between simulations is displayed for the two locations, in percentage. 58

6.1 Number of cells on the surface of the spheroid, total number of cells, and $((y_n^+)_c)_{max}$ of the grid used in the spheroid test-case. 64
6.2 Description of all the cases used to study the flow over the 6:1 spheroid, regarding the usage of transition model, the turbulence quantities in several points, flow separation, and iterative convergence. In the penultimate column, ”Sep.” stands for ”flow separation”. . . . 66

List of Figures

1.1 Neutral stability curves for velocity profiles with and without inflection point [13]. 5
1.2 Depiction of the velocity profiles in a crossflow transition environment [16] 6
1.3 Depiction of transition induced by Tolmien-Schlichting waves [18]. 7
1.4 Depiction of separation induced transition [21]. 8

4.1 Different blocks that compose the grid used in the flat-plate test-case, highlighted in different colours. 32
4.2 C_f distribution for the $k-\omega$ SST model with the inlet conditions described in table 4.2. . . 34
4.3 C_f distribution for all the models used in [2] with the inlet conditions presented in table 4.2 34
4.4 C_f distribution for the RSM model with the inlet conditions described in table 4.2. 34
4.5 C_f distribution for all the models used in [2] with the inlet conditions presented in table 4.2 34
4.6 C_f distribution obtained with the RSM and k-ω model and experimental correlation for the T3AM case ($grid1$). 35
4.7 Turbulence Kinetic Energy map obtained with the RSM model for the experimental correlation data for the T3AM case. 35
4.8 C_f distribution obtained with the RSM and k-ω models and experimental correlation for the T3A case ($grid1$). 36
4.9 Turbulence Kinetic Energy map obtained with the RSM model for the experimental correlation data for the T3A case. 36
4.10 Evolution of the C_f distribution with the grid refinement level for the $T3AM-BC1$ condition for the RSM. 37
4.11 Evolution of the C_f distribution with the grid refinement level for the $T3AM-BC1$ condition for the $k-\omega$ SST. 37
4.12 Evolution of the C_f distribution with the grid refinement level for the $T3A-BC1$ condition for the RSM. 38
4.13 Evolution of the C_f distribution with the grid refinement level for the $T3A-BC1$ condition for the $k-\omega$ SST. 38
4.14 Evolution of the C_f distribution with the grid refinement level for the $T3B-BC1$ condition for the RSM. 38
4.15 Evolution of the C_f distribution with the grid refinement level for the $T3B-BC1$ condition for the $k-\omega$ SST. 38

4.16 Evolution of transition position with the increasing level of grid refinement for the different turbulent inlet conditions. Bars representing the numerical uncertainty for the calculation of transition position for the finer grid are shown. The used axis scale is different in the rightmost figure. 39
4.17 Evolution of the C_f distribution with the grid refinement level for the $T3B - BC2$ condition for the RSM. 40
4.18 Evolution of the C_f distribution with the grid refinement level for the $T3B - BC2$ condition for the $k - \omega$ SST. 40
4.19 C_f distribution for all the different cases tested with the flat plate, with different inlet turbulence boundary conditions, for the RSM and the $k - \omega$ SST models. 41
4.20 Turbulence Kinetic Energy for the $T3B - BC2$ condition for the SSG-LRR-ω using $grid8$. . 42
4.21 Turbulence Kinetic Energy for the $T3B - BC2$ condition for the $k - \omega$ SST using $grid8$. . . 42
4.22 Curves representing the variation of the freestream turbulence kinetic energy along the domain in the x direction for both the RSM and the $k - \omega$ SST models for T3B-BC2 conditions using $grid8$. 42
4.23 Turbulence Kinetic Energy for the $T3B - BC2$ condition for the SSG-LRR-ω using $grid1$. . 43
4.24 Turbulence Kinetic Energy for the $T3B - BC2$ condition for the $k - \omega$ SST using $grid1$. . . 43
4.25 Curves representing the variation of the freestream turbulence kinetic energy along the domain in the x direction for both the RSM and the $k - \omega$ SST models for T3B-BC2 conditions using $grid8$. 43
4.26 C_f distribution for the RSM model, using three different sets of inlet conditions, for the T3AM conditions. The three horizontal lines correspond to the three phases of transition: beginning, middle and end. 46
4.27 C_f distribution for the RSM model, using three different sets of inlet conditions, for the T3A conditions. The three horizontal lines correspond to the three phases of transition: beginning, middle and end. 46
4.28 Sensitivity coefficients to the inlet turbulent boundary conditions calculated for the T3A case, for the beginning, middle, and end of transition, for the three different turbulence models: SSG-LRR-ω, $k - \omega$ SST and $k - \sqrt{k}L$. 49
4.29 Sensitivity coefficients to the inlet turbulent boundary conditions calculated for the T3AM case, for the beginning, middle, and end of transition, for the three different turbulence models: SSG-LRR-ω, $k - \omega$ SST and $k - \sqrt{k}L$. 49

5.1 Different blocks that comprise the grid used in the airfoil test-case highlighted in different colours - view of the entire domain. 54
5.2 Different blocks that comprise the grid used in the airfoil test-case highlighted in different colours - zoomed view. 54
5.3 Different blocks that comprise the grid used in the airfoil test-case highlighted in different colours - zoomed view. 54

5.4 Different blocks that comprise the grid used in the airfoil test-case highlighted in different colours - surface detail. 54
5.5 C_f distribution for the RSM model. The three horizontal lines correspond to the three phases of transition: beginning, middle and end. The filled green bars match the chosen C_f values for the upper surface, and the dashed blue lines for the lower surface. 55
5.6 C_f distribution for the $k-\omega$ SST model. The three horizontal lines correspond to the three phases of transition: beginning, middle and end. The filled green bars match the chosen C_f values for the upper surface, and the dashed blue lines for the lower surface. 55
5.7 Analytical solution for the turbulent kinetic energy decay along the domain for three different cases. 58
5.8 Turbulent kinetic energy decay along the domain. It is possible to see that the inital decay - near the leading edge - is abrupt, and then it tends to a stable, assymptotic behaviour. The airfoil is located in the middle of the image, and it is possible to see the wake it produces. 60
5.9 C_f curves obtained for the five different sets of turbulent inlet conditions, both for the SSG-LRR-ω and the $k-\omega$ SST. The filled lines represent the reults obtained for the SSG-LRR-ω model and the dashed lines for the $k-\omega$ SST model. Green lines correspond to the results for the upper surface, and blue lines for the lower surface. 61

6.1 Depiction of the grid in the regions near the spheroid. The ”cross” in the mesh is due only to visual effects, and does not intend to represent any additional local refinement. 64
6.2 Zoomed view of the grid used around the spheroid test-body. It is possible to see the additional refinement employed near the body. 64
6.3 Detailed view of the grid zoomed near the leading edge of the spheroid. The grid is considerably more refined in the regions adjacent to the body, to better capture the near-wall phenomena. 65
6.4 Depiction of the grid used on the spheroid's surface, near its leading edge. This grid structure is symmetric in relation to the spheroid's mid planes, and so the region near the trailing edge will present an identical configuration. 65
6.5 Map of the skin-friction in the x direction on the surface of the spheroid using the SSG-LRR ω model with 0.15 $\%$ of FSTI at the LE of the spheroid. The streamlines show the recirculation of the flow inside the large separation bubble that is formed on the suction side. 66
6.6 Map of the skin-friction in the x direction on the surface of the spheroid using the $k-\omega$ SST model with 0.15 $\%$ of FSTI at the LE of the spheroid. The recirculation of the flow shown by the streamlines highlights a much smaller separation bubble in the suction side than in the RSM. 66
6.7 Map of the skin-friction in the x direction on the surface of the spheroid using the SSG-LRR-ω with Case4. The streamlines show that there is no recirculation of the flow as in Case1. 67

6.8 C_f distribution on the unrolled surface of the prolate spheroid obtained for Case1 with the $k-\omega$ SST model. 67
6.9 C_f distribution on the unrolled surface of the prolate spheroid obtained for Case1, with the SSG-LRR-ω model. 68
6.10 C_f distribution on the unrolled surface of the prolate spheroid obtained for Case2, with the SSG-LRR-ω model. 68
6.11 C_f distribution on the unrolled surface of the prolate spheroid obtained for Case3, with the SSG-LRR-ω model. 68
6.12 C_f distribution on the unrolled surface of the prolate spheroid obtained for Case4, with the SSG-LRR-ω model. 68
6.13 C_f distribution on the unrolled surface of the prolate spheroid obtained for Case5, with the SSG-LRR-ω model. 69
6.14 C_f distribution on the unrolled surface of the prolate spheroid obtained for Case8, with the SSG-LRR-ω model. 69

Nomenclature

Greek symbols

α	Angle of attack.
α_{exp}	Explicit under relaxation factor.
α_{imp}	Implicit under relaxation factor.
ϵ	Turbulence dissipation rate.
γ	Intermittency factor.
μ	Dynamic viscosity of the fluid.
μ_t	Dynamic turbulent (eddy) viscosity.
ν	Kinematic viscosity of the fluid.
ν_t	Kinematic turbulent (eddy) viscosity.
ω	Specific turbulence dissipation rate.
Φ	Average value of a given quantity.
ϕ	Fluctuation of a given quantity.
ρ	Density.
τ	Shear stress.
$\tilde{\Phi}$	Instantaneous value of a given quantity.

Roman symbols

p	Static pressure.
$\mathbf{Re}$	Reynolds number.
$\mathbf{Re_{\theta t}}$	Transition momentum thickness Reynolds number.
$\mathbf{Re}_\theta$	Momentum thickness Reynolds number.
$\mathbf{V}$	Velocity vector.

Subscripts

∞	Free-stream condition.
c	At the near-wall cell centre.
i, j, k	Computational indexes.
n	Normal component.
t	Tangential component.
w	At the wall.
x, y, z	Cartesian components.
ref	Reference condition.

Glossary

DNS	Direct Numerical Simulation.
EVM	Eddy Viscosity Based Model.
EVR	Eddy Viscosity Ratio.
FSTI	Freestream Turbulence Intensity.
LES	Large Eddy Simulation.
LE	Leading Edge.
LRR	Launder-Reece-Rodi.
RANS	Reynolds-averaged Navier Stokes.
RSM	Reynolds Stress Model.
SSG	Speziale-Sarkar-Gatski.
SST	Shear Stress Transport.
TE	Trailing Edge.
Tu	Turbulence Intensity.

Chapter 1

Introduction

The constant pursuit of new ways of simulating increasingly complex transitional flows motivates inumerous studies and research in the aerodynamics field [1–3]. For the past few years, new tools have been developed, with the purpose of increasing the simulation's modelling accuracy, without a significant rise in the computational costs . For cases of transitional flows, where a significant part of the flow is laminar, the use of the Reynolds averaged Navier Stokes (RANS) mathematical approach with a Reynolds stress model (RSM) to model turbulence, coupled with a reliable transition prediction method is emerging as an alternative to other numerical methods such as the direct numerical simulation (DNS), large eddy simulation (LES), or the e^N method. RSMs present the advantage of being able to deal with turbulence anisotropy and are often regarded as being a more accurate alternative for time-averaged RANS simulations, when compared to eddy viscosity based models (EVMs). Combining RSMs with transition models can be advantageous in geometries with strong curvature, with rotational flows [4], where other models as the $k-\omega$ SST model [5] might be less reliable. The focus of this work draws upon assessing the coupling between the SSG-LRR-ω Reynolds stress model [6] and the $\gamma - Re_\theta$ transition model [7].

There are two main objectives of this research:

1. Evaluate the numerical robustness of the SSG-LRR-ω + γ-Re_θ combination, i.e. check the ability to reduce the residuals to negligible levels;

2. Evaluate the influence of inlet turbulence boundary conditions on the location of transition predicted with the SSG-LRR-ω+γ-Re_θ combination and compare it with the results obtained with the $k-\omega$ SST+γ-Re_θ combination;

To fullfill these objectives, three different test cases were selected, each one having different goals:

1. 2D study of a flow over a flat plate, which allows the use of an inlet boundary relatively close to the leading edge;

2. 2D study of a flow around the NFL1-0416 airfoil that exhibits separation induced transition as well as natural transition;

3. 3D Study of a flow around a prolate spheroid to include a three-dimensional geometry.

1.1 Thesis Outline

This thesis has been divided into various chapters, each focusing on different relevant aspects for the assessment and evaluation of the SSG-LRR-ω+$\gamma - Re_\theta$ model:

1. Chapter 1 features a brief review of the transition phenomena, adressing the different mechanisms behind it. It also focuses on the latest developments in the study of transitional flows, providing an overview about the different approaches available to conduct studies regarding this topic. This chapter also introduces the reader to *ReFRESCO* [8], the software used to perform all the simulations in this thesis.

2. Chapter 2 states the mathematical approach that is used in this work to simplify the Navier-Stokes equations. It also furnishes a characterization of the different turbulence and transition models used, as well as details regarding the different couplings used in this thesis. A brief explanation of non-dimensional turbulence quantities is also given.

3. Chapter 3 states the numerical options used in *ReFRESCO* to numerically solve the mathematical approach applied to the problem. It also yields a characterization of the decay of the turbulence quantitites along the domain, and its implications in the work developed in this thesis.

4. Chapter 4 presents the results obtained for the flat plate 2D test-case, with the grid refinement studies necessary to assess the numerical errors inherent to the SSG-LRR-ω + $\gamma - Re_\theta$, $k - \omega$ SST + $\gamma - Re_\theta$ and $k - \sqrt{L}L$ + $\gamma - Re_\theta$ couplings. Sensitivity studies are presented, to evaluate the influence that the inlet turbulence boundary conditions have on these couplings, namely in the prediction of transition.

5. Chapter 5 features the results achieved in the airfoil 2D test-case, where another sensitivity analysis was performed. It is also shown a comparison between the results obtained with the SSG-LRR-ω + $\gamma - Re_\theta$ and the $k - \omega$ SST + $\gamma - Re_\theta$ couplings.

6. Chapter 6 comprises all the analysis performed with the 3D test-case of the prolate spheroid, where the focus is to evaluate the influence of the inlet turbulent boundary conditions on the predicition of transition using the SSG-LRR-ω + $\gamma - Re_\theta$ and the $k - \omega$ SST + $\gamma - Re_\theta$ couplings.

7. Chapter 7 strives to gather all the relevant conclusions withdrawn from the analysis performed with the different test-cases, and endorses some suggestions for future work that might be done in this field.

1.2 Transition Phenomena

In transitional flows, the transition phenomena is obviously an important part of the flow. The transition from laminar to turbulent happens due to the amplification of small disturbances naturally existent in the environment, that influence the boundary layer [9]. These disturbances can be of various types: mechanical vibrations of the body itself, pressure waves related to acoustic phenomena, surface roughness, etc. There are certain characteristics, such as the Reynolds number of the flow, the shape of the velocity profile in the boundary layer, the disturbance wave-length, its angular frequency or propagation velocity, that can make the flow to denote **receptivity** to the small disturbances. The disturbance can be so amplified that, after a highly nonlinear process, it leads to a degeneration of the flow into a chaotic, turbulent regime. Alternatively, if it is damped, the regime will remain organized, laminar. [10]

For the various types of disturbances, the transition process can be described in the following four phases:

1. Shear layer instability due to essentially two-dimensional perturbations;
2. Appearance of secondary disturbances that contribute to tri-dimensionalities;
3. Random formation of turbulent eruptions;
4. Degeneracy in turbulent regime .

If the amplitude of the disturbance is very high, the first two, very rapid steps of the normal transition process are bypassed, turbulent eruptions arise spontaneously, and the transition occurs abruptly, a phenomena known as bypass transition [11].

Types of Instabilities

To describe the instabilities that a laminar boundary layer may be subjected to, that will later induce transition from laminar to turbulent regime, one can recur to the Orr-Sommerfeld equation [12]. This intends to find the biggest amplification rates of a given flow instability, that can be characterized by, among others, two parameters: k and ω. k is the disturbance's wave number, representing the number of waves by unit of length in rad/m, and ω is the angular frequency - the number of cycles by unit of time, in rad/s. When the ω of a given instability is zero, it can be considered a purely spatial amplification. With a given k and Reynolds number, the Orr-Sommerfeld equation assumes the shape of an eigenfunction Φ and eigenvalues $c = c_r + ic_i$. These eigenvalues are usually represented in a $\overline{k}$ vs Re diagram where each point corresponds to a pair $(c_r; c_i)$. The geometric place of the points of $c_i = 0$ (neutral stability curve) separates the stable dampened regions ($c_i > 0$) from the unstable regions where the instabilities are amplified ($c_i < 0$).

These instabilities may be viscous or inviscid. Viscous instabilities can only occur when the Reynolds number is finite. On the other hand, for inviscid instabilities, even in the situation of $Re = \infty$ (simulation of ideal flow), there is a range of perturbation's wavelengths that can be amplified. When looking at the

average velocity profile of a boundary layer, they may or may not exhibit an inflection point. This will influence the type of instabilities they can subjected to [10].

Free shear layers (such as jets, wakes and mixing layers) and boundary layers in adverse pressure gradients do exhibit velocity profiles with an inflexion point, and so they can be subjected to both viscous and inviscid instabilities. Boundary layers in null and favourable pressure gradients do not present an inflexion point in their velocity profile, and so they have characteristics of only viscous instabilities.

This behaviour is displayed in figure 1.1, where the neutral stability curves for velocity profiles with and without inflexion points are displayed. The inner part of a curve represents the unstable region, and the outer part the stable region. As expected, the unstable region for boundary layers whose velocity profiles have an inflection point is bigger and includes the unstable region for velocity profiles with no point of inflection. The difference between the two curves can be seen as the inviscid instability region.

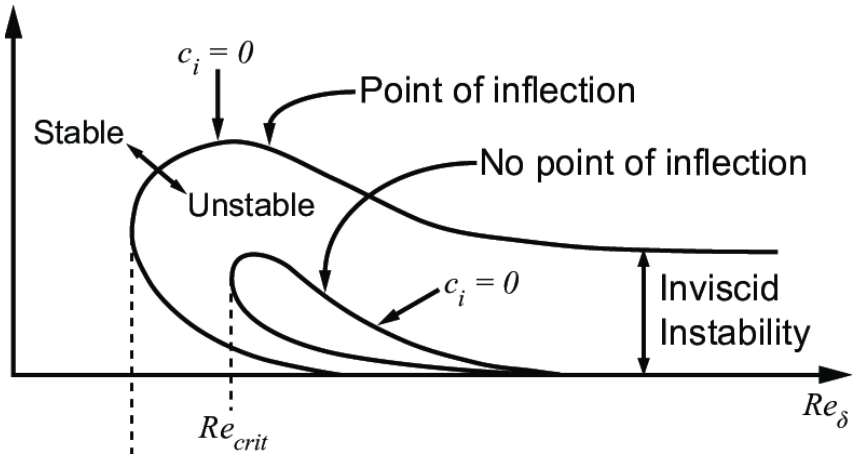

Figure 1.1: Neutral stability curves for velocity profiles with and without inflection point [13].

Crossflow Transition

Crossflow transition is a common phenomena in some curved bodies, such as spheroids or swept wings. In the inviscid region outside the boundary layer, the curvature of the body and the pressure-gradients produce curved streamlines in the boundary layer's edge. In this region outside of the boundary layer, the centripetal force is counteracted by the pressure gradients. However, inside the boundary layer, the streamwise velocity is reduced, due to viscous effect in the near-wall region, therefore reducing the centripetal forces. Since the pressure gradient remains unchanged, this creates a secondary flow in the boundary layer, perpendicular to the streamwise direction, usually named crossflow [14]. Physically, this inflectional boundary layer profile is inherently unstable and entails the development of a series of streamwise-oriented co-rotating vortical disturbances that redistribute momentum within the boundary layer. These instability modes can be of a stationary or traveling nature, depending on boundary layer receptivity to free stream conditions and surface roughness, and have been found to have a distinctive effect on the topology of the transition front. The growth and laminar breakdown of these crossflow instability mechanisms will then eventually induce transition [15].

Figure 1.2 depicts the 3-D sketch of the various velocity profiles that are characteristic of a 3-D boundary layer with crossflow.

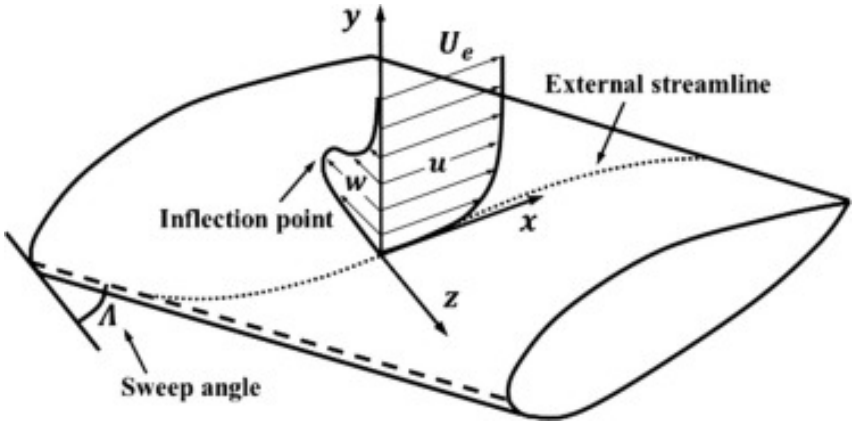

Figure 1.2: Depiction of the velocity profiles in a crossflow transition environment [16] .

Streamwise Transition

In the streamwise direction, several types of transition can occur, such as the **Tolmien-Schlichting** or **natural** transition, **bypass** transition and **separation induced** transition.

Tolmien-Schlichting transition occurs usually in zero-pressure or weak adverse-pressure gradient conditions, by the action of unstable disturbances, namely a bi-dimensional progressive wave that emerges in boundary layer flows [17]. When the velocity fluctuations reach a certain amplitude, secondary, less powerful instabilities will arise, resembling longitudinal vortices. The progressive wave is then disturbed by these, assuming a tri-dimensional shape, and causing tri-dimensional changes to the velocity profile inside the boundary layer.

This is what creates the so-called hairpin vortices. These vortices are of an unstable nature, with the discrepancies in the velocity profile causing their filaments to stretch, increasing vorticity, and increasing the intensity of the disturbance velocities. In consequence, the disturbance to the fundamental instability will be enlarged, producing high shear stress local regions, randomly distributed in space and time, which tend to detonate in chaotic, tri-dimensional eruptions. These will expand, affecting the whole field, that then assumes statistically stationary characteristics corresponding to a fully developed turbulent state [10].

Figure 1.3, taken from [18], depicts the different phases of the transition by the action of Tolmien-Schlichting waves.

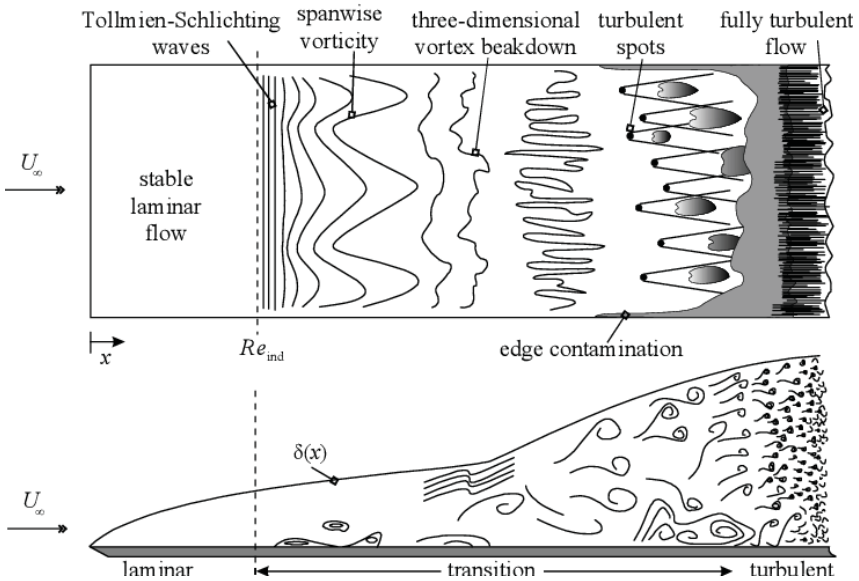

Figure 1.3: Depiction of transition induced by Tolmien-Schlichting waves [18].

On the other hand, **bypass** transition is forced by very strong freestream perturbations, that cause the first steps of transition described in figure 1.3 to be bypassed, in a way that the turbulent spots are directly produced. This type of transition is common among turbomachinery flows, and occurs usually when the freestream turbulence intensity is greater than 1% [19]. Increased surface roughness and turbulent injections into the boundary layer also promote the occurence of bypass transition.

Separation-induced Transition occurs when the laminar boundary layer is under strong adverse pressure gradients, that will stimulate flow separation. When some disturbances such as the Kelvin-Helmholtz (K-H) instabilities [20], or the Tolmien-Schlichting waves (these latter only prevail when the Reynolds number is lower) enter the separated shear layer, the recirculating flow inside of it will interact with them, leading to their growth. This will eventually trigger transition further downstream. Once transition has started, the momentum exchange in the mixing layer decreases the size of the reverse flow bubble, and hence its displacement effect as well. This shear layer will thus entrain more fluid, and contribute to the reattachment of it. This entire process forms what is called laminar separation/turbulent reattachment bubble on the surface of the body, as depicted in figure 1.4, composed by [21]. The size of the separation bubble will vary according to the inlet turbulence boundary conditions - the larger the turbulence intensity, the smaller the bubble, since the flow will more promptly transit to turbulent. The value of the adverse pressure gradient will also play a part in the bubble size, since larger gradients will originate bigger bubbles. The Reynolds number also influences the bubble dimension: for lower values of it, transition may occur slowly, and the turbulent mixing effect may be insufficient to make the flow reattach.

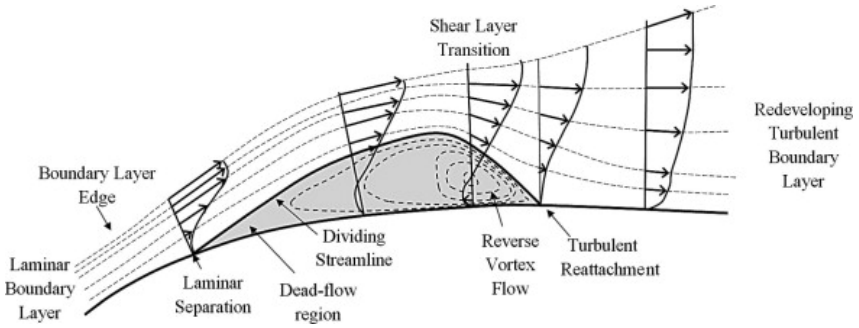

Figure 1.4: Depiction of separation induced transition [21].

1.3 Transitional Flows Study Overview

Simulating flows around bodies with complex geometries is fundamental in early stages of the design process of numerous engineering projects. Whether in the air flow around an airplane, a drone, or a race car, an increase in the simulation's modelling accuracy is beneficial to improve the efficiency of the final design itself, and of the whole process that leads to it.

That being said, the discovery and evaluation of new methods to simulate transitional flows, as the one presented in this thesis, that allow to correct any of the shortcomings of the current state of the art, is beneficial. Simulating transitional flows is of increased importance when studying flows at a mid-range Reynolds numbers (1×10^5 to 5×10^6), where transition plays a major role in the overall flow. Some practical real life applications of these flows can include the airflow around a drone, wind tunnel flows over scaled models, the water motion around a small submarine, or even the study of the flight of birds of prey, such as eagles and hawks.

To study transitional flows over objects with simple geometries, methods known for their superior accuracy such as the direct numerical simulation (DNS) can be a possibility [22]. It involves the direct solution of the unsteady Navier Stokes equations in the whole spectrum of spatial and temporal scales of the flow. In the DNS approach, the number of needed mesh points grows exponentially with the Reynolds number, increasing the memory storage requirement [23]. Therefore, it is currently suitable to simulate problems only at relatively low Reynolds numbers. Several researches have been made in the recent years, regarding this topic, simulating the entire transition regime to a fully turbulent boundary layer, including bypass transition due to high-intensity free-stream turbulence [24, 25], the transition processes associated with linear instabilities such as the oblique breakdown of first mode waves in a two-dimensional supersonic boundary layer [26, 27] or the transition due to secondary instabilities of Tollmien-Schlichting waves in a low-speed flat plate boundary layer [1].

Other methods, such as large eddy simulation (LES) appear as simplification of the DNS approach [28]. The principle behind LES is to ignore the smaller length scale phenomena, which are the most computationally expensive to solve, by time and space averaging the Navier-Stokes equations. This acts as a low-pass filter, that exempts the numerical solution from the smaller scale information. However, the latter is not irrelevant for the simulation's final result, prompting researches in how to model its effect

in the flow field [29, 30]. Since this modelling is not perfect, in situations where small-scales can play an important role, such as near-wall flows, LES may not be the most suitable option. Nevertheless, several different studies regarding transitional flows have been performed with this method, such as a LES of controlled transition to turbulence [3], LES of transition to turbulence in a boundary layer developing spatially over a flat plate [31], or LES of boundary layer transition over an isolated ramp-type micro roughness element [32].

Turbulence Models

Other tools used nowadays to simulate transitional flows near walls draw upon some simplification of the Navier-Stokes equations such as in the case of the Reynolds Averaged Navier-Stokes (RANS) equations. This mathematical method averages the continuity and momentum equations, and all the dependant variables, requiring a **turbulence model** to perform the so-called "closure of the problem" [33], explained in subsection 2.1.2. Various types of turbulence models can be used, each one of them possessing its own strenghts and downsides. Two of the most used types of turbulence models are the eddy viscosity based models (EVMs) and the Reynolds stress models (RSMs).

EVMs can be one or two equation models, as the $k-\omega$ SST (shear stress transport) or the $k-\sqrt{k}L$ model, where the Reynolds stresses are obtained through a previously established assumption, such as the Boussinesq hypothesis [34]. They present several advantages: are relatively simple due to the use of an isotropic eddy (turbulent) viscosity; are stable via stability-promoting second-order gradients in the meanflow equations, and work reasonably well for a large number of engineering flows [35]. However, the use of an isotropic concept of viscosity (which is a false assumption in near-wall conditions) causes the Reynolds stress tensor to be directly proportional to the strain rate tensor. It is then a poor model when comes to predict the normal Reynolds stresses, which for flows with strong curvature and rotation may harm the accuracy of the solution.

On the other hand, full second-moment RSMs, such as the SSG-LRR-ω are establishing themselves as an alternative to one or two equation linear/non-linear EVMs [36]. The greater grid dependance and the more difficult iterative convergence that the RSMs may yield are the current drawbacks of this model that should have a superior modelling ability when compared to EVMs [37]. In the RSMs, the Reynolds stresses are directly computed, eliminating the flaws coming from assumptions such as the Boussinesq hypothesis. They can deal with the anisotropy of turbulence, due to the re-distribution of the Reynolds stresses coming from the pressure-strain correlation. This makes RSMs more accurate than EVMs in predicting flows with normal Reynolds stress anisotropy [37] and flows with large amounts of rotation, such as the free vortices created in the tip of a plane's wing [38]. It is also indicated for flows with strong curvature [4], or with large instability regions [39] and strong adverse pressure gradients [2].

RSMs can solve an unsteadiness of the flow, in situations where an EVM could predict a steady flow [2]. This, however, comes at the expense of a higher computational effort. Therefore, it will only be useful if the resolved unsteadiness is effectively significant for the final result of the simulation. If not, the RSM may not be the best alternative, since the increased computation effort and time dispended are not really useful.

In EVMs, the Boussinesq assumption provide specific relations between the derivatives of the Reynolds stresses and the second derivatives of the velocity components. In RSMs, that specific relation does not exist. Although this can contribute to the dampening of some numerical instabilities in RSMs [35], it causes the iterative convergence to be faster in EVMs when compared with RSMs [40].

In general, RSMs are more complex than most of the EVMs, due to the higher effort placed in modelling the pressure-strain correlation and the diffusion and destruction terms of the Reynolds stresses. Therefore, RSM's offer more possibilites to be tuned and calibrated with data coming from experimental set-ups.

Transition Models

Except for DNS, and LES that can be used for transitional flows [41], but presents the disadvantages mentioned before, the previously discussed models are not suitable to model transition on their own [42], since they usually predict transition sooner than what is verified in the real flow. Therefore, in order to ensure that transition phenomena occurring in the flow are accounted for, one should complement the turbulence model with a suitable method for predicting transition.

Modelling transition is not easy, and the variety of models available to do it has a much smaller spectrum than for modelling turbulent flows. [42]. This has to do with several reasons:

- Transition phenomena are indeed really sensitive to external factors, such as pressure gradients, surface roughness, inlet turbulent quantities and Reynolds number;
- Transitional flows involve a wide range of both temporal and spatial scales, with an intricated energy and momentum transfer between eddies of different shapes that is highly non-linear and therefore, hard to model;
- Transition can occur due to several reasons and can be of various types: natural, separated-induced, bypass or crossflow (for 3-D cases only), and taking all these into account in a simulation can be a complex task;
- In the case of RANS formulation, where the effects of linear disturbance growth are eliminated [42], transition may be hard to model, since this latter is affected by both linear and non-linear phenomena.

Nevertheless, several transition prediction methods and models have been developed, and it is possible to enumerate some of them, such as the linear stability theory based e^N method, empirical correlation based methods, or local transport equation based transition models, such as the $\gamma - Re_\theta$ model [7].

The e^N is a commonly used non-local method [43], that needs access to integral parameters of the flow. In RANS applications, where there is usually a decomposition of the domain by several computational cores, is hard to implement this non-local method: one processing core could need information stored in another one, requiring an additional computational effort, since this passage of information is usually time-consuming. The e^N method also presents some more downsides, since it is limited to

some transition mechanisms, and only provides the location of the transition point, meaning it ”activates” the turbulence model downstream of that point.This abrupt switch causes a discontinuity in the domain, which may harm the iterative convergence [43].

Empirical correlation based methods [44] predict transition based on directly applicable correlations. They are not very complex. and are not used much anymore nowadays, having been replaced by other more reliable methods.

Local transport equation based transition models such as the γ model [45] or the $\gamma - Re_\theta$ model [7] are frequently and easily coupled with RANS applications [46]. Being local models, they only require information available in the cell, and do not make use of integral parameters. Therefore, the domain partition by several computational cores that are commonly used with RANS does not hinder the model to obtain the information it requires.

In this work, the $\gamma - Re_\theta$ model was the chosen transition model to be coupled with the SSG-LRR$-\omega$ model, since this thesis follows the work reported in [46]. The choice of this coupling was due to all the factors described above, and to the fact that the $\gamma - Re_\theta$ transition model is one of the most widely used in formulations with other turbulence models, such as EVMs. However, although the SSG-LRR-ω + γ-Re_θ combination was implemented in [46], it has not been thoroughly tested, being still a relatively recent approach for solving transitional flows. Therefore, its full potential is not yet known, with only some studies being published about the capabilites and performance of this model in some very specific conditions [2].

This work aims then to keep discovering how does this model compare with the results provided by other more conventional approaches, such as the $k - \omega$ SST model coupled with the $\gamma - Re_\theta$ transition model.

1.4 ReFRESCO Software

The 2.6 version of the ReFRESCO software was used in all the computations performed in the present work. As defined in the official website [8], "ReFRESCO is a viscous-flow CFD code that solves multiphase (unsteady) incompressible flows using the Navier-Stokes equations, complemented with turbulence models, cavitation models and volume-fraction transport equations for different phases. Various turbulence models, from RANS models to high fidelity hybrid and scale resolving models, complemented with transition models are available. The equations are discretised using a finite-volume approach discretization of the RANS and turbulence quantities transport equations, with cell-centered collocated variables, in strong conservation form. A pressure-correction equation based on the SIMPLE algorithm is used to ensure mass conservation. Nonorthogonality and eccentricity corrections are applied in the determination of normal derivatives and variable values at the faces centre. Flux limiters are included in the upwind second-order schemes applied to the convective terms. The implementation is face-based, which permits grids with elements consisting of an arbitrary number of faces (hexahedrals, tetrahedrals, prisms, pyramids, etc.), and if needed h-refinement (hanging nodes)".

ReFRESCO enables a segregated or coupled solution of the continuity and momentum equations. On the other hand, the solution of the k and ω transport equations is always segregated. Therefore, all the simulations presented in this thesis were performed with the segregated approach.

There was a crossflow transition predicition method available, but it was decided not to include it in the model. This would only be eventually useful in the case of the 3-D spheroid. However, the main purpose of this test-case is to compare the behaviour of both the $k-\omega$ SST and the SSG-LRR-ω , and evaluate the influence that the inlet turbulence boundary conditions have on them, which does not require a crossflow transition prediction method. However, if the results withdrawn from this work are to be compared with experimental data, care must be taken, since crossflow transition could occur in the real flow and not be predicted by ReFRESCO.

In all the simulations made with ReFRESCO, the fluid is assumed to be Newtonian, single-phase and incompressible, meaning that the density ρ remains constant. The dynamic molecular viscosity μ is also constant in a simulation.

1.5 Objectives

The aim of this work is to assess the performance of coupling of the SSG-LRR-ω turbulence model with the $\gamma - Re_\theta$ transition model in predicting transitional flows. The results obtained were, in some cases, compared with the ones acquired with the $k-\omega$ SST [5], and the $k-\sqrt{k}L$ [47] models. These three models are the most commonly used in ReFRESCO applications.

The evaluation of this coupling was performed by simulating the flow around bodies with different geometries. As said before, there are three different test-cases, two 2D and one 3D: a flat plate, the NLF1-0416 airfoil, and a 6:1 prolate spheroid. These different test-cases will allow to obtain several conclusions:

- Validate the results obtained for the flat plate test-case using the implementation of the coupling SSG-LRR-ω + $\gamma - Re_\theta$ in ReFRESCO with the ones obtained in other previous works, and with experimental data;
- Perform grid refinement studies in the 2D flat plate test-case using the SSG-LRR-ω and the $k - \omega$ SST model coupled with the $\gamma - Re_\theta$, for both natural and bypass transition, to assess the numerical robustness of the couplings;
- With the 2D flat plate test-case, perform sensitivity analysis to establish how the SSG-LRR-ω + $\gamma - Re_\theta$ coupling is affected by the change in the inlet turbulence conditions of the simulations, namely the eddy viscosity ratio and the freestream turbulence intensity, and compare this data with the one obtained with the $k - \omega$ SST + $\gamma - Re_\theta$ and the $k - \sqrt{k}L$ + $\gamma - Re_\theta$ couplings;
- Evaluate how the decay of the inlet turbulence quantities influences the results of a simulation, namely the position of transition, when the test-body is located far downstream of the inlet, in the 2D airfoil test-case;
- In the 2D airfoil test-case adress the differences in prediction of transition between the SSG-LRR-ω + $\gamma - Re_\theta$ and the $k - \omega$ SST + $\gamma - Re_\theta$ combinations;
- Using the 3D spheroid test-case, assess if the inlet turbulence boundary conditions tuned to be used with the $k - \omega$ SST + $\gamma - Re_\theta$ combination are suitable to be used with the SSG-LRR-ω + $\gamma - Re_\theta$;
- Evaluate how the decay of the inlet turbulence quantities will affect the occurence of transition in the 3D spheroid test-case.

Chapter 2

Theoretical Overview

2.1 Mathematical Model

To describe flows of viscous, incompressible fluids, one can resort to mass conservation and momentum balance, which can be expressed in a Cartesian coordinate system as:

$$\begin{gathered} \frac{\partial \tilde{V}_i}{\partial x_i} = 0. \\ \frac{\partial \left(\rho \tilde{V}_i\right)}{\partial t} + \frac{\partial \left(\rho \tilde{V}_i \tilde{V}_j\right)}{\partial x_j} = -\frac{\partial \tilde{P}}{\partial x_i} + \frac{\partial \tau_{ij}}{\partial x_j}. \end{gathered} \tag{2.1}$$

Being $\tilde{V}_i$ the instantaneous Cartesian velocity components, ρ the fluid density, $\tilde{P}$ is the relative pressure (with the reference pressure being the hydrostatic pressure). The subscripts i and j are computational indexes representing consecutive, non-equal cartesian coordinates x, y, z and τ_{ij} stands for the components of the stress tensor, which for a Newtonian fluid is given by:

$$\tau_{ij} = \mu \left(\frac{\partial \tilde{V}_i}{\partial x_j} + \frac{\partial \tilde{V}_j}{\partial x_i} \right). \tag{2.2}$$

2.1.1 RANS Equations

The three test cases evaluated in this thesis are wall bounded transitional flows, at a middle range Reynolds number, meaning that the boundary-layer developing on the body surface may present transition to the turbulent regime. Hence, the flow will be unsteady, exhibiting a wide range of length and time scales that make the direct solution of equations 2.1 too expensive as per the reasons mentioned in subsection 1.3. Therefore, the RANS approach can used, meaning that all instantaneous flow variables $\tilde{\Phi}$ are decomposed in a mean value Φ and a fluctuation ϕ (turbulence). To discover a variable $\tilde{\Phi}$, different type of averaging can be used, depending on the physics of the flow. For the flows analysed in this work, where the mean flow is statistically steady, time-averaging can be applied, being defined by equation 2.3:

$$\Phi(x_i) = \lim_{T\to\infty} \frac{1}{T} \int_0^T \tilde{\Phi}(x_i, t)\, dt. \tag{2.3}$$

Applying equation 2.3 to the variables in the continuity and momentum equations 2.1, one obtain the RANS equations, defined by:

$$\begin{aligned} \frac{\partial V_i}{\partial x_i} &= 0. \\ \frac{\partial(\rho V_i V_j)}{\partial x_j} &= -\frac{\partial P}{\partial x_i} + \frac{\partial}{\partial x_j}\left(\mu\left(\frac{\partial V_i}{\partial x_j} + \frac{\partial V_j}{\partial x_i}\right) - \rho\overline{\tilde{V}_i\tilde{V}_j}\right). \end{aligned} \tag{2.4}$$

This leads to a statistically steady flow. However, it also generates the Reynolds stress tensor $-\rho\overline{\tilde{V}_i\tilde{V}_j}$ patent in the momentum equation, where the overbar stands for average values.

The notation used in this thesis for the Reynolds stresses is ρR_{ij}, that is equivalent to $-\rho\overline{\tilde{V}_i\tilde{V}_j}$, as expressed in equation 2.5:

$$\rho R_{ij} = -\rho\overline{\tilde{V}_i\tilde{V}_j}. \tag{2.5}$$

This additional term requires closure, implying the formulation of an extra equation, i.e. writing this term as a function of known variables of the flow [48]. This is achieved by using a turbulence model, that will prescribe the values of the Reynolds stresses, through modeling approximations, allowing the computational solving of these equations. To prescribe the values for the Reynolds stresses, turbulence models can follow different approaches, as explained in subsection 2.1.2.

2.1.2 Turbulence Models

Some turbulence models, called eddy viscosity based models (EVM), make use of a "mathemathical concept" called **eddy viscosity** μ_t, first described by Joseph Boussinesq in [34]. The reasoning behind this first approach to eddy viscosity was to ignore the small-scale vortices (or eddies) in the motion and to calculate a large-scale motion with an eddy viscosity, that would characterize the transport and dissipation of energy in the smaller-scale flow. These models involve a previously established assumption, that relates the eddy viscosity with the Reynolds stresses, such as the Boussinesq hypothesis [34]. The way eddy viscosity is calculated nowadays depends on the formulation that each model uses, but the fundamental goal is to define it using known flow variables.

There are other turbulence models, the Reynolds stress models (RSM), that directly compute the Reynolds stresses, requiring additional equations to do so.

In this study, three different turbulence models were used: one Reynolds stress model, the SSG-LRR-ω, and two eddy-viscosity based models, the $k-\sqrt{k}L$ and the $k-\omega$ SST.

$k-\omega$ SST

The $k-\omega$ SST turbulence model is a two-equation eddy viscosity model, presented in [5]. The formulation used in this thesis follows the expressions that can be found in [49]. It features two transport

equations, for the turbulent kinetic energy k and the specific turbulent dissipation rate ω.

The turbulence kinetic energy, k, is the kinetic energy per unit mass of the turbulent fluctuations v_i in a turbulent flow [50], and can be defined as:

$$k \equiv \frac{1}{2}\overline{v_i v_i} = \frac{1}{2}\left(\overline{v_x^2} + \overline{v_y^2} + \overline{v_z^2}\right). \tag{2.6}$$

The specific turbulent dissipation rate ω is the rate at which turbulence kinetic energy is converted into thermal internal energy per unit volume and time. It is usually defined as:

$$\omega = \frac{\epsilon}{k\beta^*}. \tag{2.7}$$

Being β^* a constant of the turbulence model used, and ϵ the turbulence dissipation, representing the rate at which turbulence kinetic energy is converted into thermal internal energy [51]. It can be expressed as:

$$\epsilon \equiv \nu \frac{\partial v_i}{\partial v_k}\frac{\partial v_i}{\partial v_k}. \tag{2.8}$$

The two-equation model, for incompressible flow can be written, in conservation form, for steady flows as:

$$\frac{\rho\partial\left(V_j k\right)}{\partial x_j} = P_k - D_k + \frac{\partial}{\partial x_j}\left[\left(\mu + \sigma_k \mu_t\right)\frac{\partial k}{\partial x_j}\right]. \tag{2.9}$$

$$\frac{\rho\partial\left(V_j \omega\right)}{\partial x_j} = P_\omega - D_\omega + \frac{\partial}{\partial x_j}\left[\left(\mu + \sigma_\omega \mu_t\right)\frac{\partial \omega}{\partial x_j}\right] + 2\left(1 - F_1\right)\frac{\rho\sigma_{\omega 2}}{\omega}\frac{\partial k}{\partial x_j}\frac{\partial \omega}{\partial x_j}. \tag{2.10}$$

P_k and D_k are the production and dissipation terms of the turbulent kinetic energy k, and are stated by:

$$P_k = \min\left(\mu_t S^2, 15 D_k\right) \quad ; \quad D_k = \beta^* \rho \omega k. \tag{2.11}$$

P_ω and D_ω correspond to the production and dissipation terms of the specific turbulence dissipation ω, and are prescribed as:

$$P_\omega = \frac{\gamma}{\nu_t} P_k \quad ; \quad D_\omega = \beta \rho \omega^2. \tag{2.12}$$

σ_k, σ_ω, $\sigma_{\omega 2}$, β and γ are constants and F_1 is a blending function that switches from the $k-\epsilon$ formulation in the freestream to the $k-\omega$ formulation in the boundary layer. S is the strain rate magnitude, specified in equation 2.13:

$$S = \sqrt{2 S_{ij} S_{ij}}, \quad \text{with} \quad S_{ij} = \frac{1}{2}\left(\frac{\partial v_i}{\partial x_j} + \frac{\partial v_j}{\partial x_i}\right). \tag{2.13}$$

The eddy viscosity μ_t is given by:

$$\mu_t = \frac{\rho a_1 k}{\max\left(a_1 \omega, S F_2\right)}. \tag{2.14}$$

Being F_2 an auxiliary function and a_1 a constant.

All the equations, damping functions and constants of this model are available in [49].

$k - \sqrt{k}L$

The $k - \sqrt{k}L$ model is a linear eddy viscosity model, that features two transport equations, one for $\phi = \sqrt{k}L$, with L being the turbulent length scale, and another for k. This model is also used in ReFRESCO, and provides extra data for comparison. The formulation used in this thesis follows the expressions that can be found in [47].

The two-equation model, written in conservation form, for steady, incompressible flow, is given by the following:

$$\frac{\rho\partial\left(V_j k\right)}{\partial x_j} = P_k - D_k + \frac{\partial}{\partial x_j}\left[\left(\mu + \sigma_k \mu_t\right)\frac{\partial k}{\partial x_j}\right], \tag{2.15}$$

$$\frac{\rho\partial\left(V_j \phi\right)}{\partial x_j} = C_{\phi 1}\frac{\phi}{k}P - C_{\phi 2}\rho k^{3/2} - 6\mu\frac{\phi}{d^2}f_\phi + \frac{\partial}{\partial x_j}\left[\left(\mu + \sigma_\phi \mu_t\right)\frac{\partial \phi}{\partial x_j}\right]. \tag{2.16}$$

With:

$$P_k = \mu_t S^2 \quad ; \quad D_k = \rho c_\mu^{3/4}\frac{k^{3/2}}{L} + 2\mu\frac{k}{d^2}. \tag{2.17}$$

C_{ϕ_1}, C_{ϕ_2}, σ_ϕ are constants, d is the distance from the wall, and f_ϕ is an auxiliary function.

The eddy viscosity μ_t is given by:

$$\mu_t = \min\left(c_\mu^{1/4}\Phi, \frac{a_1 k}{S}\right).; \quad a_1 = a_1^{SST} f_b + \left(1 - f_b\right) a_1^{REAL}. \tag{2.18}$$

a_1^{SST} and a_1^{REAL} are constants, and f_b is a function that takes the value of one inside the boundary-layer and zero outside of it.

All the equations, damping functions and constants used in this formulation are available in [47].

RSM - SSG-LRR-ω

The SSG-LRR-ω model is a blend between the Speziale-Sarkar-Gatski model (SSG) [52] in the far field and the Launder-Reece-Rodi model (LRR) [53] near walls, combined with Menter's baseline ω-equation for the length scale [6]. The formulation used in this thesis follow the expressions that can be found in [54].

The SSG-LRR-ω is a full second-moment Reynolds stress model [39, 55, 56], meaning it computes each of the 6 Reynolds stresses directly, with each Reynolds stress having its own transport equation. There is also a seventh transport equation for the ω variable.

The specification of the RSM model used was the SSG/LRR-RSM-ω 2012-SD, which uses a "simple diffusion" (SD) model rather than the generalized gradient diffusion model ([57]).

The six Reynolds stresses, for steady flows, are given by equation 2.19:

$$\frac{\rho\partial(V_k R_{ij})}{\partial x_k} = \rho D_{ij} + \rho P_{ij} + \rho\Pi_{ij} - \rho\epsilon_{ij} + \rho M_{ij}. \tag{2.19}$$

With the production term ρP_{ij} and the dissipation term $\rho\varepsilon_{ij}$ given by 2.20:

$$\rho P_{ij} = -\rho R_{ik}\frac{\partial V_j}{\partial x_k} - \rho R_{jk}\frac{\partial V_i}{\partial x_k}. \quad ; \quad \rho\varepsilon_{ij} = \frac{2}{3}\rho\varepsilon\delta_{ij}. \tag{2.20}$$

The diffusion term ρD_{ij} is given by equation 2.21:

$$\rho D_{ij} = \frac{\partial}{\partial x_k}\left[\left(\mu\delta_{kl} + D\frac{\rho R_{kl}}{C_\mu\omega}\right)\frac{\partial R_{ij}}{\partial x_j}\right]. \tag{2.21}$$

The dissipation term $\rho\epsilon_{ij}$ is defined as:

$$\rho\epsilon_{ij} = \frac{2}{3}\rho\epsilon\delta_{ij}, \quad \textit{where} \quad \epsilon = C_\mu k\omega \tag{2.22}$$

Being δ_{ij} the Kronecker delta.

The pressure-strain correlation $\rho\Pi_{ij}$ is modelled via:

$$\begin{aligned}\rho\Pi_{ij} = &-\left(C_1\rho\epsilon + \frac{1}{2}C_1^*\rho P_{kk}\right)\hat{a}_{ij} + C_2\rho\epsilon\left(\hat{a}_{ik}\hat{a}_{kj} - \frac{1}{3}\hat{a}_{kl}\hat{a}_{kl}\delta_{ij}\right) + \\ &+\left(C_3 - C_3^*\sqrt{\hat{a}_{kl}\hat{a}_{kl}}\right)\rho\hat{k}\hat{S}_{ij}^* + C_4\rho k\left(\hat{a}_{ik}\hat{S}_{jk} + \hat{a}_{jk}\hat{S}_{ik} - \frac{2}{3}\hat{a}_{kl}\hat{S}_{kl}\delta_{ij}\right) + \\ &+ C_5\rho k\left(\hat{a}_{ik}\hat{W}_{jk} + \hat{a}_{jk}\hat{W}_{ik}\right)\end{aligned} \tag{2.23}$$

where pressure dilatation is neglected, and the anisotropy tensor $\hat{a}_{ij}$ is given by:

$$\hat{a}_{ij} = \frac{R_{ij}}{k} - \frac{2}{3}\delta_{ij}, \tag{2.24}$$

And the remaining auxiliary terms are available in [54]. For an incompressible fluid, as it is considered in this work, the pressure-strain correlation term represents the distribution of kinetic turbulent energy to the different directions.

The fluctuacting mass flux ρM_{ij} is neglected.

The equation for the specific rate of dissipation ω for steady flows is given by:

$$\frac{\rho\partial(V_k\omega)}{\partial x_k} = P_\omega - D_\omega + \frac{\partial}{\partial x_k}\left[\left(\mu + \sigma_\omega\frac{\rho k}{\omega}\right)\frac{\partial\omega}{\partial x_k}\right] + \sigma_d\frac{\rho}{\omega}max\left(\frac{\partial k}{\partial x_j}\frac{\partial\omega}{\partial x_j}, 0\right). \tag{2.25}$$

With the production term P_ω and the dissipation term D_ω given by:

$$P_\omega = \frac{\alpha_\omega\omega}{k}\frac{\rho P_{kk}}{2}. \quad ; \quad D_\omega = \beta_\omega\rho\omega^2. \tag{2.26}$$

All the damping functions and constants used in this model are available in [54].

2.1.3 Transition Model

$\gamma - Re_\theta$

The $\gamma - Re_\theta$ transition model, presented in [7] is a two-equation model used to model transitional flows where a significant portion of the boundary layer is laminar. It solves transport equations for the intermittency factor, γ, represented in equation 2.27 which indicates the state of the flow, and the transition momentum thickness Reynolds number, $Re_{\theta t}$, represented in equation 2.28. The formulation used in this thesis for this model follows the equations found in [58].

$$\frac{\rho\partial(\gamma)}{\partial t} + \frac{\rho\partial\left(V_j\gamma\right)}{\partial x_j} = P_\gamma - D_\gamma + \frac{\partial}{\partial x_j}\left[\left(\mu + \frac{\mu_t}{\sigma_f}\right)\frac{\partial\gamma}{\partial x_j}\right], \tag{2.27}$$

$$\frac{\rho\partial\left(Re_{\theta t}\right)}{\partial t} + \frac{\rho\partial\left(V_j Re_{\theta t}\right)}{\partial x_j} = P_{\theta t} + \frac{\partial}{\partial x_j}\left[\sigma_{\theta t}\left(\mu + \mu_t\right)\frac{\partial Re_{\theta t}}{\partial x_j}\right], \tag{2.28}$$

With:

$$\begin{aligned} P_\gamma &= F_{\text{length}}\, c_{a1}\rho S\left[\gamma F_{\text{onset}}\right]^{0.5}\left(1 - c_{e1}\gamma\right). \\ D_\gamma &= c_{a2}\rho\Omega\gamma F_{\text{turb}}\left(c_{e2}\gamma - 1\right). \end{aligned} \tag{2.29}$$

Being F_{length}, F_{onset} and F_{turb} auxiliary functions, c_{a1}, c_{a2}, c_{e1}, c_{e2}, σ_f and $\sigma_{\theta t}$ constants, and Ω the vorticity magnitude.

The original formulation of the $\gamma - Re_\theta$ uses a new variable, the effective intermittency factor γ_{eff} variable, defined in equation 2.30:

$$\begin{aligned} \gamma_{\text{eff}} &= \max\left(\gamma, \gamma_{\text{sep}}\right) \\ \gamma_{\text{sep}} &= \min\left(s_1 \max\left[0, \left(\frac{Re_V}{3.235 Re_{\theta c}}\right) - 1\right] F_{\text{reattach}}\,, 2\right) F_{\theta t} \\ F_{\text{reattach}} &= \exp\left[-\left(\frac{R_T}{20}\right)^4\right] \end{aligned} \tag{2.30}$$

With Re_V, $Re_{\theta c}$, $F_{\theta t}$ and R_T being auxiliary functions and s_1 a constant of the model.

This original formulation of the $\gamma - Re_\theta$ features a coupling with the $k - \omega$ SST model, where the production term P_k and the dissipation term D_k of equation 2.9, and the blending function F_1 of equation 2.10 are corrected using γ_{eff}. The production term and destruction term are multiplied by γ_{eff}, to maintain laminar flow before transition. With this, in the laminar region, the effective intermittency is almost 0, resulting in zero production of turbulence. The dissipation term in this region is 0.1 times of the exact dissipation, so the destruction of turbulence is larger than its production, allowing to obtain a laminar flow. When the effective intermittency factor is 1, the transition model returns to the original turbulence model. This is achieved by replacing these terms by $\tilde{P}_k$, $\tilde{D}_k$ and $\tilde{F}_1$ respectively, with the tilde being here used to represent the corrected formulation, given by 2.31:

$$\begin{aligned} \tilde{P}_k = \gamma_{eff} P_k. \quad ; \quad \tilde{D}_k = \min\left(\max\left(\gamma_{eff}, 0.1\right), 1.0\right) D_k. \\ \tilde{F}_1 = \max\left(F_1, F_3\right). \quad ; \quad F_3 = \exp\left[-\left(\frac{R_y}{120}\right)^8\right]. \quad ; \quad R_y = \frac{\rho d\sqrt{k}}{\mu}. \end{aligned} \tag{2.31}$$

All the equations, damping functions, and constants used in this model are available in [58].

Coupling with the SSG-LRR model

The coupling of the SSG-LRR-ω with the $\gamma - Re_\theta$ follows the work developed in [46]. To perform the coupling, the source terms of the turbulent Reynolds stresses equation 2.19 in the RSM are relaxed using the γ_{eff} variable, in a similar way as with the $k - \omega$ SST model. The production term of the ω equation 2.25 is also corrected. This results in equations 2.32, 2.33, 2.34 and 2.35.

$$\tilde{P_{ij}} = \gamma_{eff} P_{ij}. \tag{2.32}$$

$$\tilde{\epsilon_{ij}} = \text{min}(\text{max}(\gamma_{eff}, 0.1), 1.0)\epsilon_{ij}. \tag{2.33}$$

$$P_\omega = (1 - c_{\text{lam}})\, P_{SST} + C_{\text{lam}}\, P_{RSM} \tag{2.34}$$

$$C_{\text{lam}} = \begin{cases} 0, & c_\omega > \gamma \\ \frac{\gamma - c_\omega}{1 - c_\omega}, & c_\omega \leq \gamma \end{cases} \text{ and } \quad c_\omega = \left(\exp\left(- \left(\frac{420}{\tilde{Re}_{\theta t}} \right)^4 \right) \right)^2 \tag{2.35}$$

Where P_{SST} corresponds to the production term P_w of the ω equation (Eq. 2.10) for the $k - \omega$ SST model, and P_{RSM} corresponds to the production term P_w of the ω equation (Eq. 2.25) for the SSG-LRR-ω model.

The final coupling employs the corrected equations 2.32 to 2.35 with equation 2.27 and 2.28.

Full details of the functions and constants used in this coupling can be found in [46].

Coupling with the $k - \sqrt{k}L$ model

The coupling of the $\gamma - Re_\theta$ transition model with the $k - \sqrt{k}L$ turbulence model is similar to the one used with the $k - \omega$ SST model. This coupling follows the work developed in [59]. The production and dissipation terms P_k and D_k are corrected in the same way. The blending function f_b is also changed, according to equation 2.36:

$$\tilde{f_b} = \text{max}(f_b, F_3). \tag{2.36}$$

When coupling the $\gamma - Re_\theta$ model with the $k - \sqrt{k}L$ model, the ω variable is needed to compute the source terms in the γ and Re_θ equations. However, this variable is not directly available, and therefore needs to be estimated resorting to μ_t, as explicit in equation 2.37:

$$\mu_t = \frac{k\rho}{\omega} \rightarrow \omega = \frac{k\rho}{\mu_t}. \tag{2.37}$$

All the damping functions and constants used in the formulation of this coupling are available in [47].

All the three turbulence models were coupled with one transition model, $\gamma - Re_\theta$, i.e. there are no calculations performed without a transition model (with an exception for the spheroid test-case, duly explained in section 6.2). For this reason, only the turbulence model is used to distinguish between

formulations: RSM stands for RSM + $\gamma - Re_\theta$ (in this work, it means the same as SSG-LRR-ω + $\gamma - Re_\theta$), $k-\omega$ SST stands for $k-\omega$ SST + $\gamma - Re_\theta$, and $k-\sqrt{k}L$ stands for $k-\sqrt{k}L$ + $\gamma - Re_\theta$.

2.2 Non Dimensional Turbulence Quantities

Similarly to k and ω, defined in section 2.1.2, one can define two non-dimensional parameters, the **eddy viscosity ratio** (EVR) and the **turbulence intensity** (Tu), that will represent the turbulent characteristics of the flow.

2.2.1 Eddy viscosity ratio

The eddy viscosity ratio, EVR, is defined as the ratio between the turbulent viscosity μ_t and the molecular dynamic viscosity of the fluid μ:

$$EVR = \frac{\mu_t}{\mu}. \tag{2.38}$$

2.2.2 Turbulence Intensity

The turbulence intensity Tu, is defined as the ratio between the root-mean square of the turbulent velocity fluctuations v, and the mean velocity V:

$$Tu = \frac{v}{V}. \tag{2.39}$$

We can also define the freestream turbulence intensity (FSTI) as the value of Tu in the freestream.

Chapter 3

Numerical Solution

3.1 Inlet Boundary Conditions in ReFRESCO

The ReFRESCO software offers the possibility of defining several boundary conditions, among them the values for EVR and Tu. Then as per the selected turbulence model, it will implicitly transform these two quantities into variables of interest for that specific model. In the case of the $k-\omega$ SST model, the obtained quantities are evidently k and ω. The latter is obtained by rearranging equations 2.14 and 2.38, and assuming that the flow is uniform, simplifying equation 2.14, resulting in equation 3.1:

$$\mu_t = \rho\frac{k}{\omega} \quad \Rightarrow \quad EVR = \frac{\rho}{\mu}\frac{k}{\omega}. \tag{3.1}$$

Assuming that turbulence is isotropic (the turbulent fluctuations are statistically uniform in all directions), it is possible to relate Tu with the freestream velocity V_∞ to obtain k, as demonstrated in equation 3.2:

$$k = 1.5 \times Tu^2 \times V_\infty^2. \tag{3.2}$$

For the RSM, the concept of eddy viscosity does not properly exist. However, the formula expressed in equation 2.14 used in the $k-\omega$ SST is also used in the RSM, to determine the value of ω. On the other hand, the turbulence intensity Tu is transformed into the six components of the Reynolds stress tensor. The non-normal stress components (R_{12}, R_{13}, R_{23}) are assumed to be equal to 0. The normal stress components (R_{11}, R_{22}, R_{33}) are equal to each other and are given by equation 3.3:

$$R_{ii} = \frac{2}{3} \times k. \tag{3.3}$$

For the $k-\sqrt{k}L$ model, the obtained quantities are k and ϕ. The first one is obtained in a similar way as in the $k-\omega$ SST, using equation 3.2. The ϕ variable is obtained by the formula displayed in equation 3.4:

$$\phi = \frac{\mu_t}{\rho C_\mu^{1/4}}. \tag{3.4}$$

Being $C_\mu = 0.09$ a constant.

These implicit transformations made by REFRESCO allows the user to define equivalent boundary conditions, regardless of the chosen turbulence model (SSG-LRR-ω, $k-\omega$ SST, or $k-\sqrt{k}L$).

3.2 Decay of Turbulence Quantities

The turbulent quantities defined in the previous section 3.1, will decay along the domain. The evolution of this decay for both the turbulence kinetic energy k and the eddy viscosity μ_t, for the $k-\omega$ SST and the SSG-LRR-ω models is given by equations 3.5 and 3.6, respectively [46]:

$$k^* = \frac{k^*_{in}}{\left(1+\beta\left(x^*-x^*_{in}\right)k^*_{in}\left(\frac{\nu}{\nu_t}\right)_{in}Re\right)^{\frac{\beta^*}{\beta}}}, \tag{3.5}$$

$$\mu_t = \frac{\mu_{tin}}{\left(1+\beta\left(x^*-x^*_{in}\right)k^*_{in}\left(\frac{\nu}{\nu_t}\right)_{in}Re\right)^{\frac{\beta^*}{\beta}-1}}. \tag{3.6}$$

The subscript $_{in}$ represents the value of the property at the inlet. The superscript * is used to represent non-dimensional quantitities. The exception is β^*, that, jointly with β are constants of the equation, available in [49].

Hence, k^* is the non-dimensional k, given by equation 3.7:

$$k^* = \frac{k}{V_\infty^2}. \tag{3.7}$$

Equations 3.5 and 3.6 are analytical solutions for the decay of k^* and μ_t for the $k-\omega$ SST model, following the assumption that the flow is uniform and aligned with the x-direction (except for the area near the test body). For the RSM, these equations require additional premises to be valid:

1. Non-normal Reynolds stresses R_{ij} are equal to zero, justified by the fact that it is a solution to the respective equations and obeys to boundary conditions;

2. Normal Reynolds stresses R_{ii} are all equal, justified by the fact that all the equations between them are identical and obey to boundary conditions;

It should be mentioned that the decay rate of turbulence is influenced by the chosen freestream values of each one of the properties. The higher the $FSTI$, the more rapid the decay; the lower the μ_t, the more rapid the decay. [61].

Considering equation 3.5, if the second part of the denominator is much larger than one, the equation can be rewritten as equation 3.8:

$$k^* \approx \frac{1}{\left(\beta\left(x^* - x^*_{in}\right)\left(\frac{\nu}{\nu_t}\right)_{in} Re\right)^{\frac{\beta^*}{\beta}}}. \tag{3.8}$$

This can occur when performing calculations for a test-body located far downstream from the inlet, meaning a value of x^* much larger than one. So, in the second and third test-cases analysed in this work - the NLF1-0416 airfoil and the 6:1 prolate spheroid, respectively - the decay is such that the values of this quantity in the body's leading edge reach an assymptotic behaviour. In other words, a change in the inlet value will imply a much smaller change of the value in a point located far downstream of the inlet. It can be such that small differences in the freestream conditions, such as the ones used in sensitivity analysis, are not noticed in the results of the simulations.

This influence of the inlet turbulent quantities in their own decay also creates another interesting phenomena: it may occur that the k at the leading edge is similar in two simulations with different inlet turbulent quantities.

Care must be taken to ensure that the grid spacing is adequate with the expected decay. For large decay rates, the coarseness of the grid far from the body may make the solver unable to support an accurate computation and the decay can be grossly underestimated. According to [61], for the higher freestream decay conditions, the computed results display a very noticeable grid dependence, only slowly approaching the correct answer as the grid is refined. For significantly lower values of FSTI, however, the decay rate is considerably reduced, and the coarser grids do not underestimate the decay as much.

Following these assumptions, it is then expectable that, for a given inlet turbulence kinetic energy, when the values for the eddy viscosity ratio are higher, and the decay smaller, one can observe a smaller grid dependence.

3.3 Quantities of interest

The performance of the different couplings used in this work was evaluated resorting to the skin-friction coefficient C_f at the surface of the test-body. This quantity is calculated at the mid-point of the cell faces, using equation 3.9:

$$C_f = \frac{\tau_w}{\frac{1}{2}\rho V_\infty^2}. \tag{3.9}$$

The τ_w variable represents the shear-stress at the wall of the test-body, and can be defined by equation 3.10.

$$\tau_w = \mu\left(\frac{\partial V_t}{\partial x_n}\right)_{y=0} \approx \mu\frac{V_{tc}}{y_{nc}} \tag{3.10}$$

Where the subscript t represents the direction tangential to the surface, and the subscript n represents the direction normal to the surface. V_{tc} is the velocity in the direction tangential to the wall,

obtained in the near-wall cell centre, and y_{nc} is the distance between the surface and the near-wall cell centre, in the direction normal to the surface.

One can also define the y_{nc}^{+} variable in equation 3.11, an useful parameter to characterize the different grids used. For values up to $y_{nc}^{+} < 5$, the mean velocity profiles in the near-wall region remain laminar.

$$y_{nc}^{+} = \frac{u_\tau y_{nc}}{v} \text{ and } u_\tau = \sqrt{\frac{\tau_w}{\rho}} \tag{3.11}$$

3.4 Numerical Model

One of the most important aspects to deal with in a CFD simulation is the numerical setup used to solve all the transport, momentum, and pressure equations used in the turbulence and transition model. Therefore, some details of this numerical setup must be briefly explained:

3.4.1 The linear equation solver and the mass-momentum coupling solver

All the transport , momentum and pressure equations solved in the turbulence and transition models are solved in the form $A\phi = B$, being A the left-hand side matrix, ϕ the solved variable and B the right-hand side vector of the equation. It is then needed to select a specific procedure to compute the solution of the linear equations. ReFRESCO uses a PETSc (Portable Extensible Toolkit for Scientific Computation) solver [62], which dictates how high-performance computers numerically solve partial differential equations. It establishes procedures for parallel matrix and vector assembly, useful in parallel application codes. Besides this, a procedure for performing the coupling between the linear systems corresponding to the momentum and pressure equation is also needed.

3.4.2 Convergence Tolerance

At each outer loop, the solution of each one of the linear equations is computed to a certain precision, dictated by this parameter.

3.4.3 Convective flux discretization schemes

To deal with the convective fluxes, different discretization schemes were used. For the flat-plate test-case, to solve the momentum, turbulence, and transition equations, a scheme named Limited-QUICK was chosen: it is a version of QUICK (Quadratic Upstream Interpolation for Convective Kinematics) [63], with applied flux limiters. QUICK is a higher-order differencing scheme that considers a three-point upstream weighted quadratic interpolation for the cell face values.

For the airfoil and spheroid cases, the only change performed is that the scheme used for the turbulence equation was a first order upwind, for robustness purposes. The Limited-QUICK scheme was employed in all the remaining equations.

3.4.4 Relaxation Procedure

In each simulation step, new values for the solution of the several equations are computed. However, it is possible to define by how much the previous value of the equation is updated, creating a blend between the old value and the new one. This is obtained by using the **explicit under relaxation** procedure.

Besides this, each of the linear equations being solved has a determined ”stifness”, related to the matrix A, that needs to be monitored and controlled (increasing the matrix diagonal and B), ensuring

that the numerical scheme is capable of producing a solution. This is the **implicit under relaxation** procedure. Both these procedures need parameters to define them: the implicit and explicit under relaxation factors.

The explicit under relaxation factor, α_{exp}, blends the solution between two consecutive iterations, using equation 3.12:

$$\phi^{n+1} = \phi^{n} + \alpha_{\exp}\left(\phi^{n+1^{*}} - \phi^{n}\right). \tag{3.12}$$

Where $\phi^{n+1^{*}}$ is the predicted solution at the new non-linear iteration, ϕ^{n+1} is the used solution at a new iteration and ϕ^{n} is the used solution at the old iteration. This factor must follow a balance: ideally, it is as high as possible, in order to decrease the overall simulation time. However, too high values can compromise the scheme's stability and ability to converge.

The implicit under relaxation factor α_{imp}, affects (increases) both the left-hand side of the diagonal of matrix A, and the right-hand side vector B, as shown in equation 3.13, taken from [64]:

$$\left(A_{ij} + \left(\frac{A_{ii}}{\alpha_{imp}} - A_{ii}\right)\right)\phi_{j}^{n} = B_{i} + \left(\frac{A_{ii}}{\alpha_{imp}} - A_{ii}\right)\phi_{j}^{n-1}. \tag{3.13}$$

At each outer loop, equation 3.13 is applied to the non-linear problem. ReFRESCO features the possibility of choosing both a minimum and maximum implicit under relaxation factor, allowing to define how to transit from one to another. When the simulation is started, α_{imp} is set to its minimum. The user can specify the number of iterations along which the minimum factor is increased, until it reaches its maximum value. This is useful to guarantee that the scheme is stable in the early stages of the simulation: despite slowing down convergence, lower factors ensure a higher stablity.

Chapter 4

Flat Plate Test-Case

This chapter is divided into four main sections. Firstly, section 4.1 features a description of the problem. Then, in section 4.2 are presented some preliminary calculations, where the modelling done with the SSG-LRR-ω model in ReFRESCO and the results obtained with it are compared and validated with other proven CFD codes, and with experimental data. Following that, in section 4.3, grid refinement studies are performed for the SSG-LRR-ω and the $k-\omega$ SST models, both coupled with the $\gamma - Re_\theta$ transition model, to evaluate the numerical errors, assessing several aspects:

1. Verify if the result values of C_f converge to a solution when increasing the refinement level of the mesh;
2. Check if transition is affected by the different mesh refinements;
3. Compare the transition characteristics of the RSM with those of the $k-\omega$ SST model, by using turbulent kinetic energy fields;

Finally, in section 4.4, sensitivity studies are performed, with the goal of quantifying the difference in how the two models react to different turbulent inlet conditions, namely the eddy viscosity ratio and the freestream turbulence intensity. In this section, the data obtained while running the simulations with the $k-\sqrt{k}L$ model was also used, to provide a broader set for comparison.

4.1 Problem Description

4.1.1 Domain

The computational domain used in this study is a rectangle with the incoming flow V_∞ and the plate of length L aligned with the horizontal direction x. The leading edge of the plate is located at the origin of the (x, y) Cartesian coordinate system. The length of the domain is $1.5L$, with the inlet located at $x/L = -0.25$ and the outlet at $x/L = 1.25$. The domain has a height of $0.25L$, being the flat plate located at $y/L = 0$ and the top boundary of the domain at $y/L = 0.25$.

The Reynolds number Re based on the undisturbed freestream velocity V_∞, L, and kinematic viscosity of the fluid ν is given by equation 4.1:

$$Re = \frac{V_\infty L}{\nu} = 10^7. \tag{4.1}$$

4.1.2 Boundary Conditions

There are six locations that require the specification of boundary conditions: the plate's surface, the inlet boundary, the top boundary, the outlet boundary and the symmetry planes upstream and downstream of the plate.

Surface of the Plate

At the surface of the plate ($0 < x < L$ and $y = 0$) the impermeability of the surface and the no-slip condition lead to exact boundary conditions for the velocity components $V_x = 0$ and $V_y = 0$. It is assumed that the pressure does not change in the direction normal to the wall, meaning $\frac{\partial p}{\partial n} = \nabla p \cdot \vec{n} = 0$. Specific boundary conditions at the wall are applied to the different turbulence models, and to the transition model.

For the RSM, ReFRESCO specifies a value of zero for the Reynolds stresses at the wall:

$$R_{ij,\,\text{wall}} = 0. \tag{4.2}$$

However, for the ω equation, instead of specifying a value at the wall, ReFRESCO designates the value for ω directly at the first interior cell, using equation 4.3 [65]:

$$\omega_{\text{cell}} = \frac{6\hat{\nu}}{\beta_\omega^{(\omega)} \left(\Delta d_1\right)^2} \quad , \quad \text{with} \quad \beta_\omega^{(\omega)} = 0.075. \tag{4.3}$$

where Δd_1 is the distance from the wall to the nearest field solution point.

For the $k - \omega$ SST model, k is specified at the wall as zero:

$$k_{\text{wall}} = 0. \tag{4.4}$$

Regarding the ω variable, ReFRESCO proceeds in a similar way as in the SSG-LRR-ω model, and designates the value for ω directly at the first interior cell, using equation 4.5:

$$\omega_{\text{wall}} = \frac{6\nu}{\beta_1 \left(\Delta d_1\right)^2} \quad , \quad \text{with} \quad \beta_1 = 0.075. \tag{4.5}$$

For the $k - \sqrt{k}L$, the k and ϕ variables are defined by equation 4.6:

$$k_{\text{wall}} = 0 \quad ; \quad (\phi)_{\text{wall}} = 0. \tag{4.6}$$

For the $\gamma - Re_\theta$ transition model the boundary conditions prescribed for the surface of the plate are given in equation 4.7:

$$\frac{\partial \gamma}{\partial x_n} = 0 \quad ; \quad \frac{\partial \hat{Re}_{\theta t}}{\partial x_n} = 0. \tag{4.7}$$

Where ∂n_{wall} referes to the direction normal to the wall.

Top Boundary

At the top boundary, the pressure is set equal to zero and all the other flow variables have null normal derivatives.

Outlet Boundary

At the outlet, streamwise derivatives equal to zero are applied to all dependent variables.

Inlet Boundary

At the inlet boundary, the velocity is set equal to undisturbed flow conditions, meaning $V_x = V_\infty$ and $V_y = 0$. For all the three turbulence models used, both the FSTI and the EVR have a Dirichlet boundary condition, i.e. an imposed value by the user. As there are various combinations of boundary conditions used throughout the chapter, these values are given as the respective cases are presented.

For the $\gamma - Re_\theta$ transition model, the inlet boundary conditions used were adopted from the recommended ones in [58], explicit in equation 4.8:

$$\begin{aligned} \gamma_{\text{farfield}} &= 1. \\ \hat{Re}_{\theta t,\,\text{farfield}} &= \begin{cases} \left(1173.51 - 589.428 Tu_\infty + 0.2196 Tu_\infty^{-2}\right), & Tu_\infty \leq 1.3 \\ 331.50\left(Tu_\infty - 0.5658\right)^{-0.671} & Tu_\infty > 1.3 \end{cases} \end{aligned} \tag{4.8}$$

Symmetry Conditions

Symmetry conditions are applied at $y = 0$ upstream ($x < 0$) and downstream ($x > L$) of the plate.

These conditions have implications in the RSM turbulence model: being the plate in a x-symmetry plane, the Reynolds stress components R_{12} (xy) should have Dirichlet condition, with an imposed value of zero. Other Reynolds stress components should yield symmetric treatment, meaning the existance of a null gradient [54].

4.1.3 Numerical Settings

Grids

The grids used in the whole study, except for the ones in subsection 4.2.1 were adopted from the AVT 313 workshop [66]. The coarsest grid used is depicted in figure 4.1, where the different blocks

are highlighted with different colours. The grid has a symmetry axis located at the plate's half length ($x/L = 0.5$).

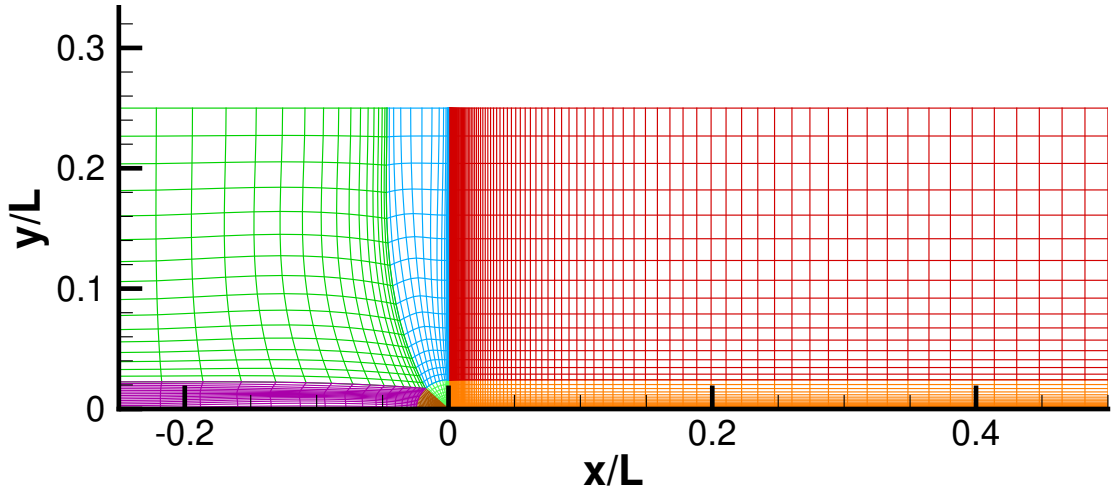

Figure 4.1: Different blocks that compose the grid used in the flat-plate test-case, highlighted in different colours.

The orthogonal grid starts upstream of the plate's leading edge, in order to ensure a high quality grid at the stagnation region. In the grid refinement studies, different but geometrically similar grids were used. Their characteristics and designation are comprised in table 4.1:

Table 4.1: Number of cells in the domain, on the flat plate surface, $((y_n^+)_c)_{max}$ and designation of the several grids used.

Grid Designation	**Number of cells in the domain**	**Number of cells on the flat plate surface**	$((y_n^+)_c)_{max}$
Grid9	20,840	256	0.92
Grid8	32,000	320	0.76
Grid7	46,080	384	0.66
Grid6	62,720	448	0.58
Grid5	81,920	512	0.52
Grid4	128,000	640	0.44
Grid3	184,320	768	0.38
Grid2	250,880	896	0.33
Grid1	327,680	1024	0.30

Simulation Stopping Criteria

The stopping criteria used in these simulations was a convergence tolerance of 10^{-6} for the residuals of certain variables, namely V_i, P, γ and Re_θ. The residual norm used was the L^∞ norm, which considers only the maximum residual value of a given variable in the entire grid.

The residuals of the turbulence-solving equation were exempted from this criteria. This eliminates

the need for the residuals of both the R_{ij} and the ω to go below the value 10^{-6} as a requirement to stop the simulation. This is explained by a condition imposed in ReFRESCO, regarding the calculation of the different Reynolds Stresses. ReFRESCO solves the transport equation, obtaining a value for ρR_{ij}.

Then, ReFRESCO checks the conditions described in equations 4.9 and 4.10:

- For the diagonal elements of the Reynolds stress tensor:

$$\rho R_{ij} \geq 0 \quad i \in 1,2,3 \quad \text{(no summation on i)} \tag{4.9}$$

- For the off-diagonal elements of the reynolds stress tensor (i not equal to j):

$$\rho R_{ij} \leq \sqrt{(\rho R_{ii})\,(\rho R_{jj})} \quad i,j \in 1,2,3 \quad \text{(no summation on i or j)} \tag{4.10}$$

If the specific condition for each Reynolds stress, normal or non-normal, is not verified, ReFRESCO imposes it, and obtains a new value. However, when solving the equation at the next iteration with this new value, the new solution will not comply with either equation 4.9 or 4.10, creating a loop, and impeding further convergence.

4.2 Preliminary Calculations

Preliminary test-cases were run prior to proceeding to quantify the numerical errors and the influence of the inlet boundary conditions obtained for the SSG-LRR-ω + $\gamma - Re_\theta$. The purpose of doing so was to evaluate how the implementation of this coupling in ReFRESCO would compare to the results obtained both experimentally in [66] and with other proven codes, as by [2].

4.2.1 Comparisons with Other Studies

The implementantion of the SSG-LRR-ω + $\gamma - Re_\theta$ coupling in ReFRESCO was compared to the one performed in [2], where the original formulation of this coupling can be found.

To mimic the inlet conditions used in [2], the grid presented in subsection 4.1.3 needed to be adapted, since the grids used in [2] have the inlet located at $x/L = -0.15$. Besides this, the cell size in the direction normal to the plate was changed, to ensure that the y+ value was appropriate and did not increase the simulation running time. Only the finest grid, $grid1$, was used.

The values then applied to the inlet conditions of ReFRESCO were the same as one condition used in [2] and are explicit in table 4.2.

The results of the simulations are displayed in figures 4.2 and 4.4. The vertical bars are shown in the same x-axis values for each pair of graphics, to ease the value correspondence:

Table 4.2: Inlet conditions used for the flat plate test-cases in [2].

Property	Value
Inlet Velocity (m/s)	5.2
μ_t/μ	13
FSTI(%) Inlet Value	7.28
Density (kg/m^3)	1.2
Dynamic viscosity (10^{-5}kg/ms)	1.79

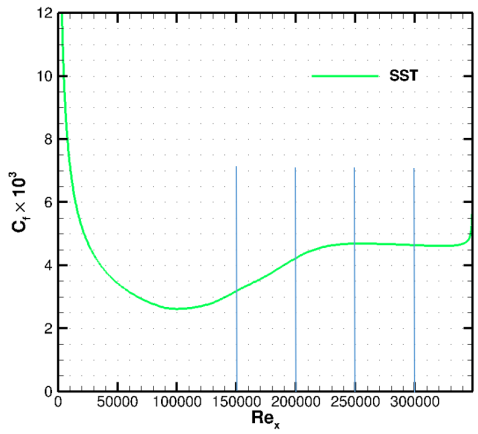

Figure 4.2: C_f distribution for the $k-\omega$ SST model with the inlet conditions described in table 4.2.

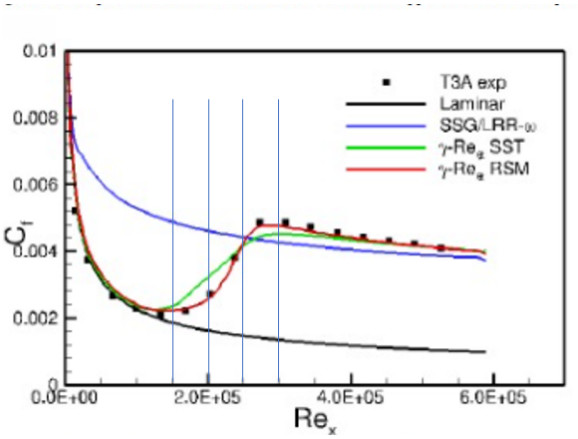

Figure 4.3: C_f distribution for all the models used in [2] with the inlet conditions presented in table 4.2

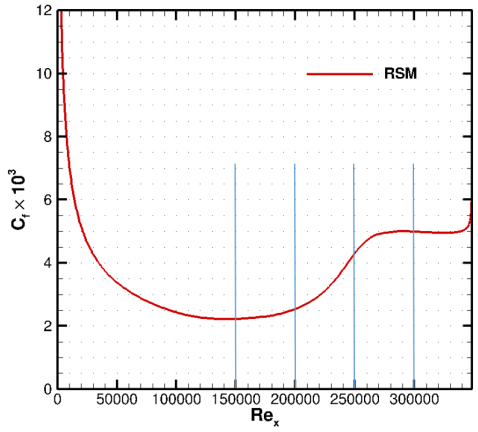

Figure 4.4: C_f distribution for the RSM model with the inlet conditions described in table 4.2.

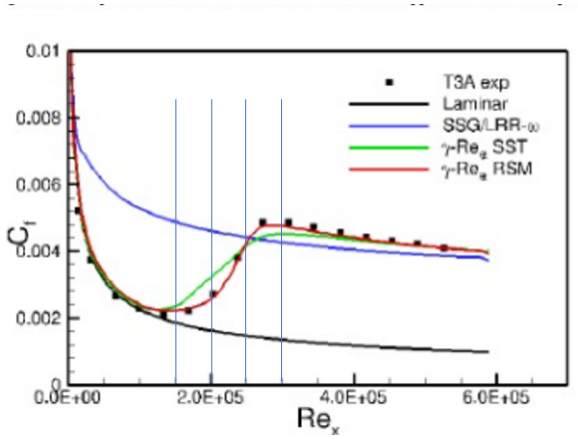

Figure 4.5: C_f distribution for all the models used in [2] with the inlet conditions presented in table 4.2

By looking at these graphics, one sees that both the $k-\omega$ SST and SSG-LRR-ω models run by ReFRESCO present a very similar behaviour with the one obtained in [2], validating the implementation performed in [46].

4.2.2 Correlation with Experimental Studies

After proving that the implementation of the RSM with the $\gamma - Re_\theta$ transition model behaves similarly to other CFD codes for identical inlet conditions, it is useful to verify how it correlates with experimental data withdrawn from [67]. In this section, the type of grid used was the one explained in subsection 4.1.3. Only the finest grid, $grid1$, was used.

Specific inlet conditions were withdrawn from [66], which provide the correct location for flow transition when used in the $k - \omega$ SST model. The values for these conditions are compiled in table 4.3:

Table 4.3: Inlet boundary conditions for the $k - \omega$ SST + γ -Re_θ model that match the experimental location of transition.

	T3AM	**T3A**
I	0.01V_∞	0.05V_∞
ν_t	25ν = 25V_∞L/Re	280ν = 280V_∞L/Re

Using the data from table 4.3, ReFRESCO was run using both the RSM and the $k - \omega$ SST model. The results are displayed in figures 4.6 to 4.9:

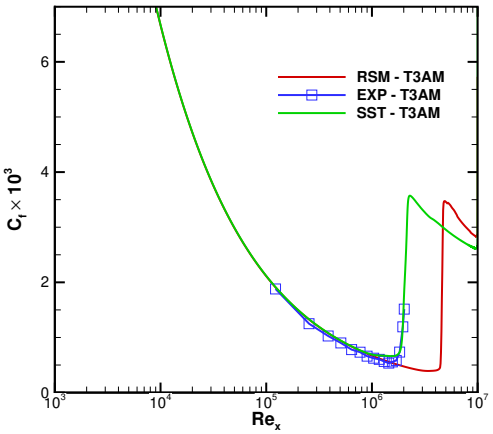

Figure 4.6: C_f distribution obtained with the RSM and k-ω model and experimental correlation for the T3AM case ($grid1$).

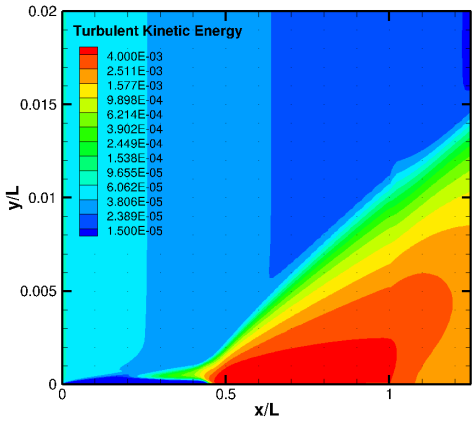

Figure 4.7: Turbulence Kinetic Energy map obtained with the RSM model for the experimental correlation data for the T3AM case.

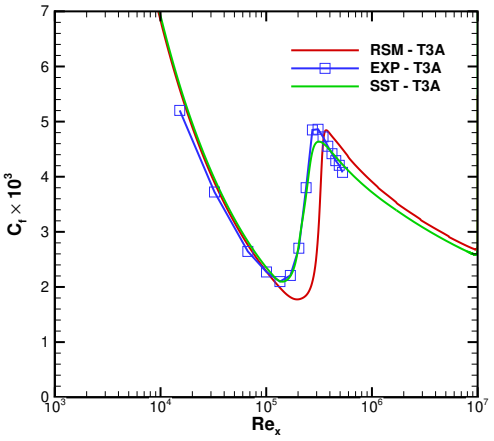

Figure 4.8: C_f distribution obtained with the RSM and k-ω models and experimental correlation for the T3A case ($grid1$).

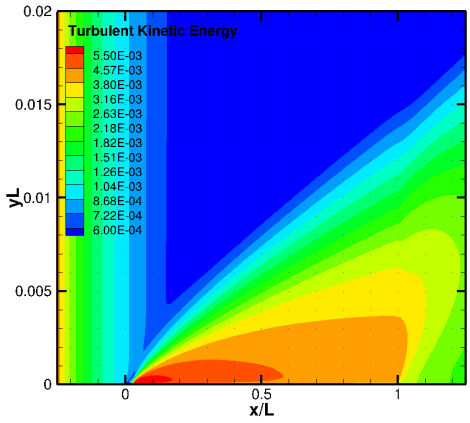

Figure 4.9: Turbulence Kinetic Energy map obtained with the RSM model for the experimental correlation data for the T3A case.

Looking at figures 4.6 and 4.8, it is possible to see that, as it is expected, the results for the $k-\omega$ SST model are identical to the experimental ones. However, the solutions for the RSM do present a small deviation from the experimental data. Since the formulation of the coupling SSG-LRR-ω had already been compared to other similar formulations from other sources in subsection 4.2.1 with satisfactory results, one can conclude that this difference arises from the inlet turbulence boundary conditions used. These had been tuned to be used with the $k-\omega$ SST model in [66], but may not be the most suitable to be used with the RSM. This prompts the research explained in subsection 4.4.3, of how sensitive are the models to the variation of these inlet turbulence boundary conditions.

4.3 Numerical Errors

After comparing the implementation of the SSG-LRR-ω in software ReFRESCO against both experimental data and results from other CFD codes, subsection 4.3.1 intends to illustrate the grid dependance of the RSM and compare it with the one of the $k-\omega$ SST model. The results for the $k-\omega$ SST model were obtained in another study [68], with a different set of grids, but with equal inlet turbulence boundary conditions to the ones used in this study. These are grouped in six different sets of inlet conditions, adopted from [68], which are given in 4.4:

Table 4.4: Inlet boundary conditions which are kept constant throughout the grid refinement study.

	T3AM		**T3A**		**T3B**	
	BC1	BC2	BC1	BC2	BC1	BC2
FSTI	0.01	0.01	0.05	0.05	0.07	0.07
EVR	7.55	0.10	12.67	0.10	99.15	0.10

These separate pairs of values aim to represent two different types of transition:

1. **T3AM** corresponds to a case where natural transition occurs;

2. **T3A** and **T3B** correspond to cases where bypass transition occurs;

4.3.1 Grid Dependance in the RSM and $k-\omega$ SST models

In this subsection, it is possible to verify how the solutions are affected by the grid refinement level, namely:

1. If the values of C_f converge to a solution when increasing grid refinement;

2. If the occurence of transition is affected by the different grid refinements;

This part of the study was performed by plotting the C_f variable against the Re_x variable, for all the case-studies described in table 4.4.

It was observed that, for all the BC1 conditions (whether for natural or bypass phenomena), there is always the occurrence of transition, independently of the grid refinement level. The latter will only influence the position of the transition: the finer the grid, the further downstream transition occurs. This is explicit in figures 4.10 to 4.15. Along all the simulations performed with the flat plate, the RSM demonstrated to have a satisfactory iterative convergence, with no major problems in reducing the residuals to negligible levels. However, it proved to have more difficulties in converging to a solution than the $k-\omega$ SST model, i.e., it took a larger number of iterations.

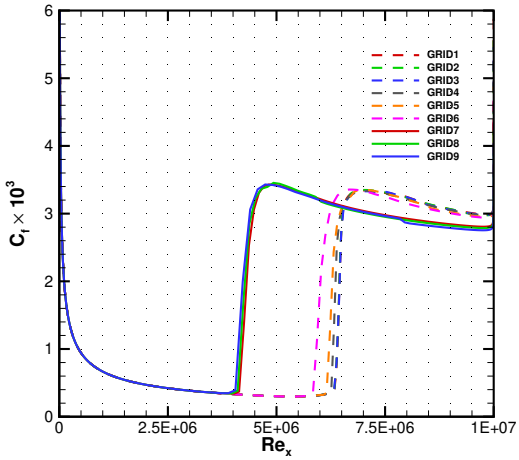

Figure 4.10: Evolution of the C_f distribution with the grid refinement level for the $T3AM-BC1$ condition for the RSM.

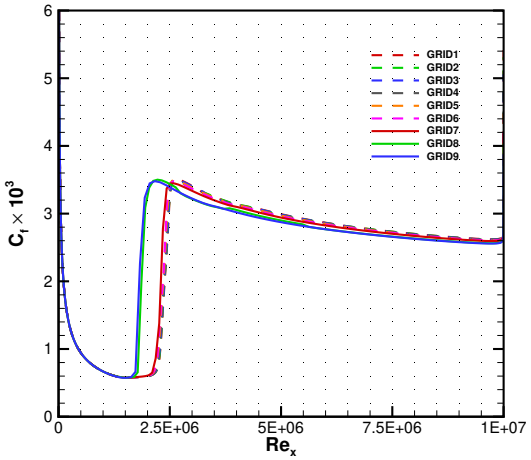

Figure 4.11: Evolution of the C_f distribution with the grid refinement level for the $T3AM-BC1$ condition for the $k-\omega$ SST.

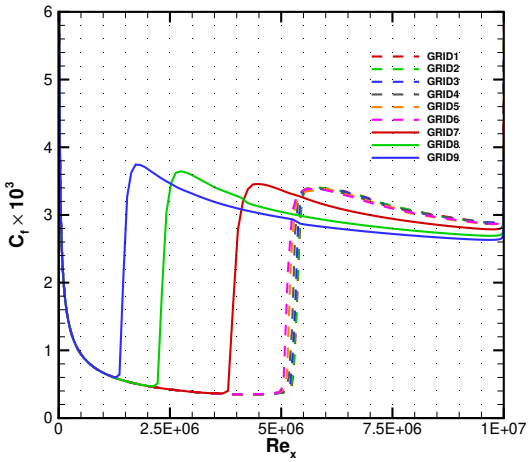

Figure 4.12: Evolution of the C_f distribution with the grid refinement level for the $T3A-BC1$ condition for the RSM.

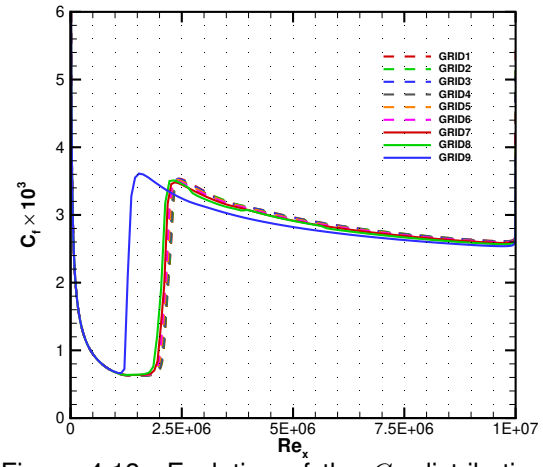

Figure 4.13: Evolution of the C_f distribution with the grid refinement level for the $T3A-BC1$ condition for the $k-\omega$ SST.

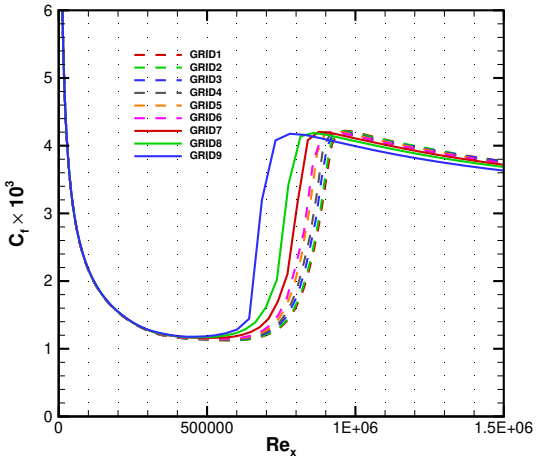

Figure 4.14: Evolution of the C_f distribution with the grid refinement level for the $T3B-BC1$ condition for the RSM.

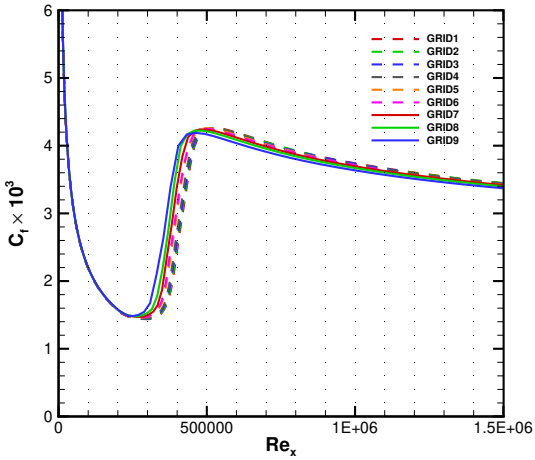

Figure 4.15: Evolution of the C_f distribution with the grid refinement level for the $T3B-BC1$ condition for the $k-\omega$ SST.

It is possible to see that when increasing the grid refinement, several phenomena occur:

1. In the T3A and T3AM solutions, where the inlet EVR and FSTI are lower, the results for the RSM present a larger discrepancy between grids than in the T3B solution;
2. The solutions for the finer grids tend to be closer to each other than the ones for the coarser grids;
3. The solutions for the $k-\omega$ SST model tend to be closer to each other than the ones for the RSM;

To illustrate this behaviour, figure 4.16 displays the evolution of the transition position x/L, with the increasing size of the grid cells h_i/h_1.

As per [69], one can obtain the numerical uncertainty for the calculation of the position of transition, depicted in figure 4.16 by the black error bars. The uncertainty was calculated only for the finest grid,

using the data from the five finest grids. This decision arises from the way the grids are set (see table 4.1), resulting in two sets of grids where the finest grid is twice as refined as the coarsest one: $grid1$ to $grid5$ and $grid5$ to $grid9$. Since the three coarsest grids display a considerably different behaviour from the others, it would not be reasonable to calculate this uncertainty using the set of the 5 coarsest grids. The values obtained for all the BC1 cases are expressed in table 4.5:

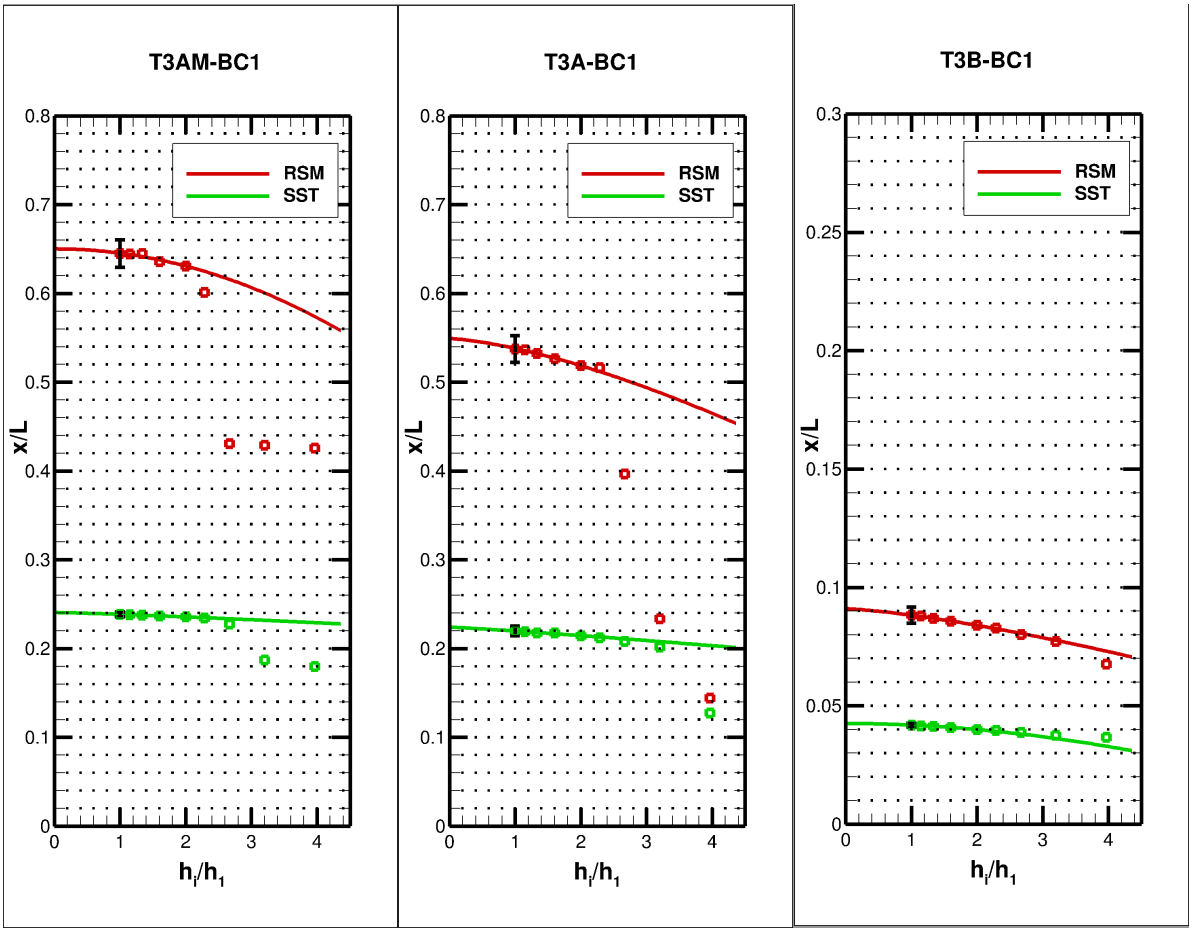

Figure 4.16: Evolution of transition position with the increasing level of grid refinement for the different turbulent inlet conditions. Bars representing the numerical uncertainty for the calculation of transition position for the finer grid are shown. The used axis scale is different in the rightmost figure.

Table 4.5: Values of uncertainty for the calculation of the transition position.

Case	RSM	$k-\omega$ SST
T3AM-BC1	0.015	0.003
T3A-BC1	0.015	0.005
T3B-BC1	0.003	0.001

Several aspects should be noticed:

1. In T3B-BC1 conditions, where the inlet EVR is considerably higher than in T3A-BC1 and T3AM-BC1, the uncertainty of the calculation of transition position is lower.

2. For all the conditions tested, the uncertainty in the calculated transition position is larger for the RSM than for the $k-\omega$ SST.

3. Regarding the RSM, there is a big convergence gap between the three coarsest grids and the others. So, when using the RSM model in future studies, care must be taken with the number of grids used and its level of refinement. In this case, if only the three coarsest grids were used for the RSM, the results would be precise, but inaccurate.

4. In the RSM, the difference between the results of the finest and coarsest grids is much more sizeable than in the $k-\omega$ SST model, which can indicate that the RSM may require finer grids when performing a similar simulation.

Looking at all the BC2 conditions, where the inlet eddy viscosity is considerably smaller (EVR=0.1) than in the BC1 condition, it is possible to see that the RSM only presents transition in the two coarser grids, remaining laminar in the seven finest grids. This behaviour does not occur for the $k-\omega$ SST. This is demonstrated in figures 4.17 and 4.18. Only the T3B-BC2 condition is depicted, but the behaviour obtained for the T3AM-BC2 and T3A-BC2 conditions is similar.

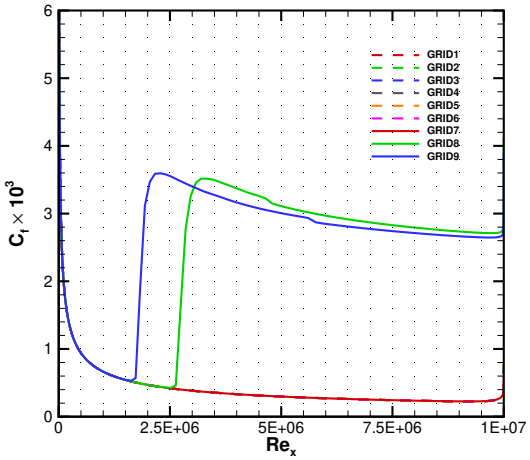

Figure 4.17: Evolution of the C_f distribution with the grid refinement level for the $T3B-BC2$ condition for the RSM.

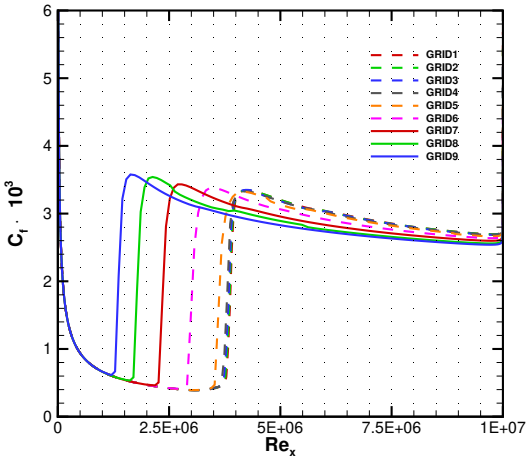

Figure 4.18: Evolution of the C_f distribution with the grid refinement level for the $T3B-BC2$ condition for the $k-\omega$ SST.

The results obtained in the finest grid, $grid1$ with the different inlet conditions, for both turbulence models (RSM and $k-\omega$ SST), are compiled in figure 4.19, which shows that when the inlet EVR is higher (the BC1 cases), the solutions for both models become more similar. In these cases, the C_f curves for the RSM and $k-\omega$ SST present analogous behaviour, but transition happens further downstream for the RSM model.

On the other hand, for every BC2 condition, where the inlet EVR is lower, the solution for the $k-\omega$ SST model features the occurrence of transition, while for the RSM it does not.

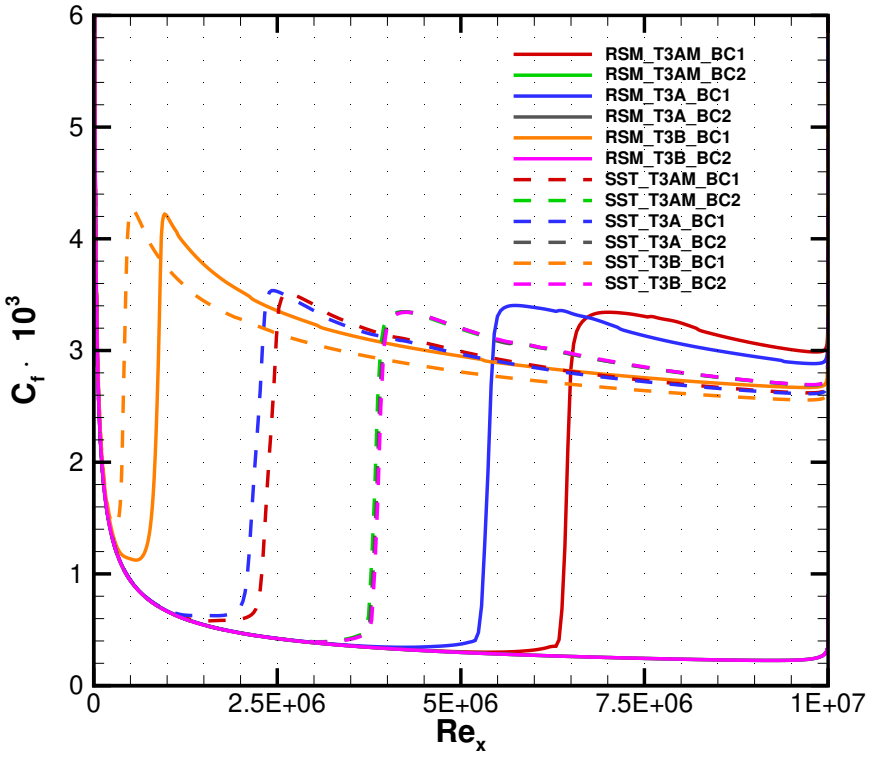

Figure 4.19: C_f distribution for all the different cases tested with the flat plate, with different inlet turbulence boundary conditions, for the RSM and the $k-\omega$ SST models.

4.3.2 Turbulence Kinetic Energy decay

In order to verify how the decay could possibly influence the ocurrence of transition, turbulence kinetic energy maps were produced, which allow to study the decay of this variable inside the study domain. These maps feature solutions of both the RSM and the $k-\omega$ SST model, for two different grids: $grid1$, the finest one, and $grid8$, the finest grid for which transition did occur in the RSM for the BC2 sub-condition.

The numerical solutions obtained for the decay of the turbulence kinetic energy with both the $k-\omega$ SST model and the RSM are also compared. These values are obtained in freestream along the domain, far away from the flat plate's surface.

For $grid8$ and T3B-BC2 condition, the turbulence kinetic energy in the vicinity of the boundary layer is shown in figures 4.20 and 4.21, for the RSM and $k-\omega$ SST models respectively. It is possible to see that transition was predicted by both models. Figure 4.22 has the values of turbulence kinetic energy in the freestream, for both models, also for the T3B-BC2 condition.

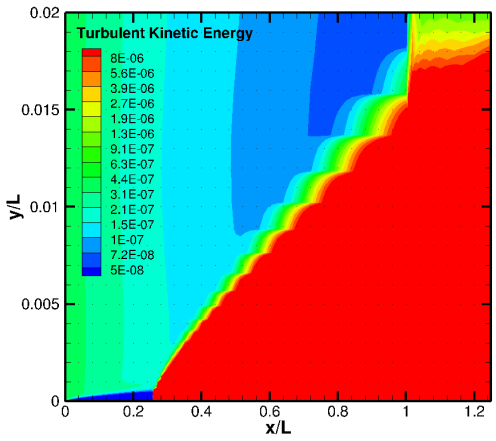

Figure 4.20: Turbulence Kinetic Energy for the $T3B-BC2$ condition for the SSG-LRR-ω using $grid8$.

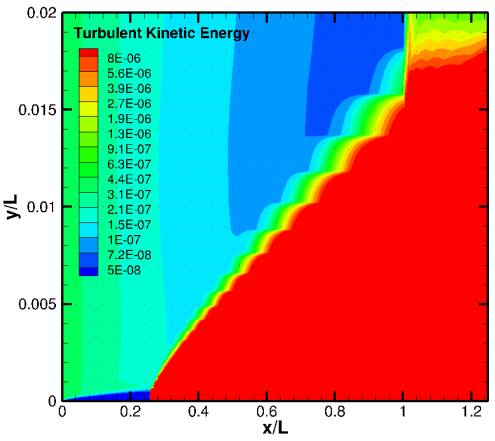

Figure 4.21: Turbulence Kinetic Energy for the $T3B-BC2$ condition for the $k-\omega$ SST using $grid8$.

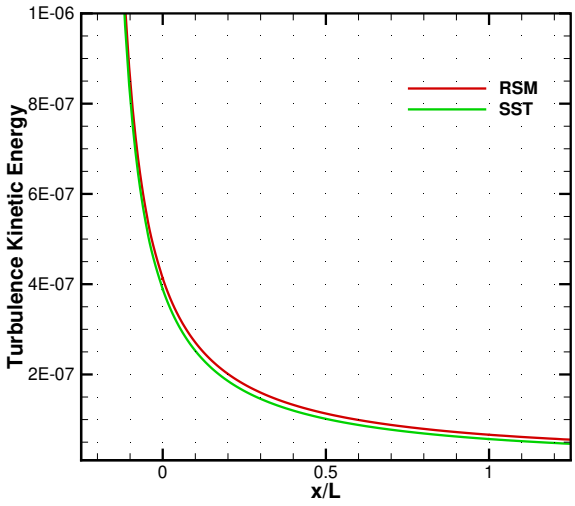

Figure 4.22: Curves representing the variation of the freestream turbulence kinetic energy along the domain in the x direction for both the RSM and the $k-\omega$ SST models for T3B-BC2 conditions using $grid8$.

For $grid1$ and conditions T3B-BC2, the turbulence kinetic energy in the vicinity of the boundary layer is shown in figures 4.23 and 4.24, for the RSM and $k-\omega$ SST models respectively. It is possible to see that only the $k-\omega$ solution presents transition, whilst the RSM remains laminar. Similarly to what has been done for $grid8$, figure 4.25 depicts the values of turbulence kinetic energy in the freestream, for both models, for the T3B-BC2 condition.

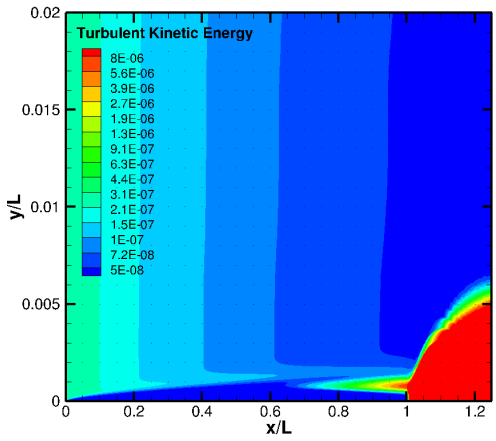

Figure 4.23: Turbulence Kinetic Energy for the $T3B-BC2$ condition for the SSG-LRR-ω using $grid1$.

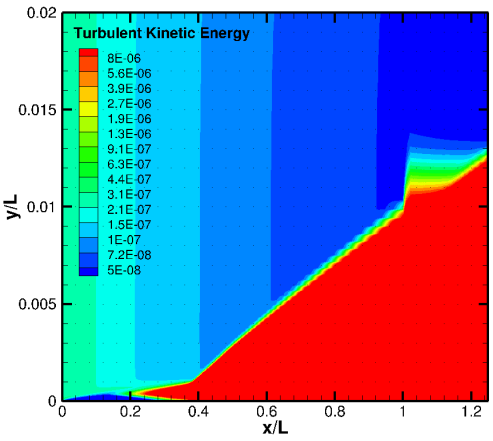

Figure 4.24: Turbulence Kinetic Energy for the $T3B-BC2$ condition for the $k-\omega$ SST using $grid1$.

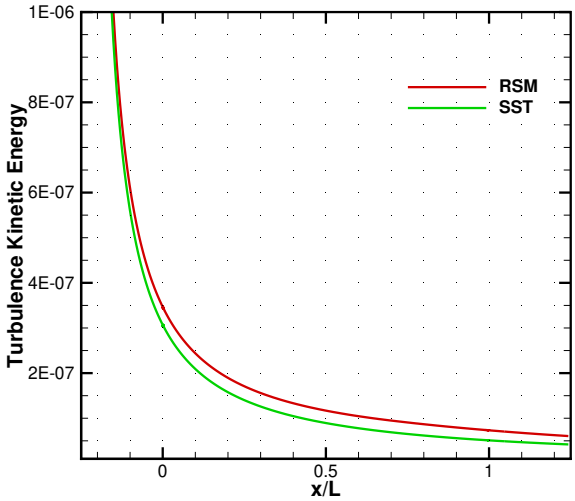

Figure 4.25: Curves representing the variation of the freestream turbulence kinetic energy along the domain in the x direction for both the RSM and the $k-\omega$ SST models for T3B-BC2 conditions using $grid8$.

By looking at figures 4.22 and 4.25, one sees that the freestream turbulence decay is similar in both models, in both situations, and thus it does not justify the differences in the models' transition prediction.

4.3.3 Conclusions

For this part of the study, one can infer several conclusions:

1. The RSM presents a greater grid dependence than the $k-\omega$ SST model;
2. The RSM needs finer grids than the $k-\omega$ when performing a similar simulation;
3. The prediction of decay of the turbulence kinetic energy is similar for both models;
4. The small difference in the decay prediction is not enough to justify differences in transition occurence between both models;
5. The difference between the $k-\omega$ SST model and the RSM is augmented when the inlet eddy viscosity is lower, meaning the RSM is especially sensitive to this flow property, which can justify the differences in transition occurence between both models;
6. The RSM model presents transition downstream of the experimental location, both for natural and bypass transition;
7. The uncertainty in the calculation of the position of transition with increasing grid refinement is larger in the RSM than in the $k-\omega$ SST, for the same set of grids;
8. The solution of the RSM obtained with ReFRESCO presents a similar behaviour to the results obtained with other codes, described in [2];

4.4 Influence of Inlet Boundary Conditions

In order to try to quantify how much more sensitive to the turbulence inlet conditions the RSM is when compared to the $k-\omega$ SST model, sensitivity studies were carried out. As mentioned in subsection 4.3.3 the location of transition predicted by the RSM appears to be more sensitive to the inlet turbulence boundary conditions than the $k-\omega$ SST model, and also more sensitive to the grid refinement level. Therefore, sensitivity coefficients were calculated for these two models. This is done by running simulations for small variations of the inlet turbulence boundary conditions FSTI and EVR. These simulations were performed with three different turbulence models: RSM, $k-\omega$ SST and the $k-\sqrt{k}L$ model.

The grid used in this study corresponds to $grid1$ explained in subsection 4.1.3. The discretization scheme is the same as explained in 3.4. The symmetry, outlet, top and surface of the plate's boundary conditions, the simulation stopping criteria are the same as described in subsection 4.1.3. The mathematical model applied to the Navier Stokes equations, the turbulence and transition models used are the same as described in subsection 2.1.

4.4.1 Inlet Boundary Conditions

As in the grid refinement studies, at the inlet boundary, the velocity is set equal to undisturbed flow conditions, meaning $V_x = V_\infty$ and $V_y = 0$. Specific values for turbulence kinetic energy and eddy viscosity are chosen.

In both types of transition (natural transition with T3AM set of values, and bypass transition for T3A), there are three different simulations:

1. A base one that will act as an original for comparison (based on the values from the AVT 313 workshop [66])
2. One where the value of FSTI is slightly changed and the EVR is maintained as the original, that will serve to calculate the FSTI sensitivity coefficient;
3. One where the value of EVR is slightly changed and the FSTI is maintained as the original, that will serve to calculate the EVR sensitivity coefficient;

These values are compiled in table 4.6:

Table 4.6: Inlet turbulence boundary conditions used for the determination of the sensitivity coefficients.

T3AM			
EVR	25	25	30
FSTI	0.01	0.02	0.01

T3A			
EVR	280	280	300
FSTI	0.05	0.06	0.05

4.4.2 Calculation of the Sensitivity Coefficients

The sensitivity coefficients quantify how much a quantity will vary when another quantity (from which the first one is dependant on) is varied by a fixed amount. In this case, they measure the variation of the x-coordinate (when changing the inlet EVR and the FSTI) for which the C_f is equal to a given value. In each simulation, three different C_f values were used, one corresponding to the beginning of the transition zone, one for the middle, and one for the end. This value of C_f is chosen visually, by looking at each simulation and noticing where the transition begins and ends. This C_f value is different in the T3AM and T3A case, since these comprise natural and bypass transition cases respectively, which imply a different C_f range during transition. Figures 4.26 and 4.27 depict this reasoning. The three horizontal grey lines are aligned with three different values of C_f, representing the beginning, middle and end of transition.

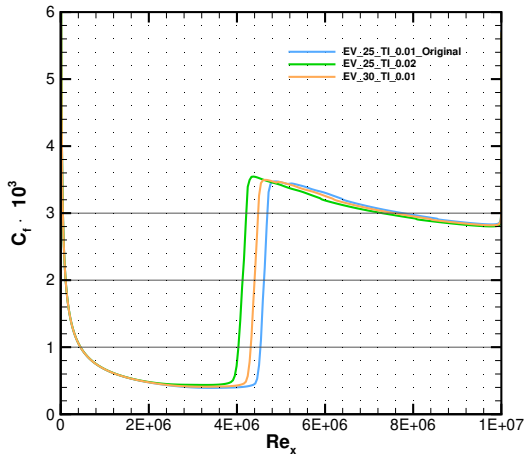

Figure 4.26: C_f distribution for the RSM model, using three different sets of inlet conditions, for the T3AM conditions. The three horizontal lines correspond to the three phases of transition: beginning, middle and end.

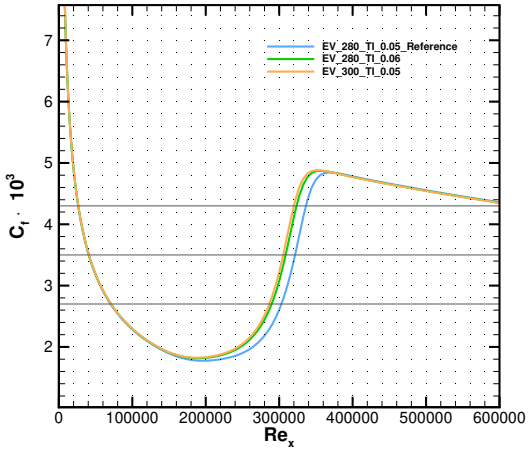

Figure 4.27: C_f distribution for the RSM model, using three different sets of inlet conditions, for the T3A conditions. The three horizontal lines correspond to the three phases of transition: beginning, middle and end.

Since, for each case, the variations between the three simulations are not significant, the values of C_f chosen are suitable for monitoring the transition in all of them. Bearing figure 4.26 as an example, one can calculate the turbulence intensity sensitivity coefficient, when $C_f = 1$, corresponding to the beginning of transition.

One must then know the x-coordinate for this C_f value, both for $FSTI = 0.01$ and $FSTI = 0.02$, displayed next:

Table 4.7: X-coordinate values used to calculate the FSTI sensitivity coefficient.

Turbulence Intensity	X-coordinate
0.01	0.4526
0.02	0.4026

With these values, one can use the formula:

$$\frac{f_{(x_{i+1})} - f_{(x_i)}}{x_{i+1} - x_i} \tag{4.11}$$

As proposed by [70], the sensitivity coefficient can be correctly calculated with different intervals between values. Replacing the values in table 4.7 in equation 4.11, one obtains:

$$\frac{0.4026 - 0.4526}{0.02 - 0.01} = -5 \tag{4.12}$$

Multiplying the result by x_i and dividing by $f(x_i)$ to normalize the coefficient:

$$\frac{-5 \times 0.01}{0.4526} = -0.1105 \tag{4.13}$$

4.4.3 Results

Doing a similar analysis for both transition types in the RSM model, both for the EVR and FSTI, in the beginning, middle, and end of the transition zone, it is possible to compile all the calculated sensitivity coefficients. Besides the RSM turbulence model, these coefficients were also calculated for the $k-\omega$ SST and the $k-\sqrt{k}L$ models, to provide a better term of comparison. Tables 4.8 and 4.9 feature the sensitivity coefficients calculated for the T3A and T3AM cases, respectively, with the three turbulence models.

Table 4.8: Sensitivity coefficients to the inlet turbulent boundary conditions calculated for the T3A case, for the beginning, middle, and end of transition, for the three different turbulence models: SSG-LRR-ω, $k-\omega$ SST and $k-\sqrt{k}L$.

T3A									
	Beginning of Transition			**Middle of Transition**			**End of Transition**		
	$k-\sqrt{k}L$	$k-\omega$ **SST**	**RSM**	$k-\sqrt{k}L$	$k-\omega$ **SST**	**RSM**	$k-\sqrt{k}L$	$k-\omega$ **SST**	**RSM**
Turbulence Intensity Sensitivity Coefficient	-0.079	-0.23	-0.32	-0.052	-0.18	-0.20	-0.042	-0.16	-0.19
Eddy Viscosity Ratio Sensitivity Coefficient	-0.67	-0.24	-1.07	-0.54	-0.20	-0.70	-0.50	-0.17	-0.68

Table 4.9: Sensitivity coefficients to the inlet turbulent boundary conditions calculated for the T3AM case, for the beginning, middle, and end of transition, for the three different turbulence models: SSG-LRR-ω, $k-\omega$ SST and $k-\sqrt{k}L$.

T3AM									
	Beginning of Transition			**Middle of Transition**			**End of Transition**		
	$k-\sqrt{k}L$	$k-\omega$ **SST**	**RSM**	$k-\sqrt{k}L$	$k-\omega$ **SST**	**RSM**	$k-\sqrt{k}L$	$k-\omega$ **SST**	**RSM**
Turbulence Intensity Sensitivity Coefficient	-0.067	-0.078	-0.11	-0.062	-0.071	-0.10	-0.061	-0.071	-0.10
Eddy Viscosity Ratio Sensitivity Coefficient	-0.18	-0.16	-0.24	-0.16	-0.14	-0.23	-0.14	-0.13	-0.23

Figures 4.28 and 4.29 help to visualise the values of the above tables:

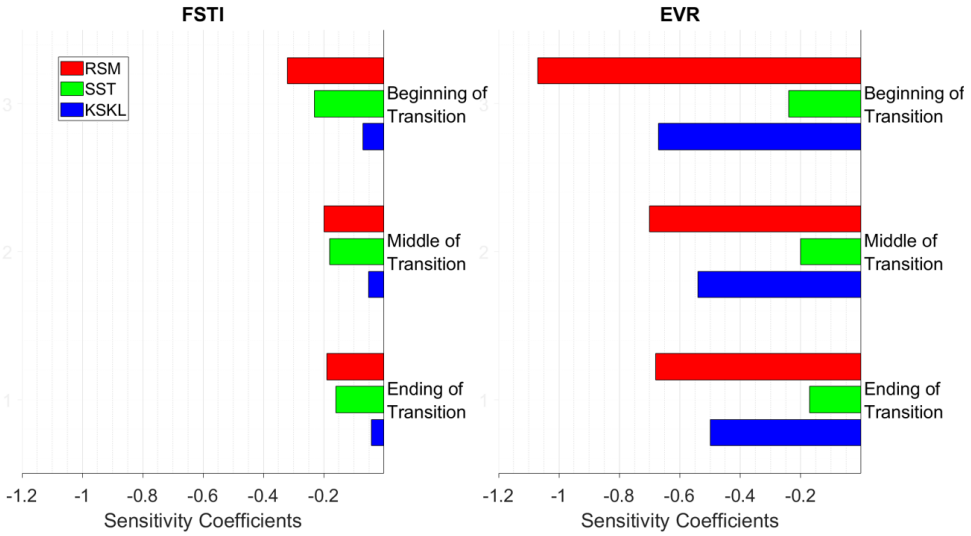

Figure 4.28: Sensitivity coefficients to the inlet turbulent boundary conditions calculated for the T3A case, for the beginning, middle, and end of transition, for the three different turbulence models: SSG-LRR-ω, $k-\omega$ SST and $k-\sqrt{k}L$.

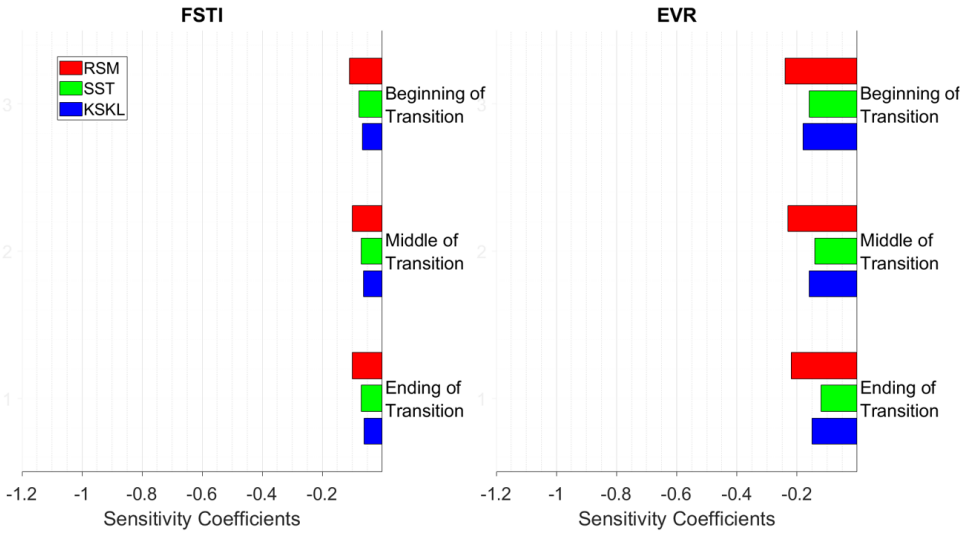

Figure 4.29: Sensitivity coefficients to the inlet turbulent boundary conditions calculated for the T3AM case, for the beginning, middle, and end of transition, for the three different turbulence models: SSG-LRR-ω, $k-\omega$ SST and $k-\sqrt{k}L$.

4.4.4 Conclusions

By looking at the sensitivity coefficients obtained, it is possible to draw some conclusions:

1. All the three turbulence models are more sensitive to changes in the inlet boundary conditions in the T3A case (bypass transition) case, where the base eddy viscosity ratio is higher;
2. The RSM is the most sensitive turbulence model, whether for the FSTI or EVR, in both natural and bypass transition;
3. The difference between the RSM and the $k-\omega$ SST model is larger in the EVR sensitivity coefficient than in the FSTI;
4. The difference between the RSM and the other models is the largest in the T3A (bypass transition) case, where the base eddy viscosity ratio is higher;
5. In almost all cases, sensitivity coefficients decrease towards the end of the transition, showing the decreasing influence of the inlet conditions along the transition region;
6. The $k-\sqrt{k}L$ model presents the lowest FSTI sensitivity coefficients. However, its EVR sensitivity coefficients are between the ones of the RSM and $k-\omega$ SST model. This suggests that this model presents a different behaviour than the other two, namely when predicting the decay of the inlet turbulence quantities, as explicit in [46].

Chapter 5

Airfoil Test-Case

The focus of this chapter is on the flow over the NLF1-0416 airfoil, and it is divided into two main sections. The first one, section 5.1, presents the definition of the problem, with the characterization of the domain, the boundary conditions and the numerical settings used. Then, section 5.2 comprises the results obtained for the various simulations performed in this test-case. This section is divided in two subsections. Firstly, subsection 5.2.1 includes studies regarding the sensitivity to inlet turbulence boundary conditions for both the SSG-LRR ω and the $k-\omega$ SST model. These aim to verify if the behaviour for the airfoil test-case is similar to the observed for the flat plate, where the RSM appears to be more sensitive to the inlet turbulence boundary conditions than the $k-\omega$ SST model. Sensitivity coefficients to the inlet turbulent boundary conditions were calculated for this test-case, similarly to what is presented for the flat plate test-case in section 4.4.3.

The second subsection, 5.2.2, features a comparison between the SSG-LRR-ω model and the $k-\omega$ SST model regarding their prediction of the location of transition, for similar conditions.

5.1 Problem Definition

5.1.1 Domain

The computational domain used in this study is a rectangle with the incoming flow V_∞ and the airfoil's chord c aligned with the horizontal direction x, with a zero angle of attack α. The leading edge of the airfoil is located at the origin of the (x, y) Cartesian coordinate system. The length of the domain in the x direction is 36c, with the inlet located at $x/c = -12$ and the outlet at $x/c = 24$. The domain has a height in the y direction of $24c$, being the top boundary of the domain located at $y/c = 12$ and the bottom boundary of the domain at $y/c = -12$.

The Reynolds number Re based on the undisturbed freestream velocity V_∞, chord of the airfoil c and kinematic viscosity of the fluid ν is given by equation 5.1:

$$Re = \frac{V_\infty c}{\nu} = 4 \times 10^6. \tag{5.1}$$

5.1.2 Boundary Conditions

There are five locations that require the specification of boundary conditions: the airfoil's surface, the inlet boundary, the outlet boundary, the top boundary and the bottom boundary.

Surface of the Airfoil

At the surface of the airfoil the boundary conditions used are identical to the ones described in subsection 4.1.2 for the flat plate.

Top and Bottom Boundary

At the top and bottom boundaries, all the flow variables have null normal derivatives in the vertical direction. The vertical velocity component is equal to zero ($V_y = 0$)

Outlet Boundary

At the outlet, streamwise derivatives equal to zero are applied to all dependent variables, except for the pressure, which is fixed and equal to zero.

Inlet Boundary

At the inlet boundary, the boundary conditions are identical to the ones described for the flat plate in subsection 4.1.2.

Inlet Turbulent Boundary Conditions

As proceeded in the flat plate test-case in subsection 4.4, specific values for inlet turbulence boundary conditions FSTI and EVR are set, in order to calculate the sensitivity coefficients to these two variables. For each calculation, there are three different simulations:

1. A base one that will act as an original for comparison.
2. One where the value of the inlet property being studied is slightly decreased and the other inlet property is maintained as the original, that will enable to calculate a "minus coefficient";
3. One where the value of the inlet property being studied is slightly increased and the other inlet property is maintained as the original that will enable to calculate an "plus coefficient";

The "minus" and "plus" coefficients have identical purposes, and the reason of considering them both, instead of a single coefficient as in subsection 4.4 with the flat plate test-case, is to have a broader set of information for comparison. The values used to calculate these sensitivity coefficients are compiled in table 5.1.

Table 5.1: Inlet turbulence boundary conditions used for the determination of the sensitivity coefficients to the inlet EVR and FSTI for the airfoil test-case.

EVR			
EVR($\frac{\mu_t}{\mu}$)	45	50	55
FSTI	0.03	0.03	0.03

FSTI			
EVR($\frac{\mu_t}{\mu}$)	50	50	50
FSTI	0.02	0.03	0.04

5.1.3 Numerical Settings

Grids

All the simulations in the airfoil test-case were performed using the same grid, taken from a previous study [59]. Similarly to the ones used in the flat plate test-case, this is comprised by several structured blocks, which feature different levels of refinement according to their location in the domain. Two preliminary calculations were performed with coarser grids, to evaluate the iterative convergence of the model, and tune the relaxation factors mentioned in subsection 3.4.4. The successively used grids are different but geometrically similar, each one of them being twice as refined as the previous one along the airfoil surface. The number of cells in each grid are displayed in table 5.2. Grids $grid-1$ and $grid-2$ were run to tune the relaxation parameters, and then $grid-3$ was used to perform all the simulations in this test-case.

Figures 5.1 to 5.4 depict the different blocks used to form $grid-1$, the coarser one. The different levels of refinement are patent in the different parts of the domain. Figure 5.4 intends to highlight the detail of the mesh used near the airfoil surface, in order to best capture the near-wall phenomena. $grid-3$ presents a similar geometry, but it is four times more refined.

Table 5.2: Number of cells on the surface of the airfoil, total number of cells, and $((y_n^+)_c)_{max}$ of the different grids used in the airfoil test-case.

	Number of cells on the airfoil's surface	**Total number of cells**	$((y_n^+)_c)_{max}$
grid-1	512	47616	6.67
grid-2	1024	190464	0.63
grid-3	2048	761856	0.33

Simulation Stopping Criteria

The stopping criteria used in these simulations was a convergence tolerance of 10^{-8} for the residuals of certain variables, namely V_i, P, γ and Re_θ. The residual norm used was the L^∞ norm, which

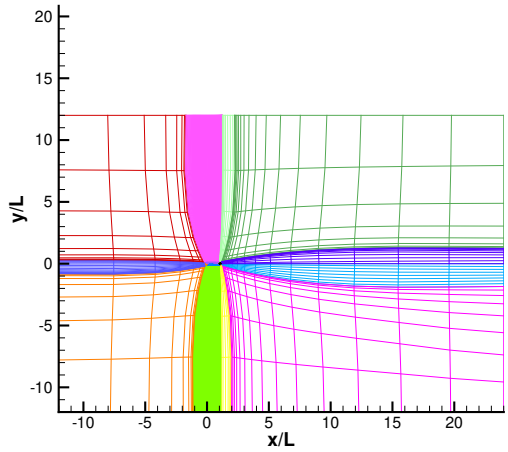

Figure 5.1: Different blocks that comprise the grid used in the airfoil test-case highlighted in different colours - view of the entire domain.

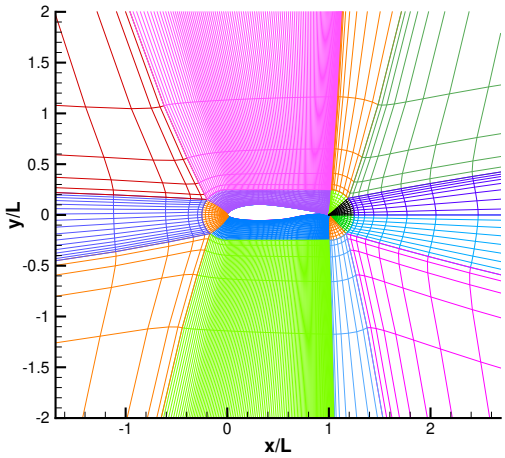

Figure 5.2: Different blocks that comprise the grid used in the airfoil test-case highlighted in different colours - zoomed view.

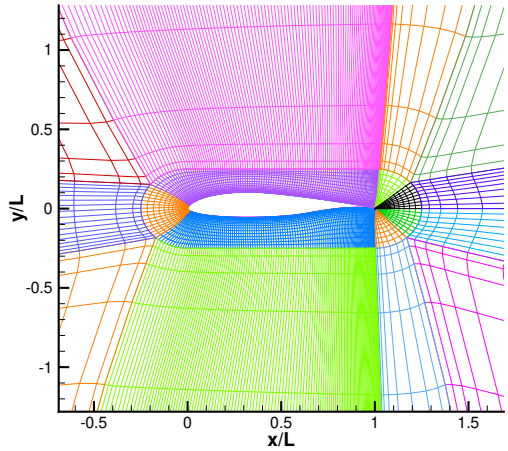

Figure 5.3: Different blocks that comprise the grid used in the airfoil test-case highlighted in different colours - zoomed view.

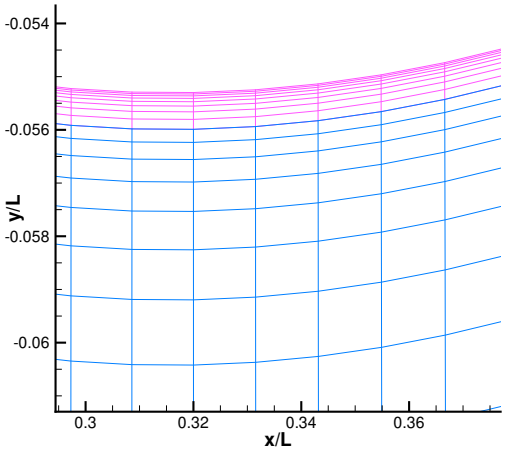

Figure 5.4: Different blocks that comprise the grid used in the airfoil test-case highlighted in different colours - surface detail.

considers only the maximum residual value of a given variable in the entire grid.

The residuals of the turbulence-solving equation were exempted from this criteria, as explained in section 4.1.3.

5.1.4 Sensitivity Coefficients Calculations

The calculation of the inlet turbulence boundary conditions for the airfoil test-case followed the same reasoning described in subsection 4.4.2 for the flat plate test-case. The C_f values used to calculate the coefficients are highlighted with horizontal bars, both for the upper and lower surface of the airfoil, in figures 5.5 and 5.6 for the SSG-LRR-ω and the $k-\omega$ SST models respectively.

In this section, besides using the values of these properties at the inlet in the denominator of equation 4.11, two additional sets of sensitivity coefficients were calculated, with the denominator of equation 4.11

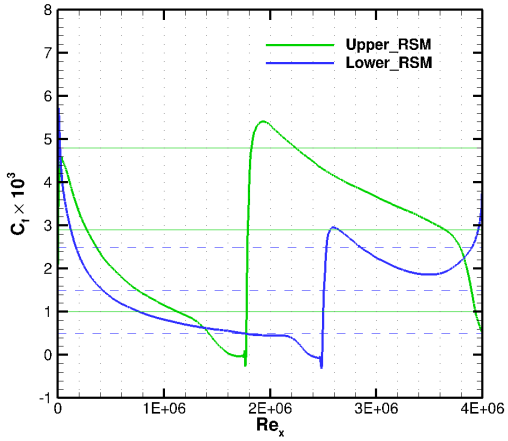

Figure 5.5: C_f distribution for the RSM model. The three horizontal lines correspond to the three phases of transition: beginning, middle and end. The filled green bars match the chosen C_f values for the upper surface, and the dashed blue lines for the lower surface.

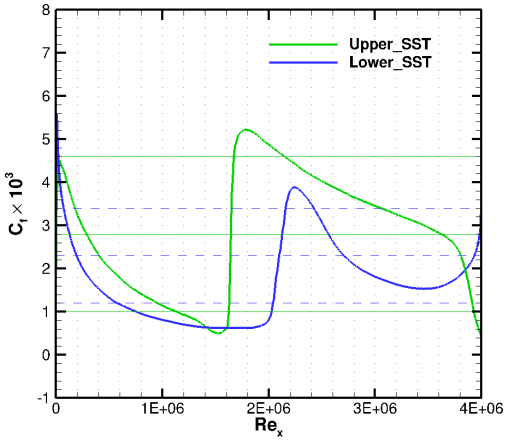

Figure 5.6: C_f distribution for the $k-\omega$ SST model. The three horizontal lines correspond to the three phases of transition: beginning, middle and end. The filled green bars match the chosen C_f values for the upper surface, and the dashed blue lines for the lower surface.

featuring the Tu and EVR values in two distinct locations: at a distance of $1c$ from the airfoil's leading edge, $11c$ downstream of the inlet, and at the leading edge itself. The purpose of doing so is to confirm that calculating sensitivity coefficients at a position far downstream of the inlet is unreasonable, since the decay of turbulence quantities causes the changes in their inlet values to be poorly represented in regions near the leading edge of the airfoil.

5.2 Results

5.2.1 Sensitivity Coefficients

The leading edge of the airfoil is located far downstream - $12c$ - of the inlet, a considerably larger value than what was verified in the flat plate test-case, where the leading edge was located $0.25L$ downstream of the inlet. Therefore, there will be a higher decay of the different turbulent quantities specified at the inlet, with them reaching the assymptotic region described in subsection 3.2 near the leading edge of the airfoil. This will cause these variables to have fairly similar values in that location, and thus the inlet turbulence boundary conditions sensitivity coefficients are expected to be much smaller than the ones observed for the flat plate.

The sensitivity coefficients obtained with the turbulence quantities at the three locations specified in subsection 5.1.4 with both the SSG-LRR-ω and the $k-\omega$ SST models are displayed in table 5.3, using the C_f distribution for the upper surface of the NLF1-0416 airfoil. For the lower surface of the airfoil, coefficients are displayed in table 5.4.

Table 5.3: Sensitivity coefficients to the inlet turbulent boundary conditions obtained with the C_f distribution for the upper surface of the NLF1-0416 airfoil using the SSG-LRR-ω and the $k-\omega$ SST models.

Upper Surface								
			Beginning of Transition		**Middle of Transition**		**End of Transition**	
			Minus Coefficient	**Plus Coefficient**	**Minus Coefficient**	**Plus Coefficient**	**Minus Coefficient**	**Plus Coefficient**
FSTI	RSM	Inlet	1.260_E-4	8.342_E-5	1.698_E-4	1.051_E-4	2.457_E-4	2.365_E-4
		11x/c	-2.254_E-3	-2.217_E-3	-3.032_E-3	-2.603_E-3	-4.398_E-3	-4.717_E-3
		12x/c	-2.331_E-3	-2.060_E-3	-2.943_E-3	-2.488_E-3	-4.257_E-3	-4.506_E-3
	$k-\omega$ SST	Inlet	-7.200_E-4	8.132_E-5	-4.768_E-4	5.101_E-5	-5.177_E-4	6.465_E-4
		11x/c	-1.285_E-2	-1.211_E-3	-8.505_E-3	-7.638_E-4	-9.224_E-3	-9.432_E-4
		12x/c	-1.243_E-2	-1.197_E-3	-8.627_E-3	-7.431_E-4	-9.362_E-3	-9.545_E-4
EVR	RSM	Inlet	-3.255_E-2	-3.372_E-2	-3.305_E-2	-3.342_E-2	-3.236_E-2	-3.135_E-2
		11x/c	-2.982_E-2	-3.092_E-2	-3.025_E-2	-3.055_E-2	-2.957_E-2	-2.866_E-2
		12x/c	-2.982_E-2	-3.092_E-2	-3.025_E-2	-3.055_E-2	-2.957_E-2	-2.866_E-2
	$k-\omega$ SST	Inlet	-6.645_E-2	-5.982_E-2	-5.572_E-2	-5.322_E-2	-6.522_E-2	-5.945_E-2
		11x/c	-6.090_E-2	-5.598_E-2	-5.169_E-2	-4.883_E-2	-5.977_E-2	-5.443_E-2
		12x/c	-6.090_E-2	-5.598_E-2	-5.169_E-2	-4.883_E-2	-5.977_E-2	-5.443_E-2

Table 5.4: Sensitivity coefficients to the inlet turbulent boundary conditions obtained with the C_f distribution for the lower surface of the NLF1-0416 airfoil using the SSG-LRR-ω and the $k-\omega$ SST models.

Lower Surface								
			Beginning of Transition		**Middle of Transition**		**End of Transition**	
			Minus Coefficient	**Plus Coefficient**	**Minus Coefficient**	**Plus Coefficient**	**Minus Coefficient**	**Plus Coefficient**
FSTI	RSM	Inlet	2.886_E-5	2.743_E-5	4.787_E-5	3.811_E-5	6.010_E-5	5.717_E-5
		11x/c	-4.884_E-4	-5.746_E-4	-8.092_E-4	-9.293_E-4	-1.073_E-3	-4.954_E-4
		12x/c	-4.991_E-4	-5.482_E-4	-8.319_E-4	-8.872_E-4	-1.039_E-3	-4.910_E-4
	$k-\omega$ SST	Inlet	1.476_E-3	2.354_E-4	1.577_E-3	1.661_E-4	1.200_E-3	9.457_E-5
		11x/c	-2.621_E-2	-3.511_E-3	-2.801_E-2	-2.480_E-3	-2.144_E-2	-1.413_E-3
		12x/c	-2.543_E-2	-3.484_E-3	-2.712_E-2	-2.451_E-3	-2.070_E-2	-1.404_E-3
EVR	RSM	Inlet	-4.513_E-3	-1.816_E-3	-5.436_E-3	-3.513_E-3	-2.778_E-2	-7.385_E-3
		11x/c	-4.142_E-3	-1.592_E-3	-4.972_E-3	-3.222_E-3	-2.500_E-3	-6.772_E-3
		12x/c	-4.142_E-3	-1.592_E-3	-4.972_E-3	-3.222_E-3	-2.500_E-3	-6.772_E-3
	$k-\omega$ SST	Inlet	-1.663_E-1	-1.706_E-1	-1.563_E-1	-1.573_E-1	-1.554_E-1	-1.475_E-1
		11x/c	-1.523_E-1	-1.556_E-1	-1.428_E-1	-1.442_E-1	-1.419_E-1	-1.418_E-1
		12x/c	-1.523_E-1	-1.556_E-1	-1.428_E-1	-1.442_E-1	-1.419_E-1	-1.418_E-1

The EVR and the FSTI do not decrease exactly in the same way. Table 5.5 presents the values of FSTI and EVR defined at the inlet, and in a location of $11x/c$ downstream from it. The decay of the EVR is such that the variations between the different simulations remain relatively similar in both locations. On the other hand, the decay for the FSTI is much more accentuated, meaning the variations between values set at the inlet is one order of magnitude larger than the ones documented $11c$ downstream of it. Since the variation between values of the EVR is nearly constant along the domain, one should expect the sensitivity coefficients calculated for the different locations to be fairly similar. Elseways, with the FSTI, since the variation decreases significantly along the domain, the coefficients are expected to increase near the airfoil's leading edge when comparing with the inlet ones. This behaviour can also be illustrated by figure 5.7, that feaures the analytical solution for equation 3.5, for different inlet turbulence boundary conditions, in a portion of the domain from the inlet to the LE. These different conditions are summarized in table 5.5. It can be assessed that when there is a variation of the EVR at the inlet, that difference is maintained along the domain up to the LE of the airfoil - the cases of the solid green line and the dashed pink line. However, when there are changes in the inlet FSTI, the inlet value of k can be the same in two simulations, but have a fairly different decay along the domain - the cases of the solid green line and the dashed blue line.

Table 5.5: Inlet turbulence boundary conditions used for the determination of the sensitivity coefficients to the inlet EVR and FSTI for the airfoil test-case.

Decay Study Cases			
EVR($\frac{\mu_t}{\mu}$)	45	55	55
FSTI	0.03	0.03	0.05

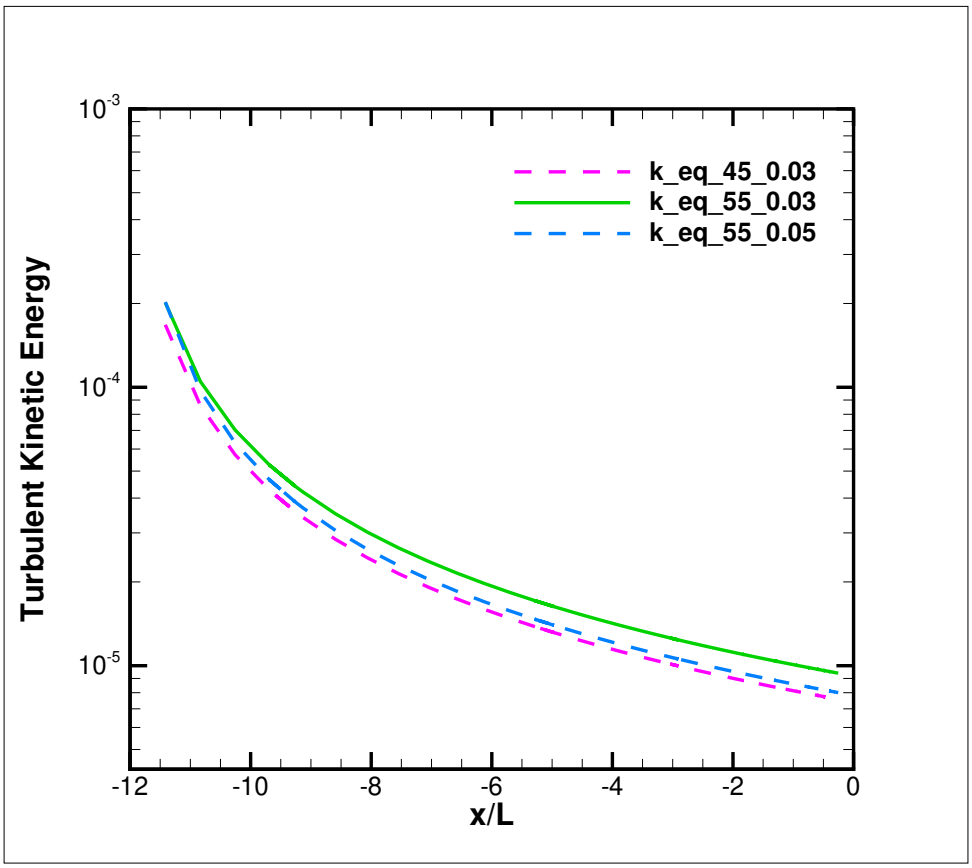

Figure 5.7: Analytical solution for the turbulent kinetic energy decay along the domain for three different cases.

Table 5.6: Values of the turbulence quantities of the different simulations, at the inlet and at a distance of $11c$ downstream from it. The variation of values between simulations is displayed for the two locations, in percentage.

			Variation		**Variation**	
EVR	**Inlet**	45	**9%**	50	**10%**	55
	11 x/c	29.8950	**12%**	33.5195	**11%**	37.1750
FSTI	**Inlet**	0.02	**50%**	0.03	**30%**	0.04
	11 x/c	0.002535	**3%**	0.002464	**2%**	0.002409

From tables 5.3 and 5.4, some conclusions can be withdrawn:

1. The overall coefficients calculated at the inlet are considerably small, and therefore should not be accepted as significant, since they do not fairly represent the variations of the inlet turbulence boundary conditions in regions close to the airfoil.

2. In general the plus coefficients are smaller than the minus coefficients. This is justified by the fact that for higher values of the inlet turbulence quantities, the decay will be more accentuated, and the values of sensitivity obtained of both the $k-\omega$ SST and the RSM is going to decrease.

3. Both the FSTI and EVR inlet coefficients are larger for the $k-\omega$ SST model than for the RSM, but within the same order of magnitude;

4. For both models, the inlet coefficients are much smaller for the FSTI than for the EVR, with the difference being of two orders of magnitude;

5. There is not a clear trend among the coefficients regarding their position in transition, whether in the beggining, middle or end of it.

6. The minus coefficients are usually larger than the plus coefficients, with a significant difference between them, altough in the same order of magnitude. This enforces the idea that this sensitivity analysis does not produces fruitful conclusions: starting from the base values, the results should be fairly similar whether the interval used to calculate the coefficients is added or subtracted - minus and plus coefficients - and that is not verified.

7. For the FSTI, in both models is verified a decrease of the value of the coefficients between the inlet and the regions near/at the leading edge of the airfoil. That reduction is of similar value in both models - one order of magnitude;

8. For the EVR, with both models, there is a slight decrease of the sensitivity coefficients between the inlet and the regions near/at the leading edge of the airfoil, but they remain in the same order of magnitude for the three locations;

Figure 5.8 shows a map of turbulence kinetic energy along the domain, where is patent the accentuated decay of this variable, reaching an assymptotic behaviour in a region far upstream of the airfoil.

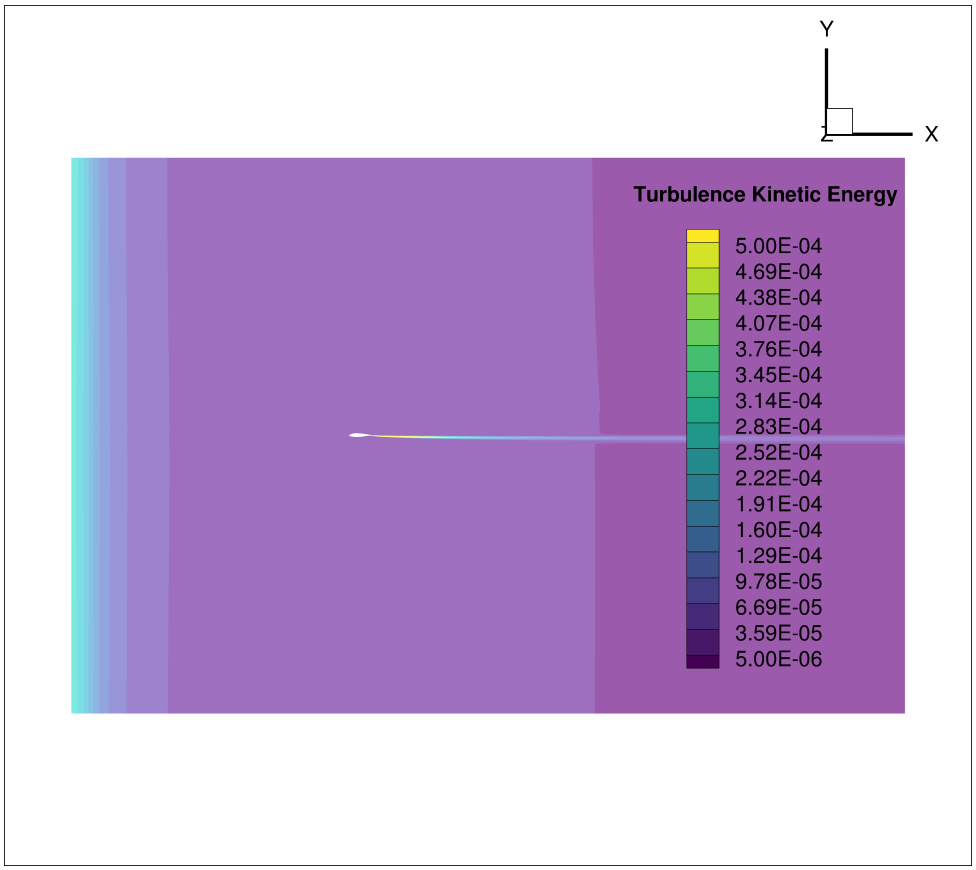

Figure 5.8: Turbulent kinetic energy decay along the domain. It is possible to see that the inital decay - near the leading edge - is abrupt, and then it tends to a stable, assymptotic behaviour. The airfoil is located in the middle of the image, and it is possible to see the wake it produces.

5.2.2 Comparison between the $k-\omega$ SST and the SSG-LRR-ω

The results obtained for all the cases described in table 5.1, used to calculate the sensitivity coefficients in subsection 5.2.1, were extremely similar. The curves of C_f for the upper and lower surfaces of the airfoil, both for the RSM and the $k-\omega$ are depicted in figure 5.9:

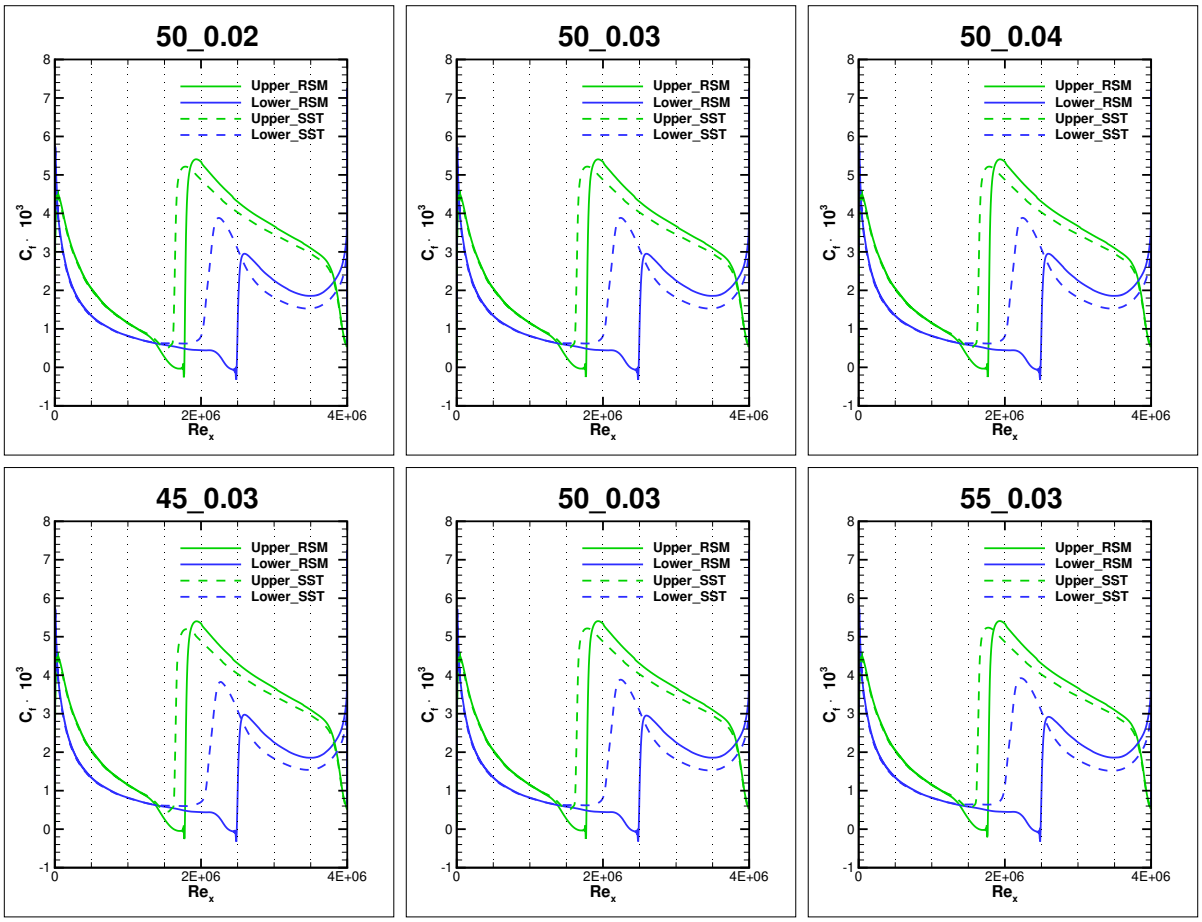

Figure 5.9: C_f curves obtained for the five different sets of turbulent inlet conditions, both for the SSG-LRR-ω and the $k-\omega$ SST. The filled lines represent the reults obtained for the SSG-LRR-ω model and the dashed lines for the $k-\omega$ SST model. Green lines correspond to the results for the upper surface, and blue lines for the lower surface.

Analysing the results, several aspects can be noticed:

1. The $k-\omega$ SST predicts transition upstream of the SSG-LRR-ω, both for the upper and lower surface;

2. The SSG-LRR-ω presents a region with negative C_f values just before the start of transition. This implies that, in the RSM, the adverse pressure gradient makes the laminar boundary layer separate before the transition to turbulent regime. This does not happen in the $k-\omega$ SST;

3. In the laminar regime, the C_f value predicted by both models is similar. However, after transition occurs, the SSG-LRR-ω predicts a slightly higher value of C_f.

4. The difference between both models in the prediction of transition position is smaller in the upper surface, where the pressure gradient is more adverse, when compared to the lower surface;

Chapter 6

Spheroid Test-Case

This chapter presents the analysis of the flow over a 6:1 spheroid at an angle of attack of 5° . The goal of this chapter is to evaluate how the RSM behaves in predicting transition over the surface of the spheroid, and compare it with the results obtained for the $k-\omega$ SST model. It is eventually shown that the inlet conditions tuned for being used with the $k-\omega$ SST may not be the most suitable to be used with the SSG-LRR-ω, even though the transition model coupled with both these models is the same.

It was chosen not to perform a sensitivity analysis for the prolate spheroid test-case, since it had already been concluded with the airfoil test-case in subsection 5.2.1 that for test-bodies located far downstream of the domain, sensitivity coefficients with the inlet boundary conditions do not present fruitful conclusions.

6.1 Problem Definition

6.1.1 Domain

The 6:1 prolate spheroid with length L is embedded in a three dimensional computational domain, shaped like a rectangular prism, with a length of $200L$ a height of $200L$ and a width of $100L$. The incoming flow V_∞ is alligned with the horizontal direction x. The major axis of the spheroid is parallel to the xy plane, and is oriented in an angle of attack α of 5° with the x direction. The center of the spheroid is located at the origin of the (x, y, z) Cartesian coordinate system. The inlet is located at $x/L = -100$ and the outlet at $x/L = 100$. The domain has a lateral boundary located at $z/L = 100$ and a symmetry boundary condition at $z/L = 0$. The top boundary of the domain is placed at $y/L = 100$ and the bottom boundary of the domain at $y/L = -100$.

The Reynolds number Re based on the undisturbed freestream velocity V_∞, length of the spheroid L and kinematic viscosity of the fluid ν is given by equation 6.1:

$$Re = \frac{V_\infty L}{\nu} = 6.5 \times 10^6. \tag{6.1}$$

6.1.2 Boundary Conditions

There are six locations that require the specification of boundary conditions, similarly to what is verified for the airfoil test-case: the inlet boundary, the surface of the spheroid, the top, bottom and side boundary, the outlet boundary and the symmetry boundary.

Surface of the Spheroid

At the surface of the spheroid the boundary conditions used are identical to the ones described in subsection 4.1.2 for the flat plate.

Top and Bottom Boundary

At the top and bottom boundaries, the boundary conditions used are the same as the ones used for the airfoil test-case, described in subsection 5.1.2.

Lateral Boundaries

At the lateral boundaries, the boundary conditions used are the same as the ones used for the top and bottom boundaries of the airfoil test-case, described in subsection 5.1.2.

Outlet Boundary

At the outlet, the boundary conditions used are the same as the ones used for the airfoil test-case, described in subsection 5.1.2.

Symmetry Boundary

Similarly to what is described in subsection 4.1.2 for the flat plate test-case. a symmetry boundary condition is applied in the domain of the spheroid test-case, at $z = 0$.

Inlet Boundary

At the inlet boundary, the boundary conditions are identical to the ones described for the flat plate in subsection 4.1.2.

Inlet Turbulent Boundary Conditions

Altough sensitivity coefficients were not calculated, different inlet boundary conditions were used in different simulations performed in this test-case. The values of each simulation and the reasoning behind them will be explained in subsection 6.2.

6.1.3 Numerical Settings

Grids

The simulations of the spheroid test-case were performed using always the same grid, which is comprised by several structured blocks. This grid was the coarser one from a set of five grids, but it was decided to use it instead of the finer ones due to the lack of computational power/cluster time available. This grid had been already used in a previous study [60] and was therefore adopted for this work. Figures 6.1 to 6.4 intend to represent different parts of this grid that are worth noticing. Table 6.1 presents the main characteristics of it.

Table 6.1: Number of cells on the surface of the spheroid, total number of cells, and $((y_n^+)_c)_{max}$ of the grid used in the spheroid test-case.

	Number of cells on the spheroid's surface	**Total number of cells**	$((y_n^+)_c)_{max}$
grid-spheroid	31504	5303536	0.72

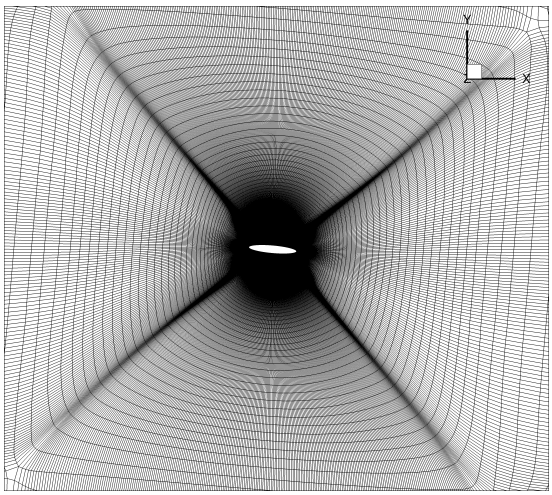

Figure 6.1: Depiction of the grid in the regions near the spheroid. The "cross" in the mesh is due only to visual effects, and does not intend to represent any additional local refinement.

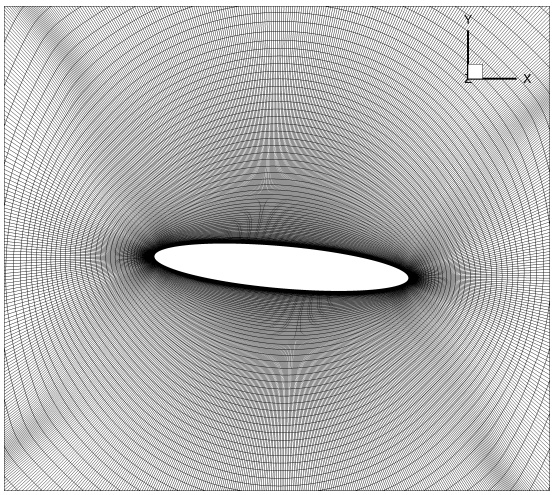

Figure 6.2: Zoomed view of the grid used around the spheroid test-body. It is possible to see the additional refinement employed near the body.

6.1.4 Simulation Stopping Criteria

The simulation stopping criteria used for the spheroid test-case is identical to the one described for the flat plate test-case, in subsection 4.1.3.

6.2 Results

The values used in the initial simulation - Case1 - provide a value of 0.15% of Tu in the leading edge of the spheroid, to match the values proposed by [71], for a simulation with the 6:1 prolate spheroid

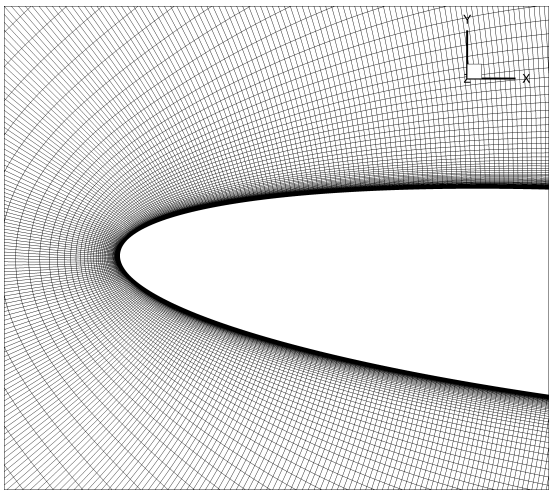

Figure 6.3: Detailed view of the grid zoomed near the leading edge of the spheroid. The grid is considerably more refined in the regions adjacent to the body, to better capture the near-wall phenomena.

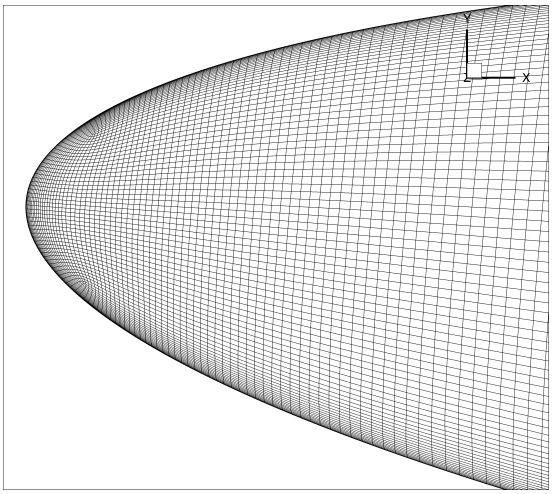

Figure 6.4: Depiction of the grid used on the spheroid's surface, near its leading edge. This grid structure is symmetric in relation to the spheroid's mid planes, and so the region near the trailing edge will present an identical configuration.

test-case with the $k-\omega$ SST model. This simulation did not converge, and presented a large region of laminar separation. On the other hand, for the same inlet turbulence boundary conditions, the $k-\omega$ SST model, without crossflow transition prediction, presented transition to turbulent regime, and a considerably smaller separation bubble upstream of it. This can be observed in figures 6.5 and 6.6. Upon this conclusion, several cases were run, trying to evaluate how the turbulence inlet conditions affected the solution. These cases are presented in table 6.2, that informs if a simulation was run with or without the $\gamma - Re_\theta$ transition model, the value of the turbulence quantities FSTI and EVR at the inlet, and at the leading and trailing edges of the spheroid, obtained with equations 3.5 and 3.6. It also tells if the results presented flow separation, and if the simulation had a sucessful iterative convergence or not. The reasoning behind the chosen values for each simulation ought to be explained:

- Case2 was run with same conditions as Case1, but with no transition model, to perceive if the difference in the transition prediction between Case1 and the results obtained for the $k-\omega$ SST were related to the coupling with the $\gamma - Re_\theta$ transition model;

- Since Case2 did converge, the inlet turbulence quantities were increased, to the values of Case3, and the transition model was again coupled with the SSG-LRR-ω. Cases 3 to 6 were run in order to find a lower limit of the turbulence quantities in the LE of the spheroid for which the SSG-LRR-ω + $\gamma - Re_\theta$ did not converge anymore, which was achieved in Case6. Due to the increased inlet turbulence quantitites, these simulations did not present laminar separation bubble, as in Case1. This can be seen in figure 6.7;

- Case7 had the goal of mimicking the turbulence intensity at the leading edge of Case6, but with a much higher value of EVR and lower value of FSTI at the inlet, to verify if the iterative convergence was achieved for the same conditions at the LE but with a higher EVR at the inlet;

- Finally Case8 was run to perceive if iterative convergence was achieved with the lower value of FSTI at the LE with which the simulation had converged - Case5, but with a higher value of inlet FSTI, and the lowest possible value of EVR at the inlet [59].

Table 6.2: Description of all the cases used to study the flow over the 6:1 spheroid, regarding the usage of transition model, the turbulence quantities in several points, flow separation, and iterative convergence. In the penultimate column, "Sep." stands for "flow separation".

Case	Transition Model	Inlet EVR	Inlet FSTI (%)	LE EVR	LE FSTI (%)	TE EVR	TE FSTI (%)	Sep.	Status
1	Yes	250	0.5	206.455	0.151	206.295	0.150	Yes	Not Converged
2	No	250	0.5	206.455	0.151	206.295	0.150	No	Converged
3	Yes	8000	5	6024.222	0.849	6019.186	0.845	No	Converged
4	Yes	8000	0.58	7800.101	0.495	7798.382	0.494	No	Converged
5	Yes	800	0.58	703.606	0.260	703.133	0.259	No	Converged
6	Yes	800	0.35	746.110	0.226	745.751	0.226	-	Not Converged
7	Yes	2000	0.257	1959.496	0.226	1959.137	0.226	-	Not Converged
8	Yes	800	2.78	547.357	0.259	546.888	0.258	No	Converged

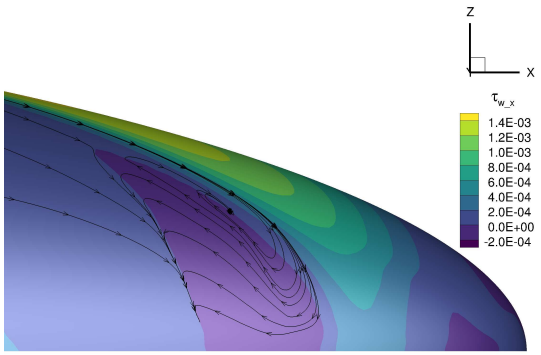

Figure 6.5: Map of the skin-friction in the x direction on the surface of the spheroid using the SSG-LRR ω model with 0.15 $\%$ of FSTI at the LE of the spheroid. The streamlines show the recirculation of the flow inside the large separation bubble that is formed on the suction side.

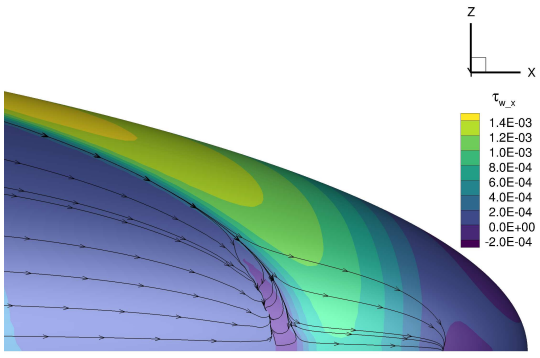

Figure 6.6: Map of the skin-friction in the x direction on the surface of the spheroid using the $k-\omega$ SST model with 0.15 $\%$ of FSTI at the LE of the spheroid. The recirculation of the flow shown by the streamlines highlights a much smaller separation bubble in the suction side than in the RSM.

Figures 6.9 to 6.14 show the C_f distributions obtained with the SSG-LRR-ω for all the converged cases mentioned in table 6.2, as well as for Case1. Figure 6.8 shows the C_f distribution obtained with

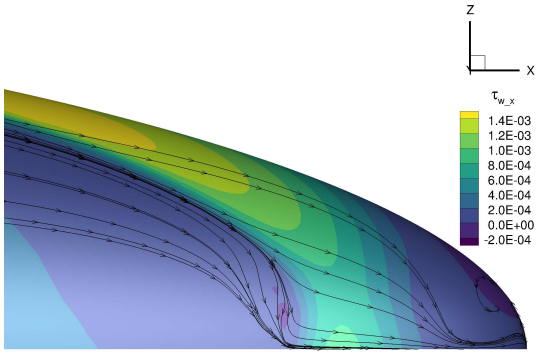

Figure 6.7: Map of the skin-friction in the x direction on the surface of the spheroid using the SSG-LRR-ω with Case4. The streamlines show that there is no recirculation of the flow as in Case1.

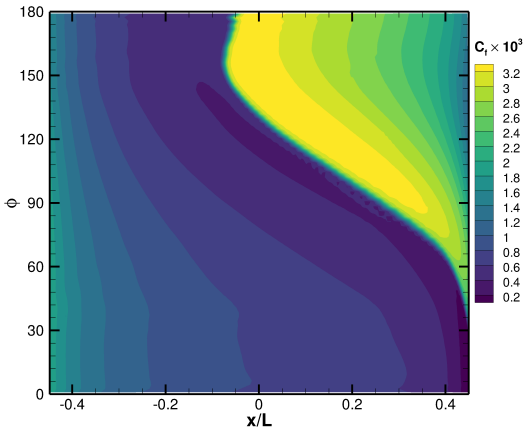

Figure 6.8: C_f distribution on the unrolled surface of the prolate spheroid obtained for Case1 with the $k-\omega$ SST model.

the $k-\omega$ SST model, for Case1. In these figures, the y axis represents the azimuthal angle ϕ of a given point at the surface of the spheroid [72], and the x axis represents the spheroid's non-dimensional length x/L. Except for figure 6.9, whose solution did not converge, the C_f distributions are in line with the expected results:

1. Figure 6.8 displays the results obtained for Case1 with the $k-\omega$ SST model, and show transition occurring fairly downstream of the location predicted by the SSG-LRR-ω for the same case, but with no transition model, patent in figure 6.10;

2. Figure 6.10 presents Case2, with no transition model coupled with the SSG-LRR-ω. The high values of C_f on the left side of the map mean that transition occurs fairly close of the leading edge, considerably upstream of what occurs in all other cases that feature the coupling of the SSG-LRR-ω with the $\gamma - Re_\theta$ model;

3. From Case3 to Case5, in figures 6.11 to 6.13, transition occurs further downstream in each case, due to the successive decrease of the inlet turbulence quantitites. This is understandable, since larger values of inlet FSTI and EVR will prompt transition to occur earlier;

4. Case8, presented in figure 6.14 is comparable to Case5, in figure 6.13, since they both present the same value of 0.26% for the turbulence intensity at the leading edge of the spheroid. However, the higher value of EVR at the spheroid's leading edge in Case8 causes transition to be triggered earlier than in Case5.

Looking at figures 6.9 to 6.14, several conclusions may be withdrawn:

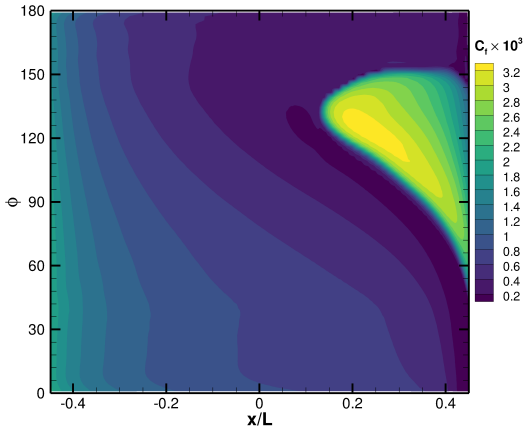

Figure 6.9: C_f distribution on the unrolled surface of the prolate spheroid obtained for Case1, with the SSG-LRR-ω model.

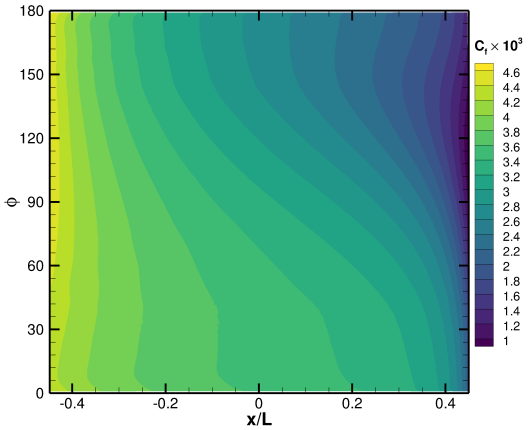

Figure 6.10: C_f distribution on the unrolled surface of the prolate spheroid obtained for Case2, with the SSG-LRR-ω model.

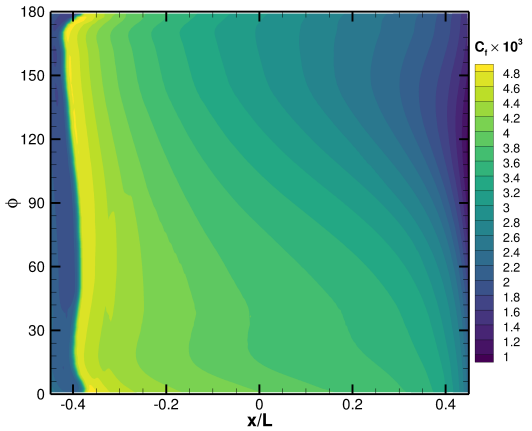

Figure 6.11: C_f distribution on the unrolled surface of the prolate spheroid obtained for Case3, with the SSG-LRR-ω model.

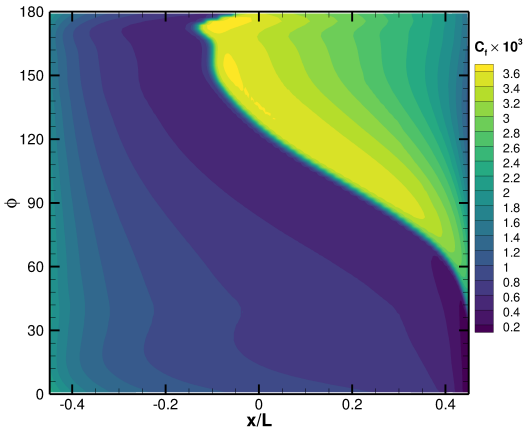

Figure 6.12: C_f distribution on the unrolled surface of the prolate spheroid obtained for Case4, with the SSG-LRR-ω model.

1. The inlet turbulence boundary conditions tuned for being used with the $k-\omega$ SST model are not suitable for being used with the SSG-LRR-ω model with this latter needing a greater turbulence intensity to display the same results of the $k-\omega$ SST model;

2. For identical inlet turbulence boundary conditions, especially for relatively low values, the RSM tends to present larger regions with flow separation, with its inherent recirculation, than the $k-\omega$ SST. This occurs because the RSM delays the occurence of transition and then inherently what happens is laminar separation.

3. The $k-\omega$ SST model can converge to a result in situations where the RSM can present some iterative convergence difficulties, namely in regions of instability, such as the large separation bubble yielded in Case1.

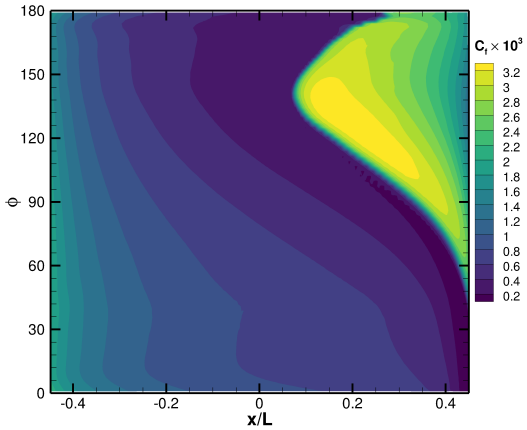

Figure 6.13: C_f distribution on the unrolled surface of the prolate spheroid obtained for Case5, with the SSG-LRR-ω model.

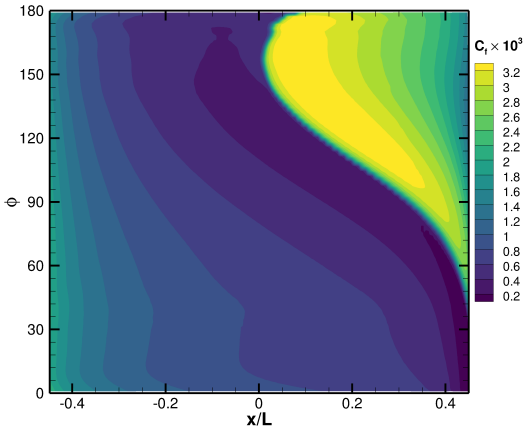

Figure 6.14: C_f distribution on the unrolled surface of the prolate spheroid obtained for Case8, with the SSG-LRR-ω model.

Chapter 7

Conclusions

This chapter intends to summarize the achievements and conclusions obtained in the different test-cases, whilst providing some ideas for future work developed in this area.

7.1 Achievements

7.1.1 Validation with results from other codes and experimental data

The coupling of the SSG-LRR-ω + $\gamma - Re_\theta$ implemented in ReFRESCO demonstrated equivalent results to the ones obtained with the same coupling implemented in other CFD codes. When comparing with experimental data, the results were in accordance with what was expected i.e. the RSM predicted transition slightly downstream of what was verified in the real flow.

7.1.2 Numerical Robustness of the SSG-LRR-ω + $\gamma - Re_\theta$ coupling

Along almost all the simulations performed in this thesis, the SSG-LRR-ω model demonstrated to have a satisfactory iterative convergence, with no major problems in reducing the residuals to negligible levels. However, in general, it proved to have more difficulties in converging to a solution than the $k-\omega$ SST model, i.e., it took a larger number of iterations. Additionaly, in some situations of large regions of instability, such as separation bubbles, the RSM could not converge to a solution, whilst the $k-\omega$ SST model could. The RSM presented a greater grid dependence, and needed a finer grid than the $k-\omega$ SST model to present similar results. The uncertainty of the calculation of transition position when increasing the grid refinement is larger in the RSM than in the $k-\omega$ SST.

7.1.3 Transition Prediction

In this thesis was concluded that the SSG-LRR-ω tends to present transition downstream of the location predicted by the $k-\omega$ SST model. In some specific cases, when the values of the inlet turbulence boundary conditions are lower, the RSM may not be able to match the experimental data and the values

predicted by the $k-\omega$ SST: these latter two exhibit transition whilst the RSM predicts a full laminar solution.

7.1.4 Influence of the decay of the turbulence inlet conditions

The decay of the FSTI is more accentuated than the one of the EVR, meaning that variations of the inlet value of the EVR will have a greater impact on the simulation results than variations of the inlet FSTI - greater decay of the FSTI will imply that a variation on the inlet is not translated into a variation near a test-body located far downstream from the inlet.

The higher the value of the inlet turbulence boundary conditions, the greater the sensitivity of the models studied to changes in these conditions. From all the models studied, the SSG-LRR-ω appeared to be the most sensitive.

It was also found out that the inlet turbulence boundary conditions tuned to be used with the $k-\omega$ SST are not the most suitable to be used with the SSG-LRR-ω.

7.2 Future Work

With the conclusions withdrawn from the work developed, it is possible to define some future work to be carried out regarding this topic.

It would be interesting to study a method to obtain the appropriate inlet turbulence boundary conditions to be used in a study with the SSG-LRR-ω, taking the conditions tuned for the $k-\omega$ SST as a starting point, since this latter is a more commonly used model, and therefore there is plenty of accessible data for it. The experimental data available could also be used to tune these conditions for the RSM.

Another suggestion would be to include the crossflow prediction method in this coupling, and assess if the differences observed in the spheroid test-case between the $k-\omega$ SST and the SSG-LRR-ω would persist. The crossflow prediction would also be useful to better compare the results obtained in this test-case with the experimental ones.

Stability studies could be carried out, in order to perceive if would be worth to develop additional tools to ensure the iterative convergence of the SSG-LRR-ω in a broad set of conditions, i.e, when there are large instability regions, or if the test-body presents a complex geometry.

Finally, it would be fruitful to compare the performance of the SSG-LRR-ω with other turbulence models in environments that theoretically suit this model the most [4]. To seize all the advantages coming from the ability to deal with the turbulence anisotropy, some test-cases could be studied, such as delta wings, oblate spheroids, or even moving cylinders.

Bibliography

[1] T. Sayadi, C. Hamman, and P. Moin. Direct numerical simulation of complete h-type and k-type transitions with implications for the dynamics of turbulent boundary layers. *Journal of Fluid Mechanics*, 724:480, 2013.

[2] S. Nie. *Extension of transition modeling by a transport equation approach*. PhD thesis, DLR, 2017.

[3] T. Sayadi and P. Moin. Large eddy simulation of controlled transition to turbulence. *Physics of Fluids*, 24(11):114103, 2012.

[4] Y. Hassan. An overview of computational fluid dynamics and nuclear applications. *Thermal-Hydraulics of Water Cooled Nuclear Reactors*, pages 729–829, 2017.

[5] F. Menter. Improved two-equation k-omega turbulence models for aerodynamic flows. *Nasa Sti/recon Technical Report N*, 93:22809, 1992.

[6] R. Cécora, R. Radespiel, B. Eisfeld, and A. Probst. Differential reynolds-stress modeling for aeronautics. *AIAA Journal*, 53(3):739–755, 2015.

[7] R. Langtry and F. Menter. Correlation-based transition modeling for unstructured parallelized computational fluid dynamics codes. *AIAA Journal*, 47(12):2894–2906, 2009.

[8] Refresco software features. `https://www.marin.nl/facilities-and-tools/software/refresco`. Accessed: 2021-02-15.

[9] W. Saric, H. Reed, and E. Kerschen. Boundary-layer receptivity to freestream disturbances. *Annual review of fluid mechanics*, 34(1):291–319, 2002.

[10] V. Brederode. Fundamentos de aerodinâmica incompressível. *Author's Edition*, 1997.

[11] M. Morkovin. Transition in open flow systems-a reassessment. *Bull. Am. Phys. Soc.*, 39:1882, 1994.

[12] S. Orszag. Accurate solution of the orr–sommerfeld stability equation. *Journal of Fluid Mechanics*, 50(4):689–703, 1971.

[13] E. Mayda. *Boundary-layer transition prediction for Reynolds-averaged Navier-Stokes methods*. ProQuest Dissertations Publishing, 2007, 2007.

[14] M. Malik, F. Li, M. Choudhari, and C. Chang. Secondary instability of crossflow vortices and swept-wing boundary-layer transition. *Journal of Fluid Mechanics*, 399:85–115, 1999.

[15] P. Rizzo, J. Serpieri, and M. Kotsonis. Crossflow transition of a swept-wing boundary layer and its sensitivity to free-stream conditions and surface roughness. In *AIAA Scitech 2019 Forum*, page 1133, 2019.

[16] L. Zhou, R. Li, Z. Hao, D. Zaripov, and C. Yan. Improved k-omega gamma model for crossflow-induced transition prediction in hypersonic flow. *International Journal of Heat and Mass Transfer*, 115:115–130, 2017.

[17] G. Schubauer and H. Skramstad. Laminar boundary-layer oscillations and stability of laminar flow. *Journal of the Aeronautical Sciences*, 14(2):69–78, 1947.

[18] B. Simon. *Active cancellation of Tollmien-Schlichting waves under varying inflow conditions for in-flight application*. PhD thesis, Technische Universitat Darmstadt, 2017.

[19] R. Langtry. A correlation-based transition model using local variables for unstructured parallelized cfd codes. *ASME Journal of Turbomachinery*, 128(3):413–422, 2006.

[20] B. McAuliffe and M. Yaras. Transition mechanisms in separation bubbles under low-and elevated-freestream turbulence. *Journal of Turbomachinery*, 132(1), 2010.

[21] A. Choudhry, M. Arjomandi, and R. Kelso. A study of long separation bubble on thick airfoils and its consequent effects. *International Journal of Heat and Fluid Flow*, 52:84–96, 2015.

[22] U. Rist and H Fasel. Direct numerical simulation of controlled transition in a flat-plate boundary layer. *Journal of Fluid Mechanics*, 298:211–248, 1995.

[23] Dns. `https://www.cfd-online.com/Wiki/Direct_numerical_simulation_(DNS)o`. Accessed: 2021-04-23.

[24] X. Wu and P. Moin. Direct numerical simulation of turbulence in a nominally zero-pressure-gradient flat-plate boundary layer. *Journal of Fluid Mechanics*, 630:5, 2009.

[25] V. Ovchinnikov, U. Piomelli, and M. Choudhari. Numerical simulations of boundary-layer transition induced by a cylinder wake. *Journal of Fluid Mechanics*, 547:413, 2006.

[26] L. Jiang, M. Choudhari, C. Chang, and C. Liu. Numerical simulations of laminar-turbulent transition in supersonic boundary layer. In *36th AIAA Fluid Dynamics Conference and Exhibit*, page 3224, 2006.

[27] C. Mayer, D. Von Terzi, and H. Fasel. Direct numerical simulation of complete transition to turbulence via oblique breakdown at mach 3. *Journal of Fluid Mechanics*, 674:5, 2011.

[28] J. Smargorinsky. General circulation experiment with the primitive equations. *Monthly Weather Review*, 91(3):99–164, 1963.

[29] U. Balaras and U. Piomelli. Wall-layer models for large-eddy simulations. *Annu. Rev. Fluid Mech*, 34:349, 2002.

[30] K. Squires. Detached-eddy simulation: current status and perspectives. In *Direct and large-eddy simulation V*, pages 465–480. Springer, 2004.

[31] F. Ducros, P. Comte, and M. Lesieur. Large-eddy simulation of transition to turbulence in a boundary layer developing spatially over a flat plate. *Journal of Fluid Mechanics*, 326:1–36, 1996.

[32] H. Belkhou, S. Russeil, T. Dbouk, M. Mobtil, D. Bougeard, and N. Francois. Large eddy simulation of boundary layer transition over an isolated ramp-type micro roughness element. *International Journal of Heat and Fluid Flow*, 80:108492, 2019.

[33] P. Durbin. Turbulence closure models for computational fluid dynamics. *Encyclopedia of Computational Mechanics*, 3, 2004.

[34] J. Boussinesq. *Théorie analytique de la chaleur mise en harmonic avec la thermodynamique et avec la théorie mécanique de la lumière: Tome I-II*, volume 2. Gauthier-Villars, 1903.

[35] L. Davidson. *An introduction to turbulence models*. PhD thesis, Chalmers University of Technology, 2015.

[36] G. Gerolymos and I. Vallet. Computation of 3-d aerospace configurations using a wall-normal-free reynolds-stress model. In *Engineering Turbulence Modelling and Experiments 5*, pages 371–382. Elsevier, 2002.

[37] S. Keye and O. Brodersen. Investigations of fluid-structure coupling and turbulence model effects on the dlr results of the fifth aiaa cfd drag prediction workshop. In *31st AIAA Applied Aerodynamics Conference*, page 2509, 2013.

[38] C. Cambon, L. Jacquin, and J. Lubrano. Toward a new reynolds stress model for rotating turbulent flows. *Physics of Fluids A: Fluid Dynamics*, 4(4):812–824, 1992.

[39] B. Eisfeld and O. Brodersen. Advanced turbulence modelling and stress analysis for the dlr-f6 configuration. In *23rd AIAA Applied Aerodynamics Conference*, page 4727, 2005.

[40] R. Maduta. *An eddy-resolving Reynolds stress model for unsteady flow computations: development and application*. PhD thesis, Technische Universitat Darmstadt, 2013.

[41] K. Bhaganagar, D. Rempfer, and J. Lumley. Direct numerical simulation of spatial transition to turbulence using fourth-order vertical velocity second-order vertical vorticity formulation. *Journal of Computational Physics*, 180(1):200–228, 2002.

[42] D. Di Pasquale, A. Rona, and S Garrett. A selective review of transition modelling for cfd. In *39th AIAA fluid dynamics conference*, page 3812, 2009.

[43] J Van Ingen. The en method for transition prediction. historical review of work at tu delft. In *38th Fluid Dynamics Conference and Exhibit*, page 3830, 2008.

[44] F. Menter, R. Langtry, S. Likki, Y.B. Suzen, P.G. Huang, and S. Völker. A correlation-based transition model using local variables—part i: model formulation. 2006.

[45] Florian R Menter, Pavel E Smirnov, Tao Liu, and Ravikanth Avancha. A one-equation local correlation-based transition model. *Flow, Turbulence and Combustion*, 95(4):583–619, 2015.

[46] R. Lopes. *Simulation of Transition from Laminar to Turbulent Regime in Practical Applications of Incompressible Flow*. PhD thesis, IST, 2021.

[47] F. Menter, Y. Egorov, and D. Rusch. Steady and unsteady flow modelling using the kskl model. In *Turbulence Heat and Mass Transfer 5. Proceedings of the International Symposium on Turbulence Heat and Mass Transfer*. Begel House Inc., 2006.

[48] A. Dewan. Reynolds-averaged governing equations and closure problem. In *Tackling Turbulent Flows in Engineering*, pages 43–48. Springer, 2011.

[49] Menter shear stress transport turbulence model. `https://turbmodels.larc.nasa.gov/sst.html`, . Accessed: 2020-09-30.

[50] Turbulence kinetic energy. `https://https://www.cfd-online.com/Wiki/Turbulence_kinetic_energy`. Accessed: 2021-04-13.

[51] Turbulence dissipation rate. `https://www.cfd-online.com/Wiki/Turbulence_dissipation_rate`. Accessed: 2021-04-13.

[52] C. Speziale, S. Sarkar, and T. Gatski. Modelling the pressure–strain correlation of turbulence: an invariant dynamical systems approach. *Journal of fluid mechanics*, 227:245–272, 1991.

[53] B. Launder, G. Jr. Reece, and W. Rodi. Progress in the development of a reynolds-stress turbulence closure. *Journal of fluid mechanics*, 68(3):537–566, 1975.

[54] Ssg/lrr full reynolds stress model. `https://turbmodels.larc.nasa.gov/rsm-ssglrr.html`, . Accessed: 2020-09-30.

[55] R. Cécora, R. Radespiel, B. Eisfeld, A. Probst, S. Crippa, and R. Radespiel. Differential reynolds stress modeling for aeronautics. In *50th AIAA Aerospace Sciences Meeting including the New Horizons forum and aerospace exposition*, page 465, 2012.

[56] B. Eisfeld, C. Rumsey, and V. Togiti. Verification and validation of a second-moment-closure model. *AIAA Journal*, 54(5):1524–1541, 2016.

[57] B. Eisfeld. Implementation of reynolds stress models into the dlr-flower code. 2004.

[58] Langtry-menter 4-equation transitional sst model. `https://turbmodels.larc.nasa.gov/langtrymenter_4eqn.html`, . Accessed: 2020-09-30.

[59] R. Lopes, E. Fernandes, L. Eça, G. Vaz, and M. Kerkvliet. Coupling two correlation-based transition models to the k- k l eddy viscosity turbulence model. *AIAA Journal*, 59(5):1735–1748, 2021.

[60] R. Lopes, L. Eça, and G. Vaz. On the decay of free-stream turbulence predicted by two-equation eddy-viscosity models. In *20th Numerical Towing Tank Symposium*, pages 133–138, 2017.

[61] P. Spalart and C. Rumsey. Effective inflow conditions for turbulence models in aerodynamic calculations. *AIAA Journal*, 45(10):2544–2553, 2007.

[62] Petsc. `https://www.mcs.anl.gov/petsc/index.html`. Accessed: 2021-03-12.

[63] B. Leonard. A stable and accurate convective modelling procedure based on quadratic upstream interpolation. *Computer methods in applied mechanics and engineering*, 19(1):59–98, 1979.

[64] J. Ferziger, M. Perić, and R. Street. *Computational methods for fluid dynamics*, volume 3. Springer, 2002.

[65] David C Wilcox et al. *Turbulence modeling for CFD*, volume 2. DCW industries La Canada, CA, 1998.

[66] Avt 313 workshop. `http://web.tecnico.ulisboa.pt/ist12278/Workshop_AVT_313_2D_cases/Workshop_AVT_313_2D_cases.htm`. Accessed: 2020-10-30.

[67] AM Savill. Evaluating turbulence model predictions of transition. In *Advances in Turbulence IV*, pages 555–562. Springer, 1993.

[68] R. Lopes, L. Eça, and G. Vaz. On the numerical behavior of rans-based transition models. *Journal of Fluids Engineering*, 142(5), 2020.

[69] L. Eça and M. Hoekstra. A procedure for the estimation of the numerical uncertainty of cfd calculations based on grid refinement studies. *Journal of computational physics*, 262:104–130, 2014.

[70] L. Eça, R. Lopes, F. Pereira, and G. Vaz. Numerical and parameter uncertainties: Are they independent? In *ASME 2019 Verification and Validation Symposium*. American Society of Mechanical Engineers Digital Collection, 2019.

[71] J.G. Coder. Standard test cases for transition model verification and validation in computational fluid dynamics. In *2018 AIAA Aerospace Sciences Meeting*, pages 2018–0029, 2018.

[72] G. Korn and T. Korn. Mathematical handbook for scientists and engineers. *New York*, 1968.